AN ABSTRACT OF THE THESIS OF

Clayton Lamar Hires for the degree of Master of Science in Industrial Engineering presented on December 2, 2010.
Title: Uniform Residence Time in Microreactor-Assisted Solution Deposition of CdS Thin-Films for CIGS Photovoltaic Cells

Abstract approved:

Brian K. Paul

Photovoltaic (PV) cells have long been an attractive alternative for the consumption of fossil fuels but current manufacturing practices suffer from poor energy efficiency, large carbon footprints, low material utilization, high processing temperatures and high solvent usage. A critical step in PV production is the deposition of CdS as a thin film to serve as a "buffer layer" between the optically absorbent layer and the transparent conducting oxide (TCO) layer to complete an effective p-n junction. The development of an inexpensive, low temperature, constant flow deposition process for producing CdS films is investigated. Micro-assisted solution concepts are implemented to promote the selectivity of heterogeneous surface reactions over homogeneous bulk precipitation. Analytical models based off Hagen-Poiseuille equation for fluid flow are coupled with computational fluid dynamic simulations to produce uniform flow fields within the deposition step permitting uniform film coverage on large substrates.

Uniform Residence Time in Microreactor-assisted Solution Deposition of CdS Thin-films for CIGS Photovoltaic Cells

by
Clayton Lamar Hires

A THESIS

submitted to

Oregon State University

in partial fulfillment of
the requirements for the
degree of

Master of Science

Presented December 2, 2010
Commencement June 2011

Master of Science thesis of Clayton Lamar Hires presented on December 2, 2010.

APPROVED:

Major Professor, representing Industrial Engineering

Head of the School of Mechanical, Industrial, and Manufacturing Engineering

Dean of the Graduate School

I understand that my thesis will become part of the permanent collection of Oregon State University libraries. My signature below authorizes release of my thesis to any reader upon request.

Clayton Lamar Hires, Author

ACKNOWLEDGEMENTS

First of all, I would like to express my sincere gratitude to my major professor Dr. Brian K. Paul, first for inspiring my interest in micro/nano fabrication field and secondly for his valuable guidance in every aspect during my graduate studies at Oregon State University. My appreciation is extended to my graduate committee members Dr. William Warnes, Dr. Karl Haapala, and Dr. John Parmigiani for their recommendations, advice and support throughout my thesis project.

I would also like to thank my immediate laboratory partners Sudhir Ramprasad, Yu Wei Su (Wayne) for their persistent work, long hours, and support throughout the years. A special thanks also goes to Don Higgins for his insight and knowledge in fabrication support, Dan Palo for his excellence in team leadership and project management and Chih-Hung Chang for his contributions guiding countless technical aspects of this project. I am very grateful for the time and effort of Anna Garrison for her contributions to defining fluid dynamic concepts and methods and support with simulation model. I am especially thankful for Brenda Langely, Joey Wilcox, Mark Smith, and Jay Mosher for critical mental and moral support over this endeavor.

Finally, I am truly and endlessly grateful for my parents to whom I owe all my accomplishments Nadine A. Hires and Clayton Hires Sr. for believing in me, nurturing, and supporting my goals since youth.

TABLE OF CONTENTS

Page

TABLE OF CONTENTS (Continued)

Page

LIST OF APPENDICES

Appendix Page

LIST OF FIGURES

LIST OF FIGURES (Continued)

LIST OF FIGURES (Continued)

LIST OF FIGURES (Continued)

LIST OF FIGURES (Continued)

Figure Page

LIST OF TABLES

Table Page

1. INTRODUCTION

1.1. Photovoltaic Industry

Concern for the energy crisis involving fossil fuel consumption is intensifying. The limited availability of resources, growing energy demand, and adverse effects of CO_2 emissions continue to add to this concern. As an alternative energy solution, solar power has long since been recognized for having the potential to curtail many of these problems. In fact, it is estimated that enough solar radiation reaches the earth's surface in one hour to replace all the electricity, coal, gas, and fire that all humans consume in an entire year. (Engelbrecht 2006). In addition each solar cell creates no emissions, noise, or has any moving parts. The development of an inexpensive, efficient solar device would not only address the destructive environmental impacts and energy demands of developed countries but also provide many opportunities for developing nations. Currently there are about 2-3 billion people worldwide that do not have electricity and other basic amenities requiring dependable power sources.

The photovoltaic (PV) market has grown approximately 33% per year since 1997 with the aid of market support programs (Hoffmann, 2006) and is characterized by its impact in four major segments shown in Figure 1-1: *Consumer application* – such as calculators, watches, battery chargers, *Remote industrial electrification* - off grid power generators, traffic signals, GPS systems, *Developing countries* – water pumping systems,

solar home systems, small village grids, *Grid-connected systems* – integrated rooftop systems, window shading, sound barriers wall along highways.

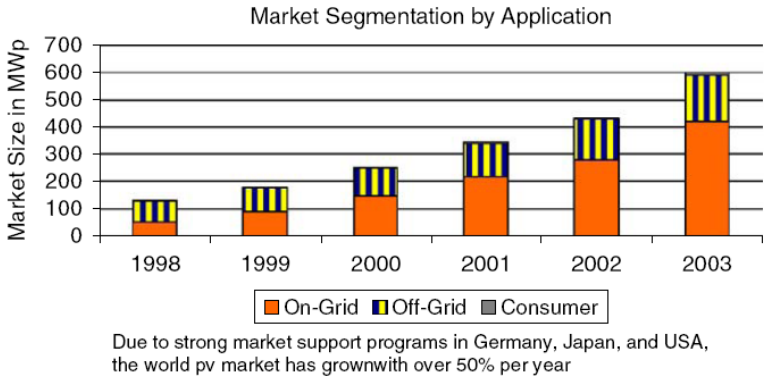

Figure 1-1: Market growth of solar electricity industry. [Hoffman 2006]

Despite the rapid growth of PV industry, the bulk of applied PV applications exist primarily due to market support aid programs. Figure 1-2 shows the largest solar energy consumption is found in the on-grid sector of the four sectors mentioned. Due to the fossil fuel based infrastructure within on-grid regions current PV integration is not yet considered economically feasible.

Figure 1-2: Solar electricity market segments.

1.2. PV industry barriers

The most prominent reason solar technology has not become the dominating mainstream energy source is due to its production cost. Over the last few decades there has been a dramatic decline in the production cost of Si-based solar cells ≈$4.2/Watt in 1992 to $1.7/Watt in 2002, but large scale commercial viability has not been achieved (Chopra et al., 2004). The expense for most solar panels is mainly due to complexity involved in producing high purity silicon substrates and depositing thin films with the uniformity, precision, and high tolerances needed for effective functionality. In addition, small deviations in crystal orientation, morphology, and film thickness have drastic effects on the efficiency of the solar cells function.

1.3. Value of non-silicon substrates

Recent advances in solar technology have given rise to several thin film manufacturing approaches to solar cell development. These approaches are considerably more cost effective, albeit less efficient, at solar conversion. In particular, CIGS (copper-indium-gallium-diselenide) alloys are showing promise in the emerging thin film PV industry (Engelbrecht 2006). A film less than 1μm thick of CIGS is able to absorb the same amount of incident sunlight as 350 μm of silicon. In addition to being more cost effective than silicon, CIGS solar cells can be applied to flexible surfaces of various sizes and shapes for increasing the portable application of this technology.

1.4. Process of developing CIGS cells

The development of successful CIGS films is very complex. Initially, the three metals: copper (Cu), indium (In), and gallium (Ga) are combined into a high quality alloy of uniform crystal structure. Figure 1-3 shows the surface of this alloy is then carefully doped with selenium to create a thin layer of CIGS film. Typically, a buffer layer is deposited on top of the CIGS film followed by a transparent conducting oxide (TCO) layer, such as intrinsic zinc oxide and/or a doped zinc oxide. The substrate of the cell is usually separated from the CIGS layer by a positive metallic contact (Mo in Figure 1-3 below) along with a negative metallic contact on top of the doped zinc oxide (not shown) to provide a pathway for generated electricity to leave the cell and do work.

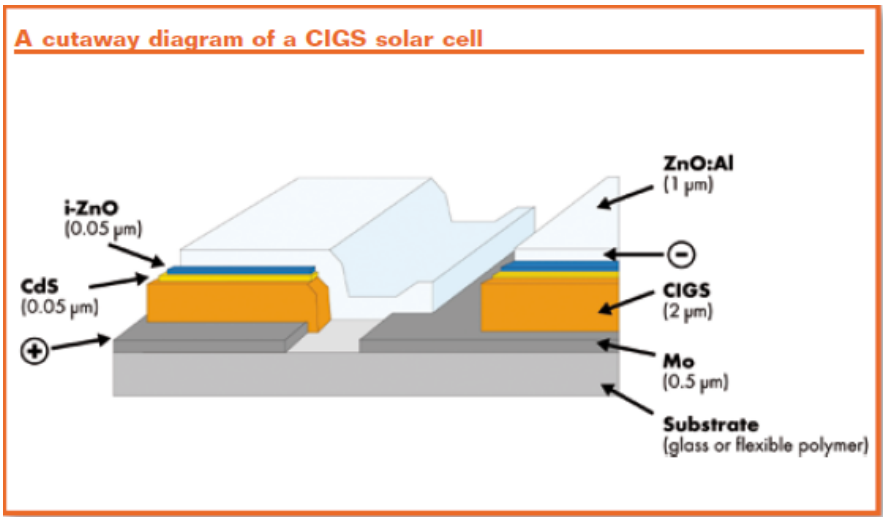

Figure 1-3: Diagram of films deposited for a typical CIGS solar cell. [Engelbrecht et al, 2006]

1.5. Role of CdS in PV cells

When incident light reaches the CIGS absorber layer, the energy is absorbed by electrons, exciting them to a state that effectively allows them to leave their orbital shells. This creates electron-hole pairs that are capable of traveling short distances (about 10-20nm) by diffusion before they fall back into an orbital energy shell (recombination). Direct contact between the CIGS layer and the transparent conducting oxide layer (TCO) will complete an effective p-n junction, but is considered fundamentally inferior without the presence of a buffer layer due to unacceptably high recombination effects.

Typically, cadmium sulfide (CdS) is used to form this core “buffer” or “window” layer component of heterojunction photovoltaic (PV) cells. CdS is a direct band gap

semiconductor with a band gap energy of 2.42 eV and has the property of becoming more conductive when exposed to light. As a buffer layer it serves to extend the distance electrons can travel before recombining and reduces reflection in the absorption layer. The CdS buffer layer should be conductive (electron density, $\eta \approx 10^{16}$ cm^{-3}), thin enough for high transmission (50-100 nm), and uniform to avoid short circuit areas. As a drawback, CdS tends to absorb radiation in the blue light spectrum meaning energy in this range is not allowed to reach the absorption layer for photogeneration. While photogeneration does occur in the CdS buffer layer, the charge generated is only partially collected, thus reducing the overall cell performance in this range.

1.6. CdS deposition by Chemical Bath Deposition

CdS films are deposited using a variety of techniques that can be classified into two categories: vapor phase and liquid phase deposition. Vapor phase techniques consist of methods such as PVD, CVD, and plasma-based deposition procedures. Liquid phase methods are divided into chemical bath deposition (CBD), electrochemical deposition, electrodeposition from fused salts, and deposition through successive ionic layer adsorption and reaction. Of these methods CBD is typically valued as an industry standard due to its relative ease to implement and low expense for covering large surface area devices. The CBD process involves large volumes of the reacting fluid that are not in intimate contact with a substrate surface, leading to an extremely high volume to surface area ratio. This results in low yields for cadmium conversion into the

final film and requires a large concentration of ammonia which can be a barrier for large industrial scale facilities. Poor material utilization, high solvent usage, low energy efficiency, and environmental discharges ultimately restrict the potential of the final cell from becoming a competitive energy alternative. These restrictions are of great concern, since the overall success of PV technology as a reasonable energy alternative depends on the simplicity of manufacturability and final cost per reliable watt.

CdS chemistry: The typical method for creating CdS films using CBD, is through the hydrolysis of thiourea in the presence of a cadmium salt and a chelating agent. The chelating agent, normally NH_3, is mainly used to limit the hydrolysis of the metal ion which slowly releases sulfide ions into solution. This results in the precipitation of CdS onto a substrate surface according to the following reaction:

Global Reaction

$$Cd(NH_3)_4^{+2} + SC(NH_2)_2 + 2OH^- \rightarrow CdS + CH_2N_2 + 4NH_3 + H_2O \quad (1)$$

Intermediate Step

$$SC(NH_2)_2 + 2OH^- \rightarrow S^{2-} + CH_2N_2 + 2H_2O \quad (2)$$

$$Cd(L)_n^{2+} \rightarrow Cd^{2+} + nL \quad (3)$$

$$Cd^{2+} + S^{2-} \rightarrow CdS_{(solid)} \quad (4)$$

CBD reaction: In a typical experimental setup, a target substrate is submersed in a large bath with the starting chemicals of cadmium chloride ($CdCl_2$), ammonium chloride (NH_4Cl), and thiourea ($SC(NH_2)_2$). The bath is slowly agitated and heated to 80 °C. The addition of NH_4OH raises the pH of the solution to approximately 11 which initiates the hydrolysis of thiourea in the bulk solution (intermediate step above). Once initiated, competing reactions occur for the available Cd^{2+} ions: the heterogeneous growth of the CdS film on the substrate and homogeneous formation of CdS in the bulk fluid. Precipitation of CdS occurs once its solubility reaches its threshold concentration in the bulk fluid, which begins to further impede the heterogeneous reaction. A linear growth rate is reported preceded by an initial induction period time lag as shown in Figure 1-4.

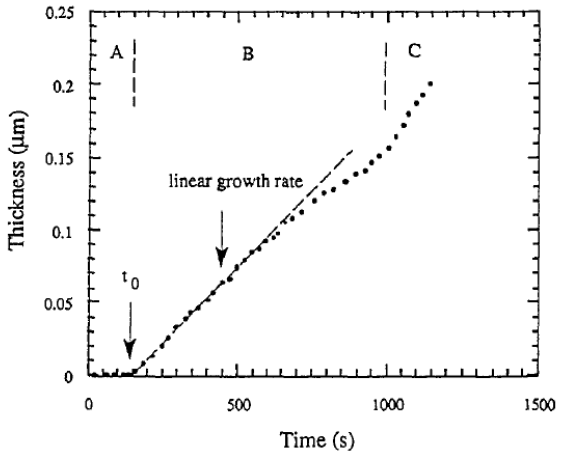

Figure 1-4: Typical growth curve of CdS using CBD processing (A) Induction region (B) linear growth of compact layer (C) growth by precipitated particles [Ortega-Borges, et al 1993]

The initial induction period is observed to be a function of the CdS saturation level in the bulk fluid. It is proposed that at low saturation, spontaneous nucleation of sites is low as is their available surface area. Once an adequate number of sites have formed and surface area has been achieved the growth proceeds into a linear region. (Kostoglou et al., 2000) Eventually, a third region is reached where film growth exponentially decreases as Cd^{2+} concentration is depleted and growth of a porous over-layer of coagulated particles dominates.

Film nucleation: The desired heterogeneous layer is firmly adhered to the substrate by "ion-by-ion" deposition of Cd^{2+} and S^{2-} in both CBD and continuous flow conditions. Early stage TEM images from Froment et al. (1995) show that several perfectly monocrystalline nuclei appear on the substrate surface, which grow until they coalesce into the final film. Ultrasonication and choice of substrate also have noticeable influence on this initial nucleation. Studies by Oliva et al. (2003) show that by using ultrasonication nucleation density increased and heterogeneous growth was promoted over sub-product reactions. Oliva et al. (1999) witnessed low nucleation and poor crystallinity on silicon in comparison to indium-tin-oxide (ITO) and glass substrates. It was found that structural changes occur in silicon substrates due to its preferable adsorption of cadmium hydroxide, suggesting that silicon is inappropriate as a substrate for CdS deposition. Under certain conditions, the presence of a non-adherent layer has also been observed which is attributed to the adsorption of aggregated precipitation particles that form in the bulk solution.

Several factors such as temperature, pH and choice of substrate affect the type of film which occurs, but the final film quality and adherence is strongly affected by CdS saturation conditions. Kostoglou (2003) define the supersaturation ratio:

$$S = \frac{[(Cd^{2+})(S^{2-})]^{1/2}}{K_{sp}} \quad (5)$$

which is a critical driving force for solid phase precipitation in the bulk fluid where the activities of the respective ions are related to K_{sp}, which denotes the thermodynamic solubility of CdS. At low saturation (less than 5), large nuclei were found to form and gradually increased in size over time. The overall surface coverage was found to be poor, even with long deposition times. Film adherence was good. At high saturation (greater than 8), the grain size was relatively small but thinner films were possible with better surface coverage. The adherence of this final film was poor as it contained many loose particles. In addition, the turbidity of liquid samples was high indicating bulk precipitation of CdS. As a result, an initial saturation range of 5 to 8 was considered optimal. In contrast, Kostoglou (2003) was able to first introduce substrates to highly saturated solutions to initiate a large number of nuclei sites for coverage and switch to a lower saturated solution for increased film growth, grain size, and coherence. These results have implications for microreactor-assisted deposition of CdS where temporal control of reactant concentration is possible.

Final film characterization: Final film characterization is usually performed using physical morphology, crystallinity, optical transmission, and band gap energy properties.

Final film roughness has been shown to be smaller than the initial roughness of many substrates. Roughness was compared on three different substrates: uncoated glass, silicon, and indium-tin-oxide-coated (ITO) with arithmetic average roughness, R_a, of 0.6 nm, 1.1 nm, and 6.7 nm respectively. After a 10 min deposition time, ITO showed no significant change in roughness. Figure 1-5 shows that the relatively smooth glass and silicon showed little change until CdS saturation was reached and bulk precipitates began to deposit on the surface (Oliva et al., 1999).

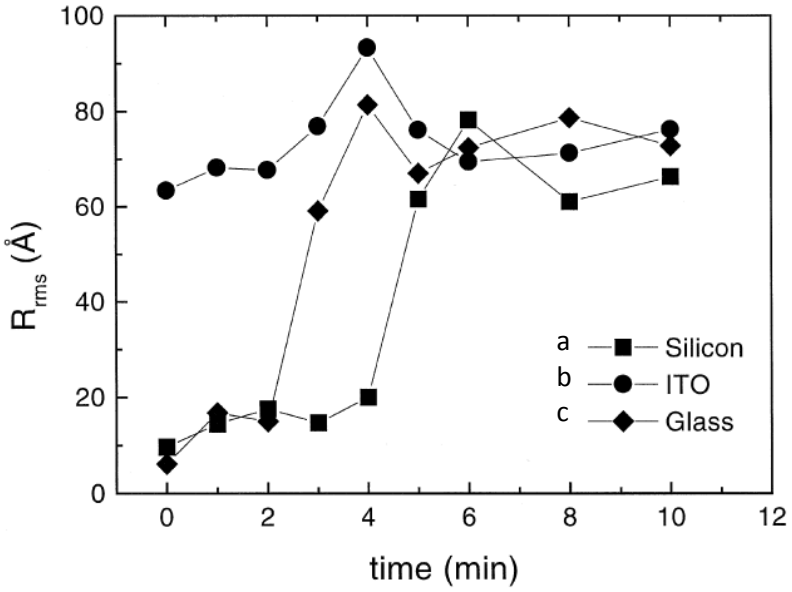

Figure 1-5: AFM images of surface roughness before and after a 3 min CBD deposition. a) Silicon b) ITO coated glass c) Corning glass. [Oliva, et al., 1999]

Crystallinity of the final films is measured through X-ray diffractograms (XRD) and typically show the presence of both the (002) hexagonal and (111) cubic phases of CdS. The desired crystallinity for CdS PV films is the stable hexagonal structure which is normally seen at higher temperature reaction conditions. The intensive peak of the 002 plane is masked by the 100 peak of SnO_2 at ~27° which require identification of hexagonal CdS with the less intensive peaks of 100 and 101 on the shoulders of the main peak at ~27° as seen in Figure 1-6.

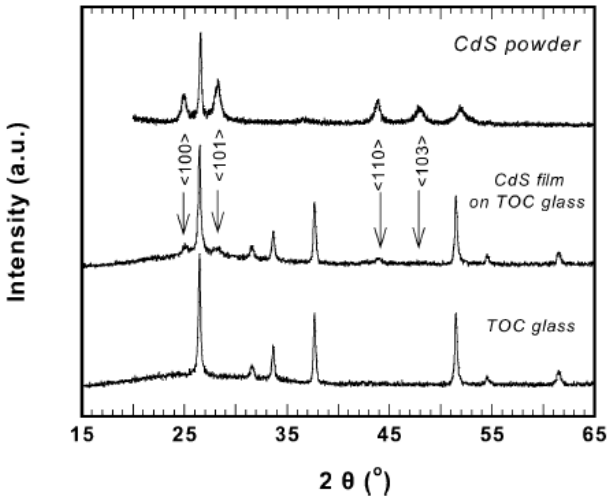

Figure 1-6: X-ray diffractograms of TOC glass, CdS on TOC glass, and precipitate CdS powder. [Kostoglou et al., 2000]

The presence of non-adherent CdS powder can be distinguished by the additional peaks for 110 and 103 planes at ~44° and ~48° associated with the CdS cubic structure. Oliva et al. (2003) reported a CBD procedure to deposit a metastable CdS cubic structure that transitions to a stable hexagonal structure following a 300 °C annealing step.

The band gap energy of a film is determined by optical adsorption of UV light in the range of 300 to 800 nm using the equation:

$$\propto^2 \frac{1}{d^2} ln^2 \left[\frac{I_0}{I}\right] = A\left(E - E_g\right) \quad (6)$$

where α is adsorption coefficient, *d* the film thickness, I and I_0 the transmitted and emitted light intensities, A is a constant, and E the light energy.

1.7. Value of MASD to PV manufacturing

Microreactor-assisted-solution-deposition (MASD) is the coupling of microreactor technology with continuous flow deposition to resolve the temporal evolution of reaction chemistry. MASD techniques are capable of providing higher reaction selectivities which enable unique chemistries that are not accessible through CBD. Higher selectivity can lead to higher material utilization, less waste, and lower cost. Other benefits include reducing energy requirements, reducing time and number of steps for long synthesis reactions, provide access to short life intermediates, and increasing reaction selectivity (Lowe et al, 1998). Other potential benefits of MASD include characteristically small reaction volumes which reduces the exposure to hazardous materials.

The benefits of using microreactor devices are primarily realized in diffusion-limited processes. In the case of a fluid containing molecules that diffuse to the edge of a circular tube to react or transfer heat, the molecules in the center of the tube have a shorter distance to diffuse in a microchannel as shown in Figure 1-7. The speed at which molecules diffuse from the center of the tube to the wall is according to its diffusivity (m^2/s) in the solvent. The necessary molecular residence time is proportional to the square of tube radius over the diffusivity. Therefore, a 10x reduction in tube diameter results in a 100x reduction in the residence time and the consequent axial length of the reactor.

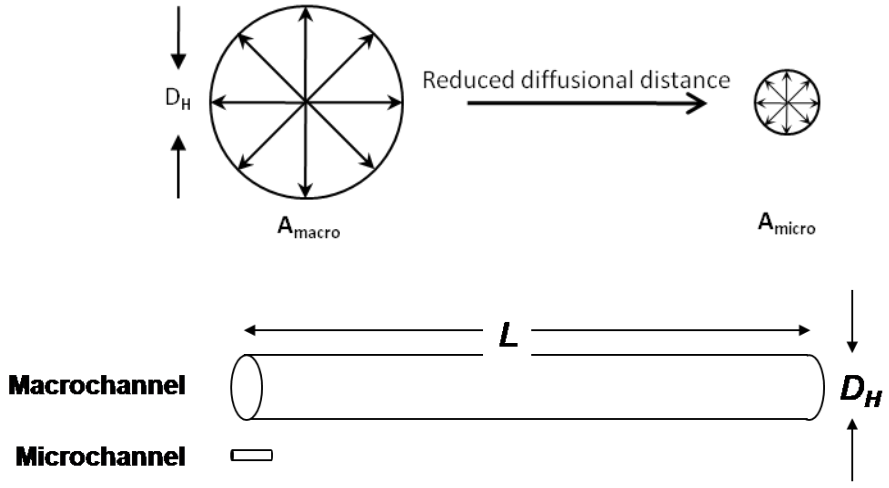

Figure 1-7: Microchannel pipe lengths needed based on mass transport times of molecular species as a function of hydraulic diameter assuming the process is diffusion-limited.

To achieve reasonable volumetric flows, microchannel components are scaled up by arraying a set of parallel microchannels within each unit operation to increase the cross-section of flow. Conceptually, a continuous flow reactor for producing CdS films would involve several components including a mixer, heat exchanger, residence time unit, and flow cell (see Figure 2-1). This enables the reactant stream to be introduced to the reaction surface at the peak of its reaction potential. For CdS deposition, MASD is expected to result in 1) higher yields, 2) lower solvent usage, 3) greater selectivity towards heterogeneous reaction, and 4) shorter cycle times.

1.8. Fluid distribution requirements for MASD flow cells

A key challenge for scaling up MASD is the requirement for film uniformity over large substrates, which requires that reaction conditions are uniform over the target substrate. Surface reaction kinetics are highly dependent on the reactant concentration and temperature at the reactive surface. In the case of reactants supplied as a continuously flowing fluid, the velocity at which the fluid travels determines the residence time over which the reactants have access to the reactive surface. The chart below (Figure 1-8) shows a sample film growth rate dependency of residence time (specified in legend) during experiments by Chang et al. (2009).

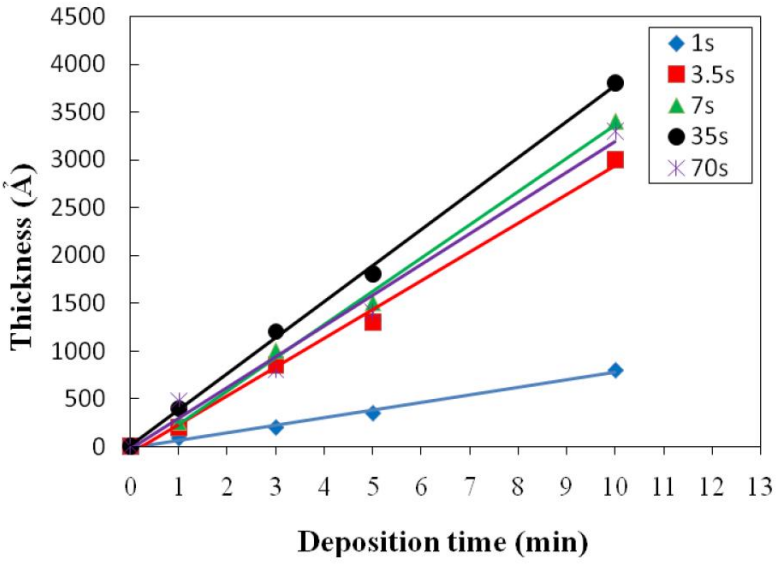

Figure 1-8: CdS thin film thickness with respect to deposition time for different residence times. [Chang et al., 2009]

The data is from tests performed with samples distributing 31 mL/min. over a coupon that measured 3”x 1”. Scale-up of this process requires much larger substrates in manufacturing which introduces the problem of maintaining constant fluid residence time across the entire surface. Faster flowing fluid will result in lower residence time contact with the target surface and a thinner boundary layer through which reactants diffuse. This difference in residence time and boundary layer thickness produces variable film thickness which is undesirable for the final cell functionality.

1.9. Flow cell designs

In a pressure gradient driven system, a challenge arises when transforming a virtual “point source” fluid supply from tubing to a uniform velocity front across a

comparatively large surface area and then back to tubing for collection. In this paper, we consider this the function of a flow cell. Various flow cell designs for managing flow distribution across a thin liquid film will be discussed.

1.9.1. Slit inlet/outlet

The basic flow cell design that is seen in most literature simply consists of two parallel plates separated by a small gap. Chung et al. (2003) presented a design for cell culture cultivation with the distinguishing feature of over-sized inlet and outlet reservoirs with the actual inlet and outlet designed as long strips instead of as a point source as seen in Figure 1-9. The large reservoirs help to slow down and distribute the fluid velocity coming into the parallel plate region, effectively reducing the lateral variation of fluid velocity.

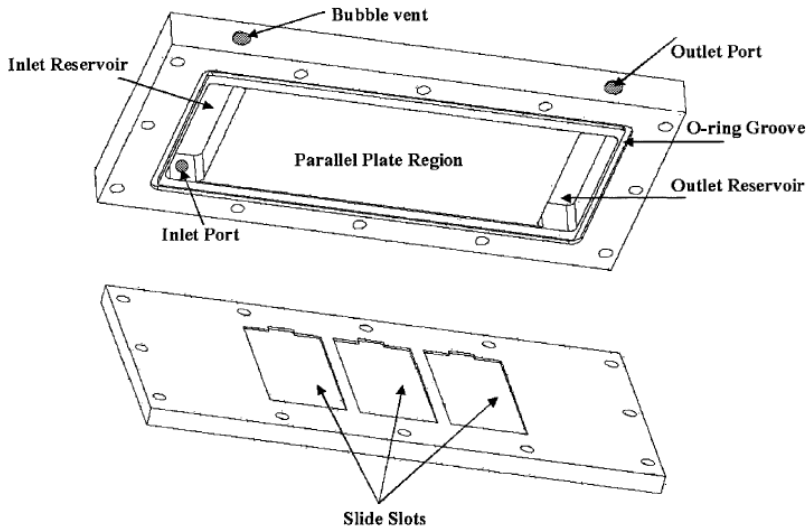

Figure 1-9: Schematic of flow chamber with inlet/outlet reservoirs. [Chung, et al. 2003]

Chung et al. (2003) shows the active area of constant shear/velocity in their flow chamber changed with 25% increase in the depth of the reservoir chamber. The schematic in Figure 1-10 shows the shear stress contours which are directly related to fluid velocity over that region. L_{en1} and L_{en2} are the distance until constant shear developed after leaving the reservoir chamber and L_{w1} and L_{w2} are the accompanying distance from the side walls for the shorter reservoir and the larger one respectively.

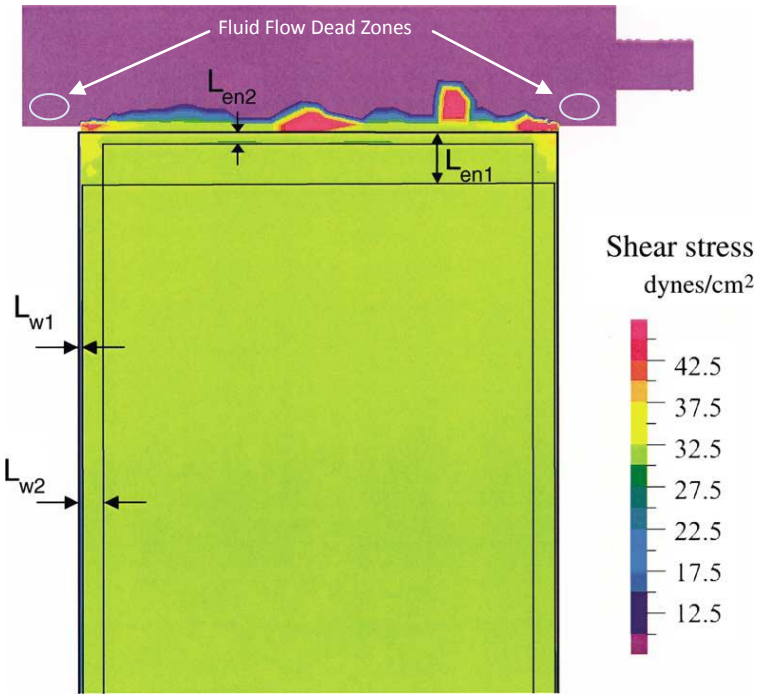

Figure 1-10: Shear stress contours of flow cells with slit inlet and reservoir. [Chung, et al. 2003]

This configuration results in more overall bulk fluid due to the reservoir chambers. This inherently reduces material utilization in reactors and tends to contain fluid flow dead zones depending on the reservoir design. For systems containing reactive species, such as those in CdS formation, there may be enough time to grow precipitates in these dead zones that may clog the device. In the field of cell cultivation certain by-products from reactions in the test area are monitored for device performance. Larger outlet reservoirs may dilute these to undetectable levels making this approach unacceptable.

1.9.2. Circular inlet/outlet

In the flow cell designed evaluated by (Jones, et al., 2008) the geometry of the inlet and outlet are circular pipes verses narrow slits. Figure 1-11 depicts the change in velocity profile between two outer wall designs, one with constricted area around the inlet/outlet points versus a more relaxed design.

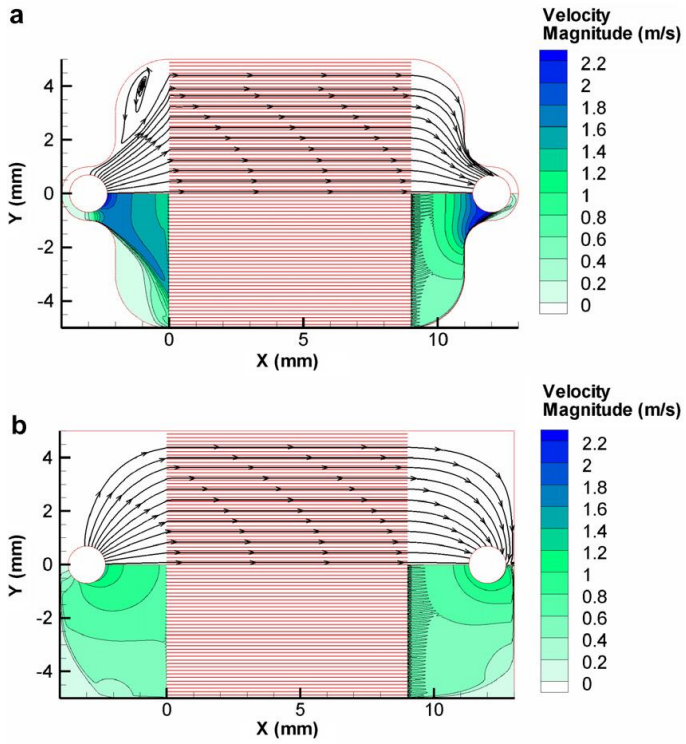

Figure 1-11: Velocity contours of circular top down inlets. (a) Constrained design around inlet/outlet. (b) Unconstrained design [Jones, et al, 2008]

Analysis realized a 4.7% difference in max velocity flux across the active area for the relaxed design and a 33.5% difference for the constrained design. This simple

change in geometry also realized a static pressure drop 32.7% higher for the constrained design. In a similar design (Bakker, et al., 2003) (see Figure 1-12) makes note to consider the distinction between velocity profiles composed of vectors pointing along the axial direction and the strong off-axis velocities magnitudes (especially near the inlet/outlet regions). This may lead to shear stresses much higher than expected if only looking at the axial velocity profile.

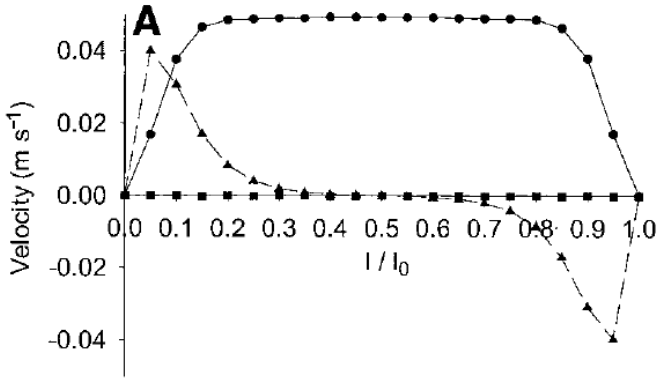

Figure 1-12: Velocity profile along the transverse flow direction. (A) Denotes velocity in off-axis directions. [Bakker, et al., 2003]

1.9.3. Circular cell

This circular flow cell was developed to provide nutrients to a culture system in a uniform and controlled manner. The cell designed by Hung, et al. (2005) consisted of an array of 10 x 10 bonded PDMS cells patterned by photolithography (see Figure 1-13).

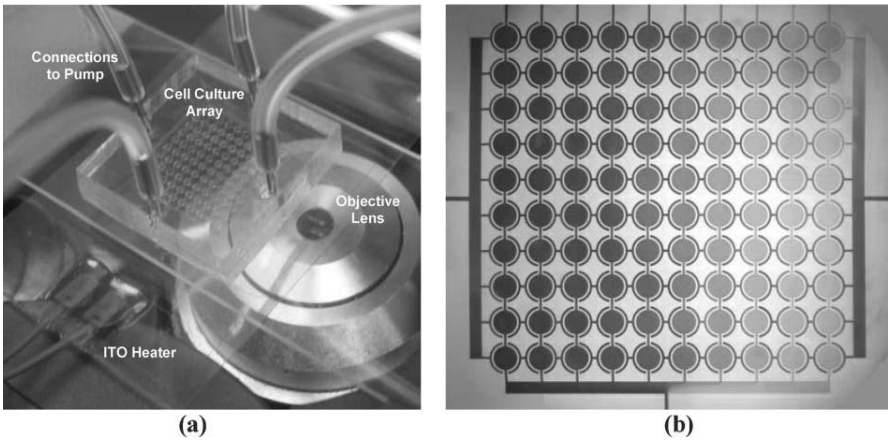

Figure 1-13: Experimental setup for circular flow cell design. [Hung, et al. 2005]

Each individual cell is designed with an inlet to deposit biological test cells that need to be maintained by a thin film of nutrient supplying fluid. The dimensions of each circular cell measure at 1 mm in diameter and 40µm in height. The 2x2 µm perfusion channels through which the nutrients enter have greatly reduced cross-sectional surface area which creates large pressure drops from the half circle inlet to the culture area. This effectively scales the fluid velocity from each perfusion down to a velocity considered uniform in comparison to the inlet velocity (see Figure 1-14 & Figure 1-16).

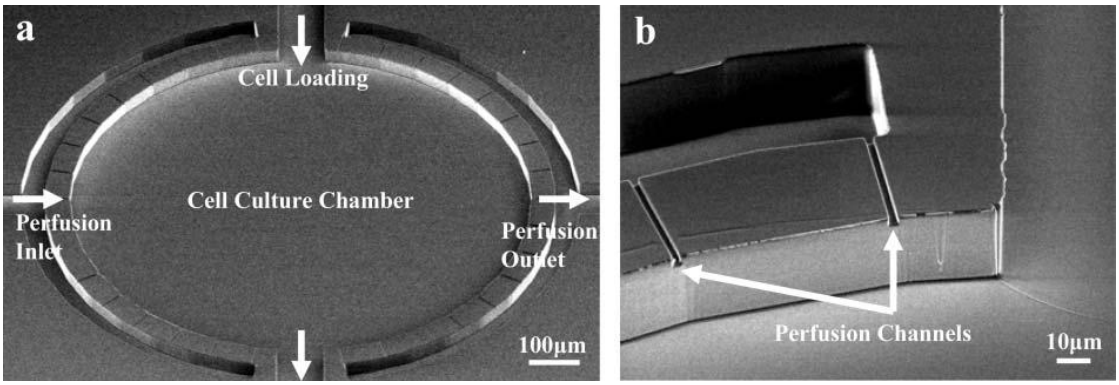

Figure 1-14: (a) Magnified view of cell chamber. (b) Magnified view of perfusion channels. [Hung, et al., 2005]

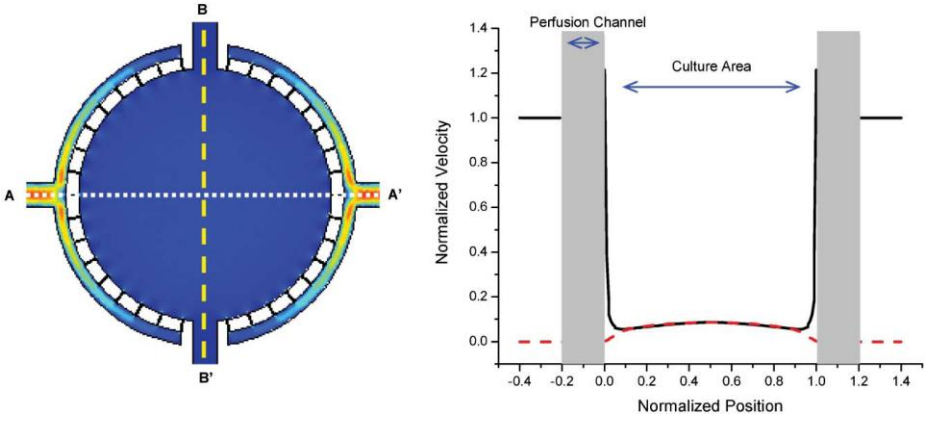

Figure 1-15: (left) Velocity contour of flow cell. (right) Normalized velocity plot from inlet to outlet. [Hung, et al., 2005]

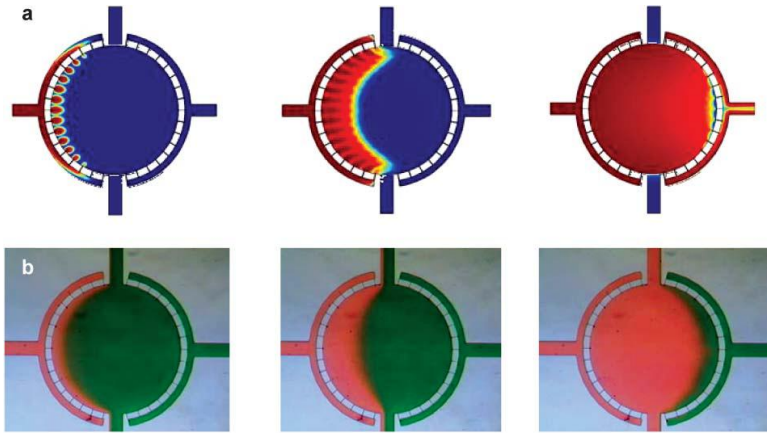

Figure 1-16: (top) Time stepped CFD simulation of fluid velocity. (bottom) Time stepped colored dye observation. [Hung, et al., 2005]

For a flow rate of .2 µm/min., this design produced a fluid velocity that varied less than 5% over 90% of the culture chamber. The associated pressure drops where not reported.

1.10. Objective

The objective of this research is to demonstrate an MASD methodology for depositing a uniform CdS film over a 152 x 152 mm surface area. This will be accomplished using a flow cell design that will provide a uniform fluid residence time profile over these large surface areas.

2. FLOW CELL DESIGN AND THEORETICAL ANALYSIS

2.1. MASD Reactor System

The overall flow design consists of separate containers for the two reacting reagents which are fed into a mixer. This stream is then fed to a heat exchanger that brings the reactants to temperature before being introduced into a flow cell for CdS film deposition. The flow cell accommodates a glass substrate and contains an integrated heating system to maintain uniform substrate temperature throughout the fluid residence time. Excess reagents and by-products are collected into a waste container from the flow cell outlet (See Figure 2-1).

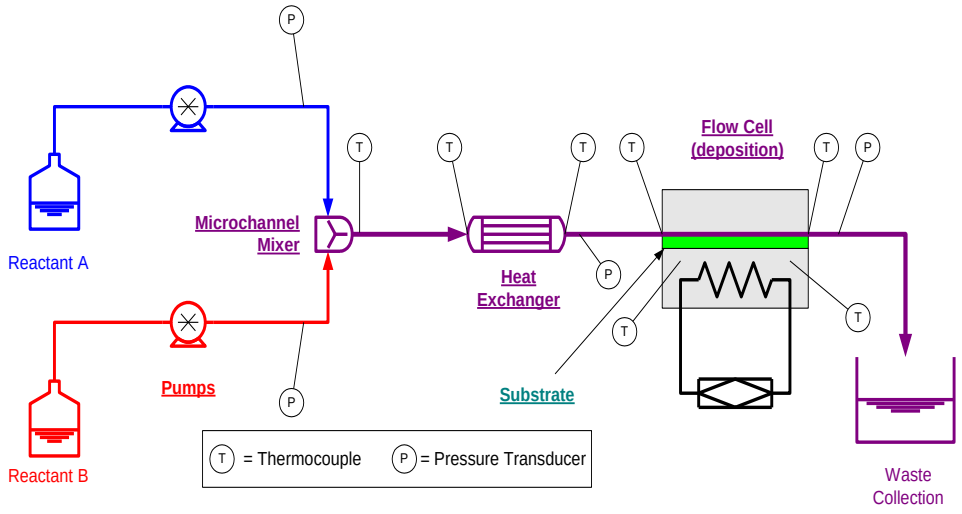

Figure 2-1: MASD test loop. [MAND Project 2008]

This system is further enhanced by implementing MASD design concepts to the mixer, heat exchanger, and flow cell. By designing the mixer with micro-scale length channels a higher amount of surface area is exposed between the combining streams,

which effectively accelerates mixing. Local pockets of unmixed reagents are reduced and quicker response in the reaction can be experienced by manipulating supply streams flow rates. This also has the potential to aid in the selectivity of heterogeneous growth over homogeneous growth by controlling the production of Cd^{2+} ions and ultimately the soluble CdS saturation. Literature has shown that this saturation has great effect on the initial nucleation rate, induction time, and onset of bulk CdS precipitate.

The kinetics for the CdS reaction is highly dependent on temperature of the reacting fluid and the substrate temperature. A micro-channel heat exchanger allows the temperature to ramp from ambient to 85 °C in an accelerated manner. This increased heat transfer allows “point of use” application of ready reactants and eliminates the need to pre-heat the reagents supplies which may cause precipitates within the mixer.

The flow cell is a constant flow system that combines macro and micro scale dimensions by utilizing a cross-sectional flow chamber with a depth less than 1000 µm and a span of nearly 200 mm. This greatly decreases the volume to surface area ratio of fluid to substrate increasing material utilization. Accelerated film growth is also expected due to shorter diffusional distances under equivalent reactant concentrations. When compared to CBD processing the constant flow allows constant reactant concentration conditions once steady state is achieved. In this system concentration of

reactants will not decrease and by-product concentration will not increase over time as in CBD processing.

2.2. Flow Cell Design Requirements

In order to deposit a CdS film of desired thickness and properties sufficient for photovoltaic operation, the flow cell must meet certain conditions. In order of priority the design requirements are listed below:

- Uniform substrate temperature – the deposition reaction rate for CdS is highly sensitive to temperature. The heating scheme must work with the material thermal properties to reduce temperature variation across the substrate.
- Uniform residence time exposure – film deposition rate is highly sensitive to reactant residence time which directly affects the concentration gradient profile experienced over the deposition surface. In a continuous flow design, the surface of the substrate is subject to variations in flow rate and subsequently variation in reactant residence time.
- Chemical compatibility with process fluids – flow cell construction material must remain inert to the film deposition chemistry.
- Accommodate 152 mm square substrate – Continuous flow deposition of CdS on large substrates leads to a wider range of application and economic feasibility.
- Minimize dead volume – the reaction mechanism produces undesirable precipitates after a certain induction period which can negatively affect film quality and

material conversion. If possible, it is desirable to keep the total residence time of any reactants shorter than the induction period. The residence time of reactants is increased within dead volumes and so could be a source of precipitate formation.

- Variable liquid film thickness (100 – 1000 μm) – MASD principles rely on small diffusional distances to accelerate mass transfer. Design flexibility is needed to operate a thin liquid film at different thicknesses to optimize reactant material utilization.
- Low pressure drop at 31 mL/min – must maintain constant flow rate without need for expensive pumping equipment.
- Optical access to interior – needed for ease of characterization and visual analysis.

2.3. Design Concept

Several design iterations were made prior to the final design and are documented in detail in Appendix A. A schematic of the final design used to meet all of the design requirements is displayed below in Figure 2-2. The overall structure is rather simple in that it basically consists of two parallel plates separated by a compressible gasket. Inlet and outlet ports on opposite ends of the upper plate allow fluid to flow through a flow cell chamber confined by the plates and the gasket. The desired distance between these two plates (100 – 1000 μm) is controlled by compressing the gasket until the top plate contacts a set of shims. The shims represent a ”hard stop” equal to the

desired flow cell channel height. A 152 mm glass substrate was accommodated by designing the entire lower plate as a single monolith of glass from which the 152 mm square area of interest could be extracted. The dimensions of the aluminum base plate are designed to accommodate a heating source and help distribute the heat for a more uniform temperature profile on the glass substrate.

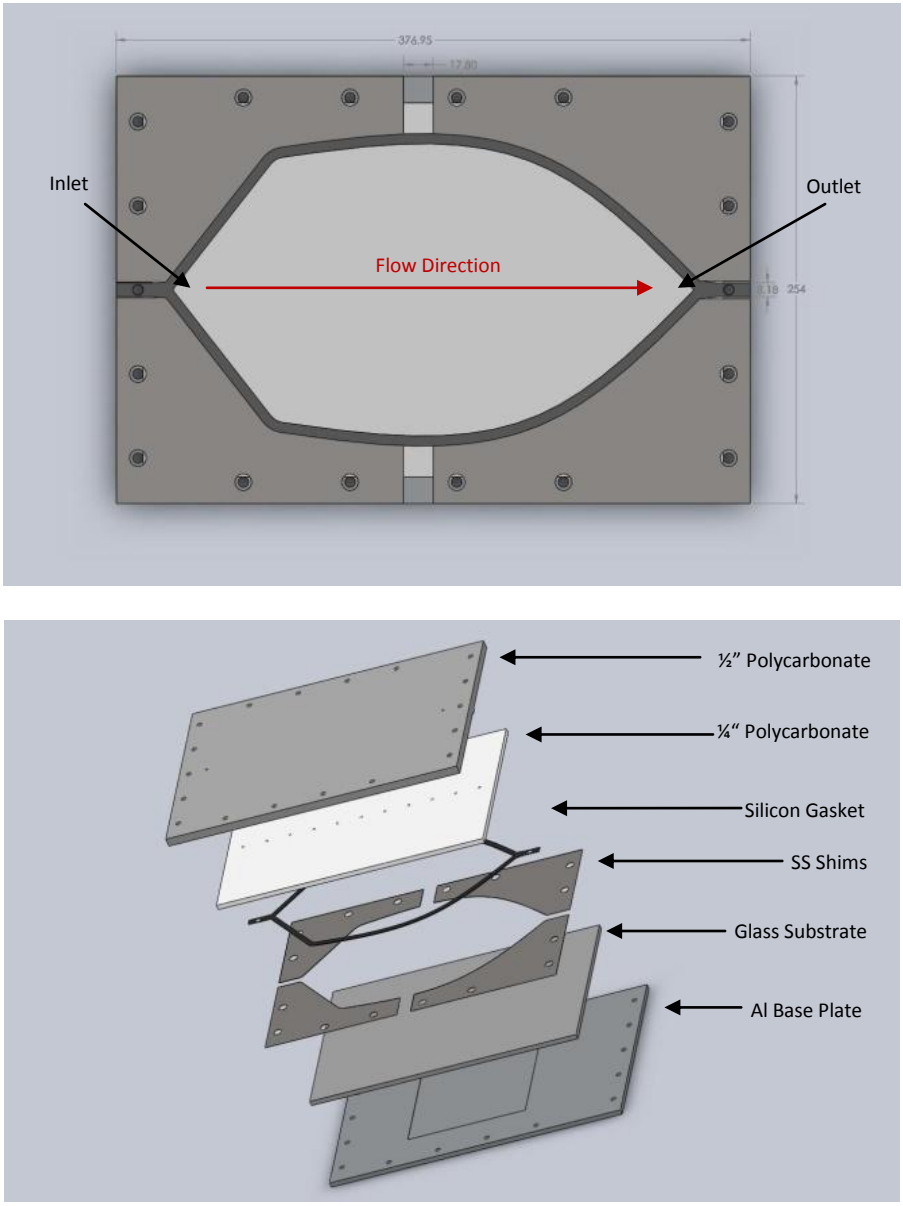

Figure 2-2: Final flow cell design (Version 6)

The geometry of the gasket reflects efforts to minimize drag and stagnant flow regions within the flow cell. The surface area of the gasket directly affects the amount of force needed for compression and was kept as thin as possible to minimize clamping

force and substrate warpage from excessive stress. The top and base plates serve as platens for compression of the gasket and inner layers. A second polycarbonate plate acts as a disposable interface with the reactive chemistry and a deflection plate for manipulating the cross-sectional area of the flow chamber. Its use is further detailed in section 2.5.3.2 below.

2.4. Materials and Fabrication

Final selection of materials included 3.2 mm and 12.7 mm polycarbonate (PC) sheet for the dual layered top plates providing optical transparency, low cost, machinability and rigidity. The plate was designed to be replaceable due to significant thicknesses of CdS which built up over time.

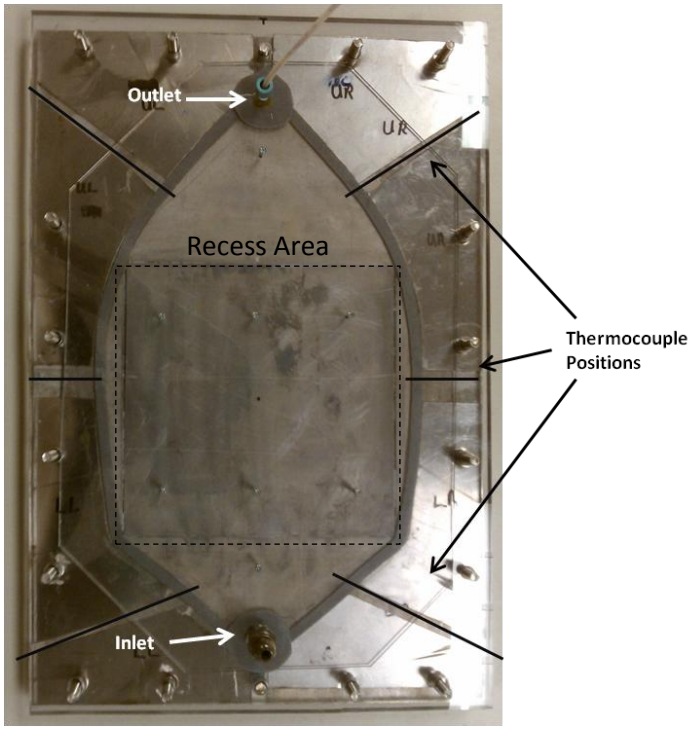

Figure 2-3: Thermocouple position in final flow cell design.

The lower base plate was constructed of 6.4 mm thick 6061 T651 aluminum (Al) alloy chosen for its high thermal conductivity, machinability, and rigidity. Initially, a 152 mm x 152 mm recess was machined into the surface to accommodate a 3mm thick glass sample as shown in Figure 2-3. Due to problems with the transition of flow between the metal and glass, the final design was simplified by using a larger glass substrate as the bottom surface of the flow channel. This eliminated the need to remove excess CdS from the Al plate. Consequently, a 152 mm square 3mm thick Al sheet was coated with thermal adhesive and placed into the recess to compensate for this pocket.

The PC and glass substrates were separated by two stacked gaskets of 1/32" (≈800 um) highly compressible closed cell silicone foam (HT-800). The distance between the plates (the height of the flow cell channel) was controlled by compressing the gaskets to the desired thickness. All experiments in this study where performed at a channel depth of 800 um resulting in a 50% compression of this stack of two gaskets. A compressive force of approximately 22 psi is suggested from manufacture's material data. Figure 2-4 outlines the compressive forces needed to control the gap distance.

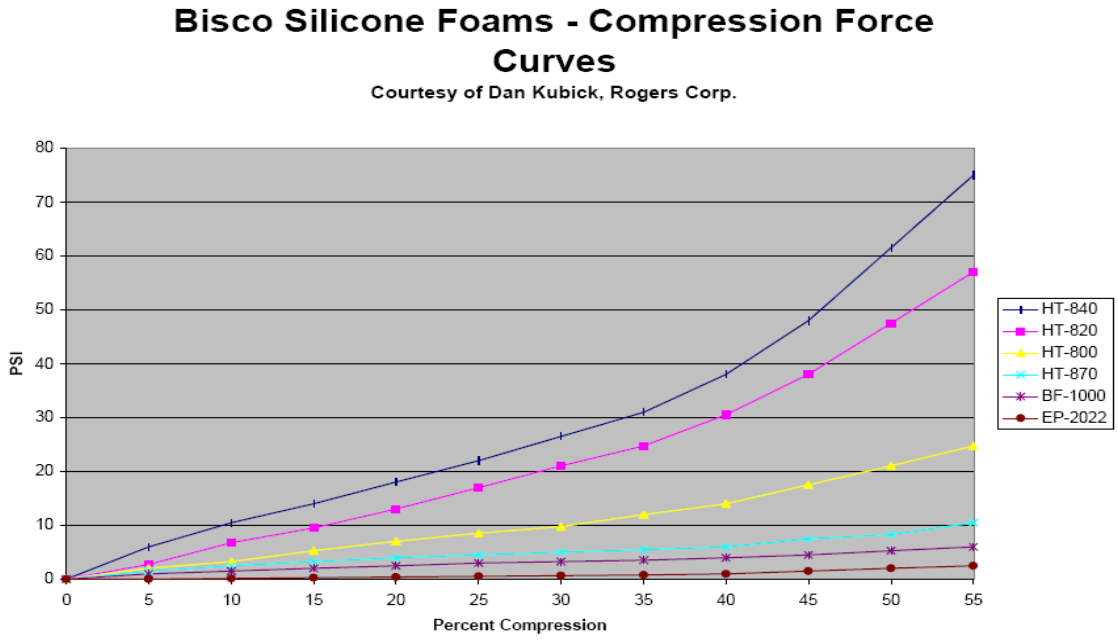

Figure 2-4: Compressibility characteristics for silicon gasket. (HT-800)

18 threaded posts (6.4 mm diameter 38.1 mm length) were mounted along the perimeter of the aluminum base for insertion into complimentary through holes cut into

the PC top. Nuts and 6.4 mm washers were used to compress the gasket down to the stainless steel "hard stops" (400 μm thick).

A 9"x 9" Wenesco hot plate (1100 W) was used to control the substrate temperature. Six thermocouples were inserted around the edge of the cell and compressed between the two gaskets allowing the tips to protrude into the flow chamber. In order to aid in sealing possible leaks from the flow chamber, silicone vacuum grease was applied to the surfaces of both gaskets. Additionally, Wakefield thermal joint compound (Type 126) was used at the Al – glass substrate interface to promote heat transfer.

2.5. Analysis of Flow Uniformity through a Flow Cell

A key requirement of the flow cell was the ability to provide uniform residence time of reactants across the flow cell. The following sections show methods used to control flow profiles in an effort to make the residence time of reactants uniform.

2.5.1. Analytical Approximations

2.5.1.1. Managing Flow Distribution

Pan, et al. (2008) characterized a microscale flow chamber composed of several parallel rectangular channels and used an electrical network parody to describe the system (See Figure 2-5). Operating under laminar conditions the pressure drop to flow

distribution between each of these channels was analyzed using the Hagen-Poiseuille Equation for rectangular channels defined below:

$$\Delta P = \frac{32\mu L\lambda_{NC}}{D_H^2}U = \frac{32\mu L\lambda_{NC}}{D_H^2 A}Q \tag{7}$$

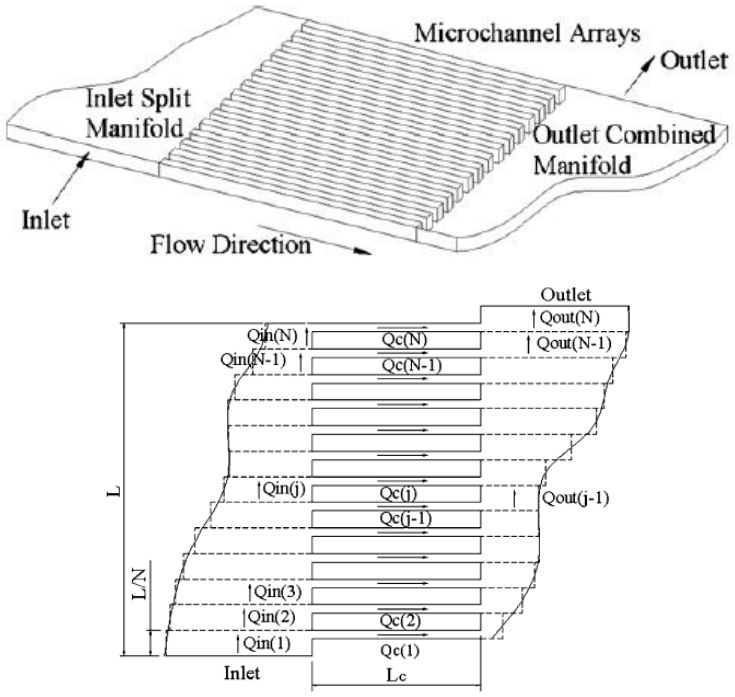

Figure 2-5: Microdevice design and analytical model [Pan, et al. 2008]

where A is the channel cross-sectional area, L is the channel length, U is the velocity, D_H is the hydraulic diameter, D_H = 2HW/(H+W); and λ_{NC} is a non-circular correction coefficient, $\lambda_{NC} = (3/2)/[(1-0.351(E/W))^2(1+H/W)^2]$ for W>H. In their model, the "loop

rule" equation V = IR used to balance electric potential is analogous to the Hagen-Poiseuille equation to balance pressure drop. Electric potential V is represented by pressure drop ΔP, electric current I by volumetric flow Q, and the electric resistance R by flow resistance defined below:

$$R = \frac{32\mu L\lambda_{NC}}{D_H^2 A} \tag{8}$$

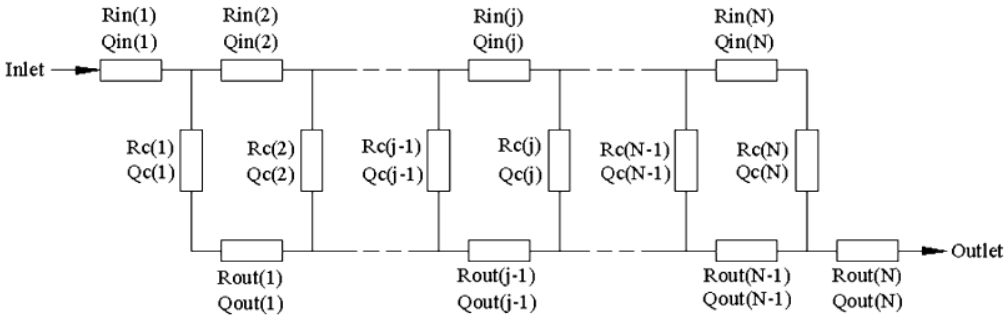

Figure 2-6: The equivalent electrical resistance model. [Pan, et al. 2008]

The basic overall resistance model assumes each channel is associated with its own unique inlet (R_{in}) and outlet (R_{out}) region resulting in a unique potential difference (ΔP) across each channel. This leads to a system of flow resistances in both series and in parallel as shown in Figure 2-6. Varying the length, depth, and number of channels allowed optimization of the inlet and outlet geometries for uniform flow distribution between each channel.

2.5.1.2. Hagen-Poiseuille Applied to a Film Deposition Flow Cell

Flow chamber designs that produce uniform flow between parallel rectangular channels have been extensively researched. A flow cell designed for uniform film deposition restricts the use of individual channels since their physical presence would disrupt the continuity of the film. This results in one large high aspect ratio channel with flow velocities changing in a continuous, rather than discrete manner lateral to the flow direction.

The model developed in this thesis for evaluating fluid flow distribution assumes that a single, wide aspect ratio channel can be described as a collection of “imaginary” channels that follow streamline pathways from inlet to outlet regions. Streamlines are imaginary lines resulting from point particles being released at the inlet of the flow chamber and tracked throughout their courses to the exit of the cell. In the case of a flow cell with physically separated channels, the streamlines would be straight along the axial path (Figure 2-7a). In the case of a single open channel, the streamlines would curve proportional to to the cell geometry (Figure 2-7b) which would increase the length of streamlines located further away from the center axis.

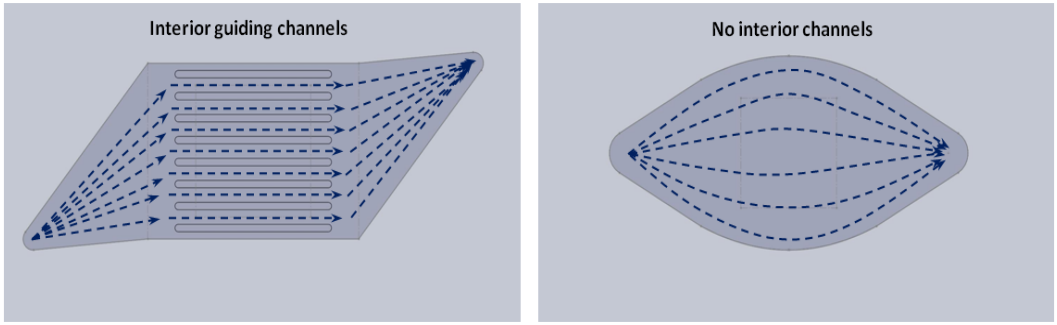

Figure 2-7: Straight streamlines vs curving streamlines

In the present analysis, it was assumed that all streamlines started and ended at the same point. This reduced the resistance network model to a simple row of channels in parallel with all paths sharing equivalent pressure drops (ΔP). For the purpose of deposition processes, a variation in fluid velocity affects: 1) the dimensions of the boundary layer and associated mass transfer to the reactive surface and 2) the residence time of the reactive molecules over the substrate. These both have direct influence on the final thickness of the film that is deposited, ultimately leading to non-uniformities across the film. In order to maintain equal velocity along each one of these channels, the Hagen-Poiseuille Equation was solved for each streamline with velocities set equal.

$$\Delta P = \frac{32\mu L\lambda_{nc}}{D_H^2} V \tag{9}$$

$$V_1 = V_2 = V_3 = \cdots \tag{10}$$

$$\frac{D_{H_1}^2}{L_1} = \frac{D_{H_2}^2}{L_2} = \frac{D_{H_3}^2}{L_3} = \cdots \tag{11}$$

$$D_H = \frac{4A}{P_w} = \frac{4(WH)}{2(W+H)} \quad (12)$$

$$H = \frac{2WD_H}{4W-2D_H} \quad (13)$$

With equivalent ΔP, the velocity of each channel can be kept equal by maintaining the appropriate D_H^2/L ratio for each channel. As L for a channel increases, the D_H of the channel must increase accordingly. For high aspect ratio channels, D_H goes to twice the channel height. Therefore, for our initial model, H was used to manipulate flow distributions.

Since streamlines increase in length as they get further from the center axis of the channel, the height of each imaginary channel for each streamline must increase in a non-linear manner according to Equations [11] & [13]. The resulting cross sectional profile looked similar to that in Figure 2-8.

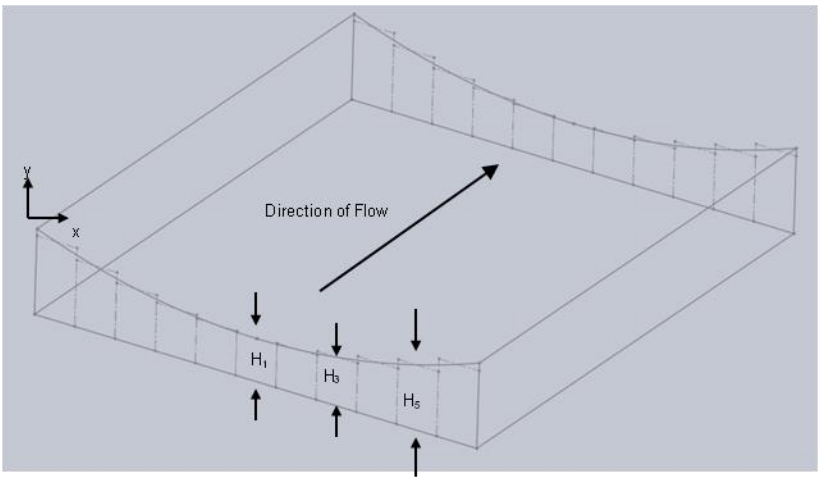

Figure 2-8: Deflected channel profile from equivalent channel heights.

By increasing the number of “channels” used to model the flow area, the width of each imaginary channel decreases approaching the profile of a continuous deflection able to maintain a flow field of constant velocity across the substrate area.

2.5.2. Thesis Statement

Demonstrate a MASD methodology for depositing a uniform CdS film over a 152 x 152 mm surface area. This will be accomplished using a flow cell design that will provide a uniform fluid residence time profile over these large surface areas. It is expected that the proper design of a deflected-plate flow cell will yield a more uniform CdS film than a parallel-plate flow cell.

2.5.3. Computational Fluid Dynamic Model

To better evaluate the precise profile geometry needed in the flow cell top plate, a computational fluid dynamic (CFD) model of the flow cell was developed. Cross-sectional profiles along nine progressive positions lateral to the flow were analytically determined using the Hagen-Poiseuille equation. These profiles were then assembled in SolidWorks 2010 and modified in GAMBIT to produce a consistent 3-dimensional model to represent the inner geometry of the flow chamber. The boundary conditions for the simulation consisted of no-slip conditions at the walls and atmospheric pressure at the outlet. Water with a density and viscosity of 9.98 X 10^2 kg/m^3 and 1 cP, respectively,

was used as the fluid. An inlet velocity of .089 m/s was calculated from the inlet area (5.849 mm^2) and volumetric flow (31.1 mL/min).

The Reynold's number at the inlet of the flow cell was found to be 1,211 which is under the 2000 value for assuming laminar conditions within the flow cell.

$$Re = \frac{\rho DV}{\mu} \qquad (14)$$

Prism shaped elements resulted from a triangular mesh applied to the top and bottom surfaces and a quad mesh to the side wall. The initial mesh divided the sidewalls into 5 segments and allowed a maximum edge ratio of 10:1 restricting the surface triangles to an edge height of 160 µm over an 800 µm high channel. The resulting mesh totaled 881,390 elements. Sensitivity of the discretization scheme was validated by refining the mesh and evaluating changes in velocity at designated points within the flow chamber. Mesh refinement resulted in 10 divisions in the channel height leading to 80 µm high elements totaling 1,763,700. The initial and refined meshes are shown in Figure 2-9.

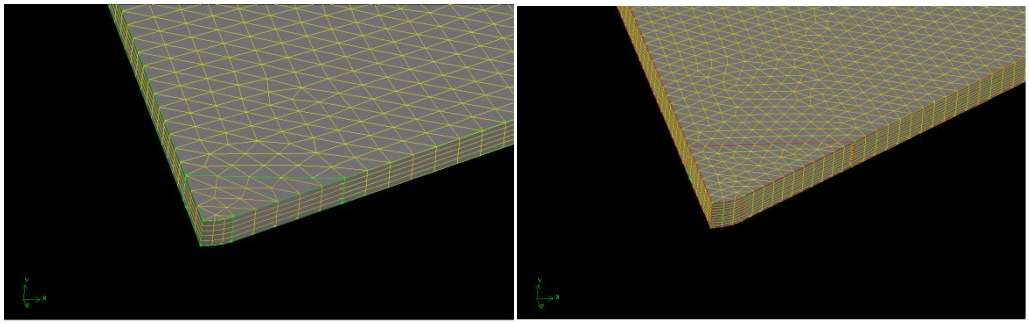

Figure 2-9: (a) Initial and (b) refined Gambit meshes for flow cell models evaluated using FLUENT.

Mesh refinement yielded a 4.3% change in predicted fluid velocity which was considered acceptable. Further decreases in element size reached the limitations of available computer resources and were not possible for additional comparison.

2.5.3.1. Baseline Model (Parallel Plates)

The baseline case to which all model results were compared was the condition of two perfectly parallel plates set at 800 µm apart. Evaluation of flow uniformity was done by calculating the standard deviation of the instantaneous velocity flow field along three different planes: The front, middle and end of the 152 mm x 152 mm substrate.

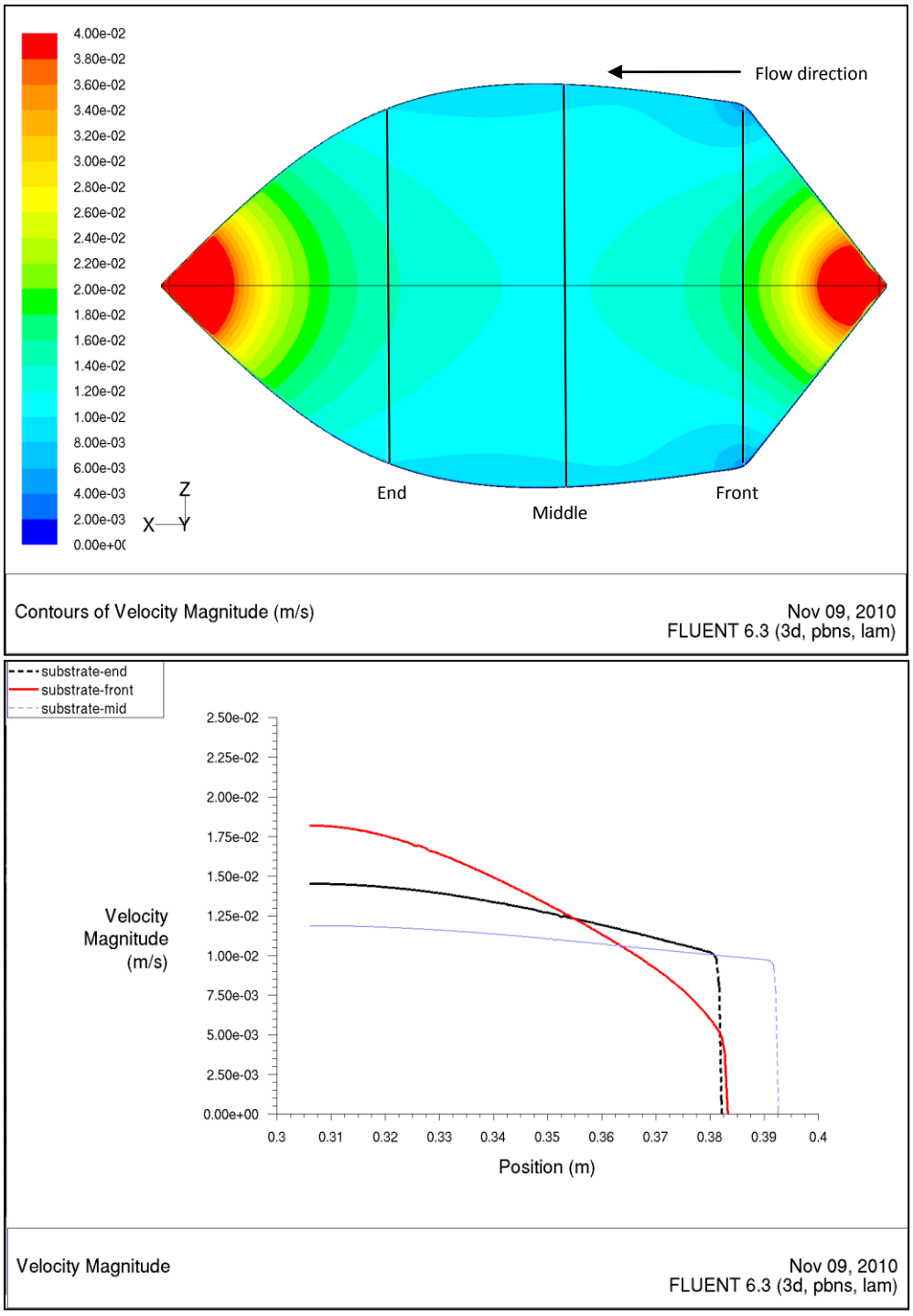

Figure 2-10: (above) Parabolic velocity contour map. (below) Velocity profile at front, middle, and ending plane of substrate position.

Simulation results for of the baseline parallel plate model produced a distinctive parabolic velocity profile near the inlet and outlet regions (see Figure 2-10). The instantaneous velocity distribution across the substrate front plane was subject to 34.4% deviation from the average velocity. This decreased to 2.4% by the middle plane and increased back to 15.1% by the ending plane.

Table 2-1: Variation in velocity magnitudes across substrate region.

	Average Velocity (m/s)	Max. Deviation (m/s)	% Deviation
Inlet	0.006428	0.002213	34.4%
Middle	0.005229	0.000124	2.4%
Outlet	0.005488	0.000829	15.1%

An estimate of reagent residence times over the substrate area was visualized by simulating a pulsed injection of discrete particles at the inlet and tracking the flow cell's ability to maintain a linear moving front across the reactive area. A snapshot of this simulated moving front as it moves through each velocity zone shows increased distortion as fluid traveled faster in central regions than outer regions. (see Figure 2-11)

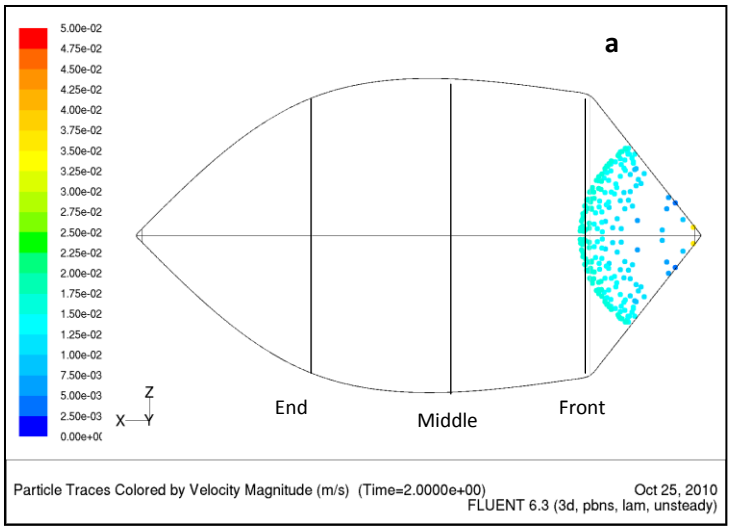
a
5.00e-02
4.75e-02
4.50e-02
4.25e-02
4.00e-02
3.75e-02
3.50e-02
3.25e-02
3.00e-02
2.75e-02
2.50e-02
2.25e-02
2.00e-02
1.75e-02
1.50e-02
1.25e-02
1.00e-02
7.50e-03
5.00e-03
2.50e-03
0.00e+00
Z
X
Y
End
Middle
Front
Particle Traces Colored by Velocity Magnitude (m/s) (Time=2.0000e+00)
Oct 25, 2010
FLUENT 6.3 (3d, pbns, lam, unsteady)

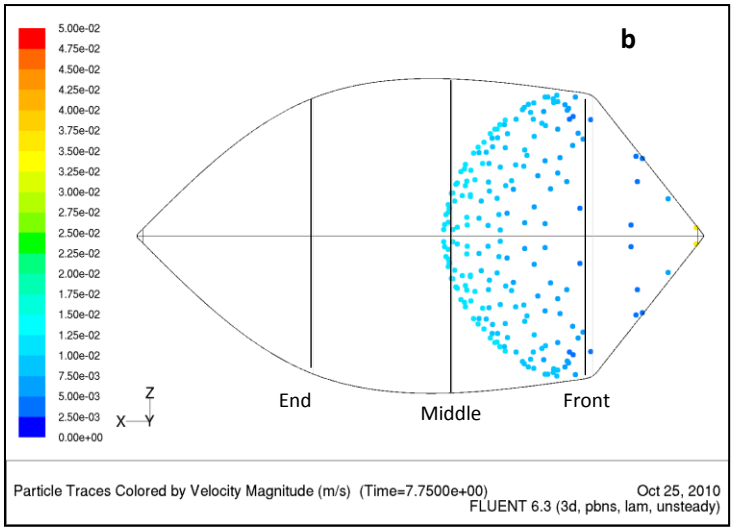
b
5.00e-02
4.75e-02
4.50e-02
4.25e-02
4.00e-02
3.75e-02
3.50e-02
3.25e-02
3.00e-02
2.75e-02
2.50e-02
2.25e-02
2.00e-02
1.75e-02
1.50e-02
1.25e-02
1.00e-02
7.50e-03
5.00e-03
2.50e-03
0.00e+00
Z
X
Y
End
Middle
Front
Particle Traces Colored by Velocity Magnitude (m/s) (Time=7.7500e+00)
Oct 25, 2010
FLUENT 6.3 (3d, pbns, lam, unsteady)

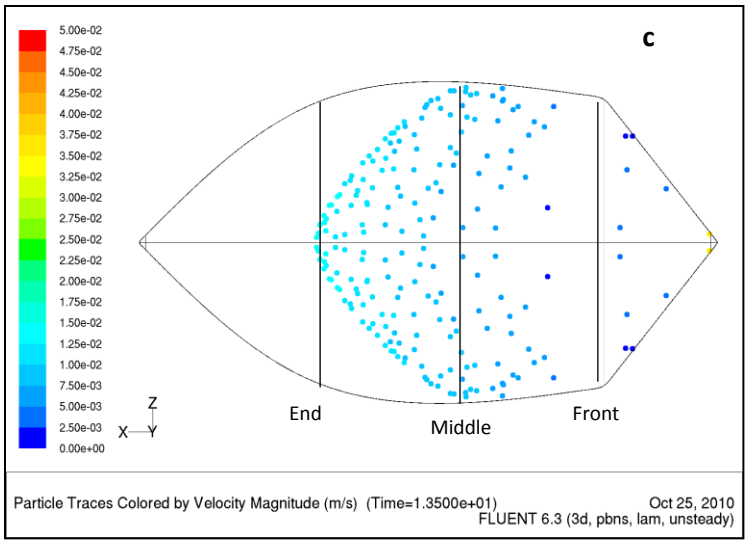

Figure 2-11: Progressive moving front profile at substrate (a) beginning (time= 2 sec) (b) middle (time=7.75 sec), and (c) ending plane (time = 13.5 sec).

The uniformity of initial flow distribution and its progression was evaluated by analyzing the X (axial flow progression) and Z (lateral position) – positions of each particle along the border of the moving front. Flow uniformity was based on the standard deviation of axial progression for all particles at the moment the first particle crossed each plane. The specific metric for flow uniformity was the standard deviation at that x-position divided by the x-position. For the parallel plate flow cell, the standard deviation of the particle position for the standard parallel plate model steadily increased as the pulse moved through the flow cell according to Figure 2-12.

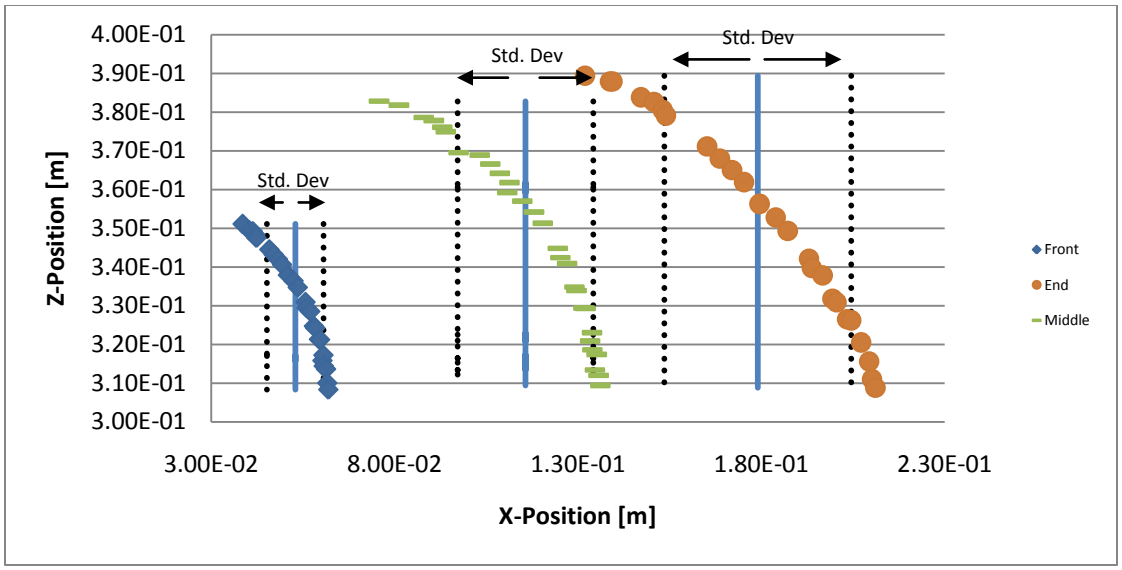

Figure 2-12: Increasing spread of moving front along axial position for parallel plates. (half model)

2.5.3.2. Deflected-Plate Models

To establish an initial profile needed to maximize flow uniformity, the base case model was used to establish precise streamlines for estimating pressure drops. Twenty-five point particles were traced using FLUENT. The resulting flow paths (see Figure 2-13) were used to construct a deflection profile as explained above. Refinements to the deflected profile were made based on the consequent velocity profile and residence time of simulated particles in CFD.

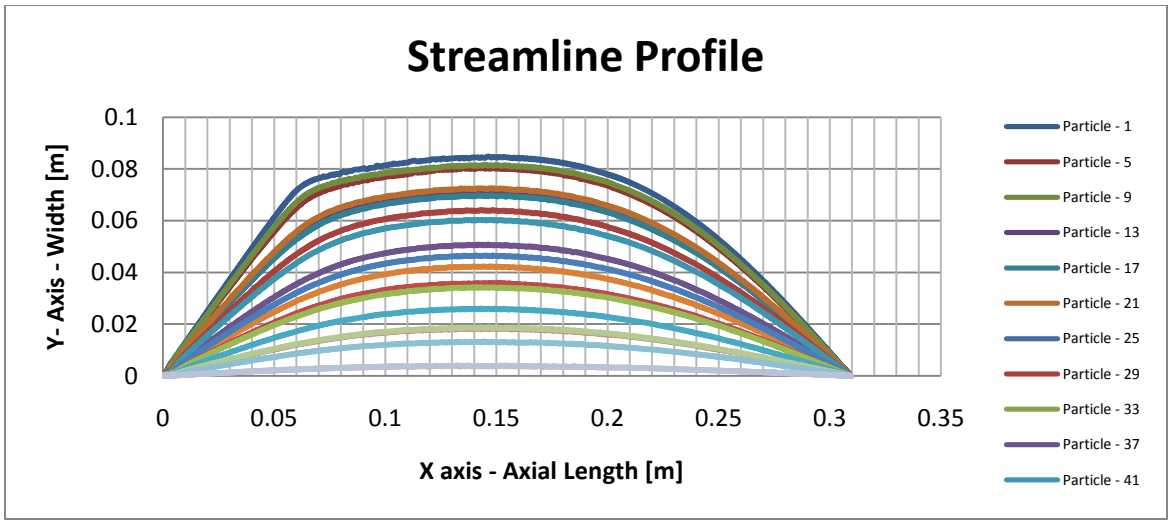

Figure 2-13: Streamline routes predicted from CFD simulation.

To ensure that the final cross-sectional profile could be implemented using a deflected plate, a series of FEA analyses were performed using a target constant centerline deflection of 200 and 300 µm based on Hagen-Poiseuille calculations using the flow paths described above. The objective of this analysis was to determine an actual deflected profile that could be used for CFD analysis. The deflected profile was based on the simulated deformation of the 3.175 mm polycarbonate (PC) plate. Each screw was simulated as a simple normal force over an area equal to the diameter of each screw and normal to the PC plate. Profile refinements included changes to the placement of screws and magnitude of the force applied within the FEA model. This was iterated until a feasible solution was found. A detailed description of each iteration and final analytical results are summarized in Appendix B.

It is important to note that the resulting deflected profile of the PC plate as a function of screw placement was the focus of this analysis rather than quantification of the forces needed to achieve these profiles. The forces supplied by these screws are a function of applied torque, friction between threads, screw pitch, and plastic and elastic deformation of the PC and screw material and are very hard to calibrate in a load cell. Consequently, the approach taken was to calibrate the actual deflected profile rather than the force applied.

A comparison of each deflection profile simulated is shown in Figure 2-14. The quantitative metric used for comparison was the standard deviation from the average axial position evaluated at the beginning, middle and ending plane for particles tracked from pulse injection. Standard deviations were normalized by the path length traveled (Front = 57.5 mm; Middle = 143.1 mm; End = 228.6 mm) to improve the consistency for comparison. Only the last two profiles are actual deflected profiles based on FEA.

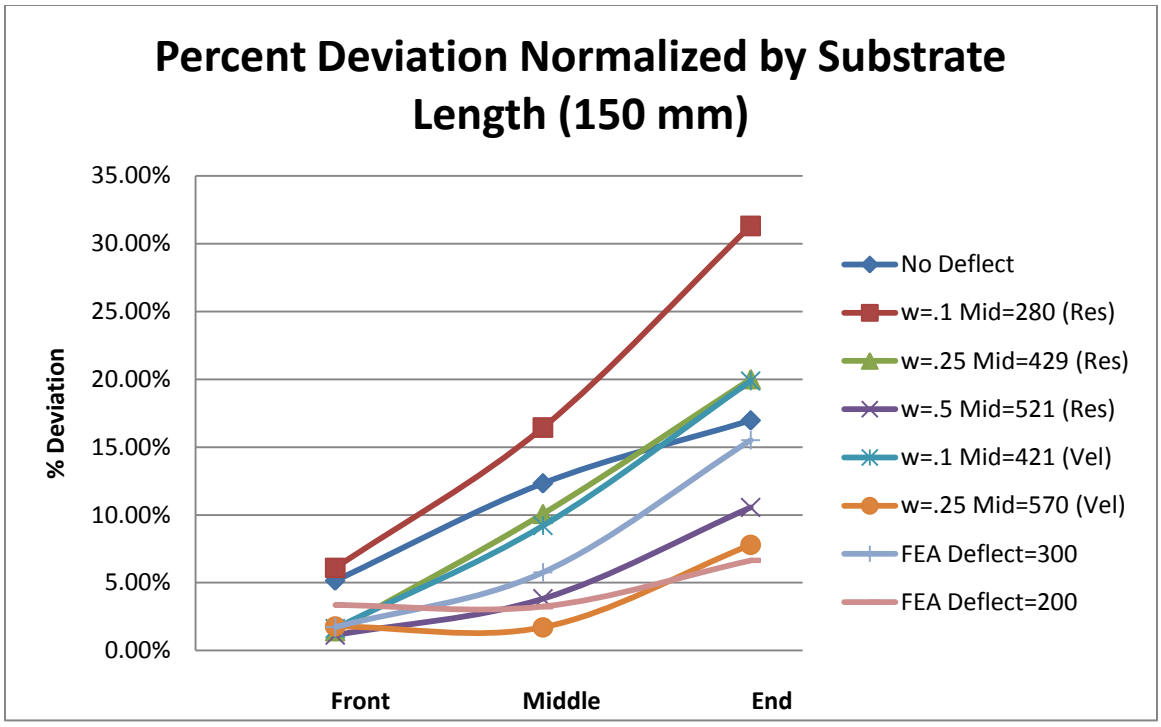

Figure 2-14: Progressive change in positional standard deviation. (Normalized by substrate length, 150 mm)

Figure 2-14 above shows that three models in particular maintained a percent standard deviation of less than 10% of the overall substrate length (150 mm) from the substrate front edge to the ending plane: 1) the constant velocity profile derived using 0.25 mm width channels; 2) the constant residence time profile of 0.5 mm width channels; and 3) the FEA profile with a constant 200 µm deflection along the central path. Of these three models, the FEA model with the 200 µm central deflection was chosen for the final experiment as it was the easiest to implement. CFD analysis results for the chosen deflection profile resulted in the flow profiles shown in Figure 2-15 & Figure 2-16 below.

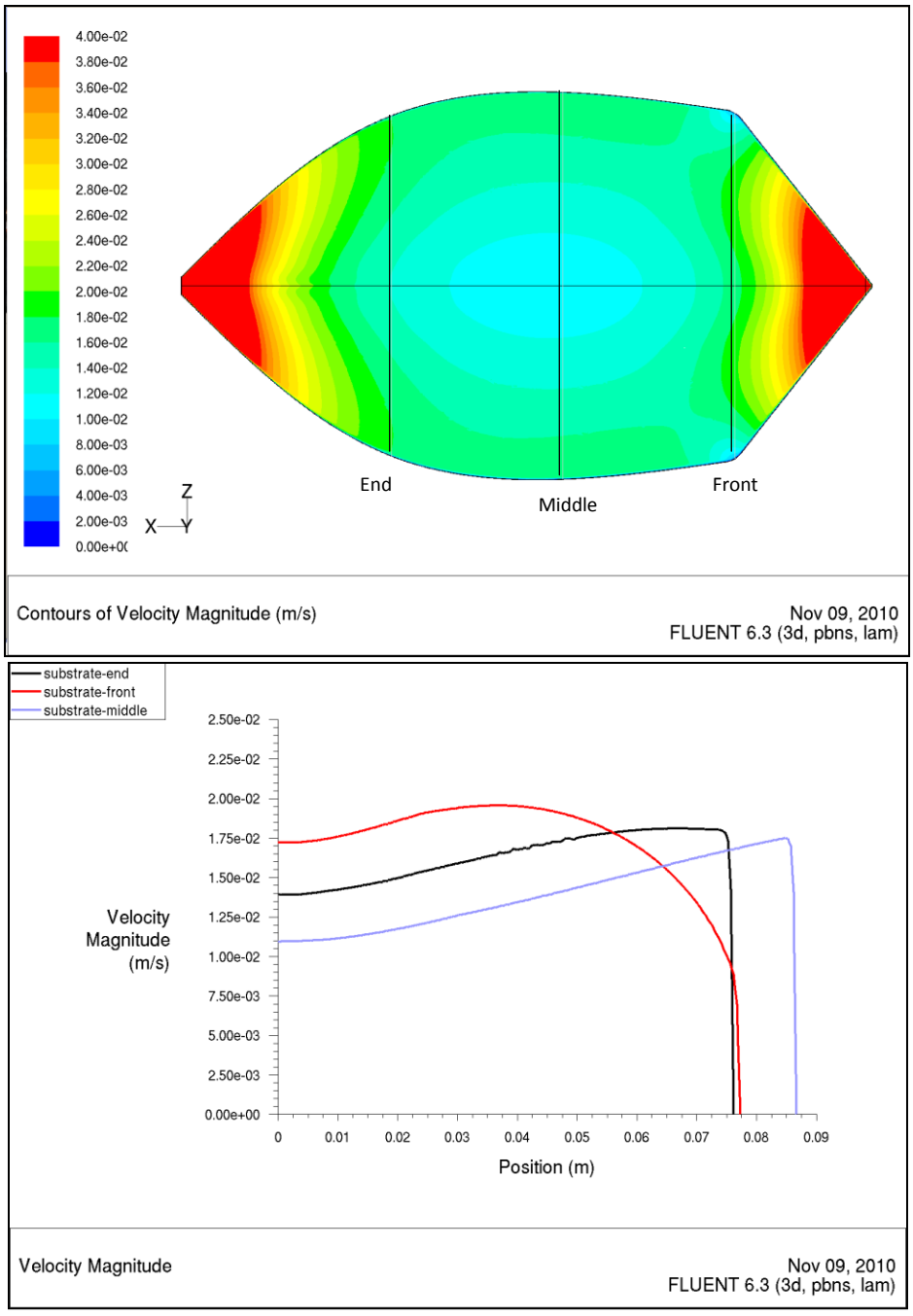

Figure 2-15: (top) Parabolic velocity contour map (bottom) Velocity profile at front, middle, and ending plane of substrate placement.

The parabolic velocity distribution shown in these figures are effectively inverted compared with the parallel plate model. Velocities are lower in the central regions and increase towards the perimeter. This compensates for the shorter distances traveled down the central streamlines effectively regulating the residence time across the flow cell.

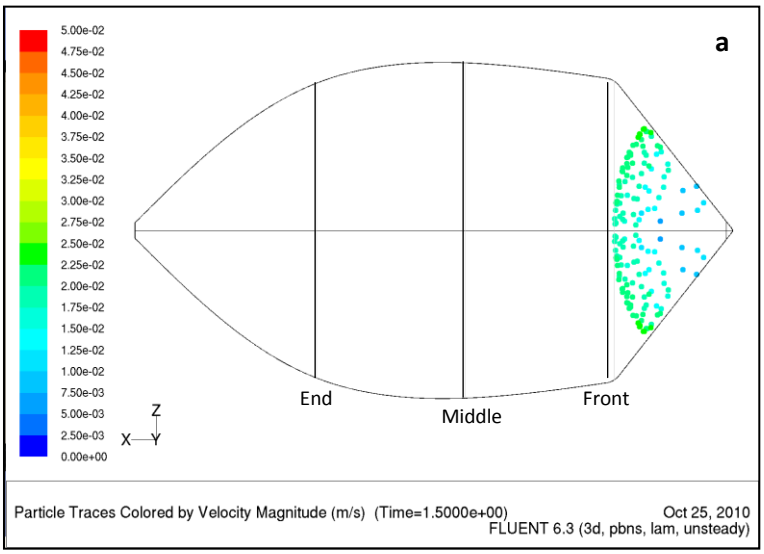

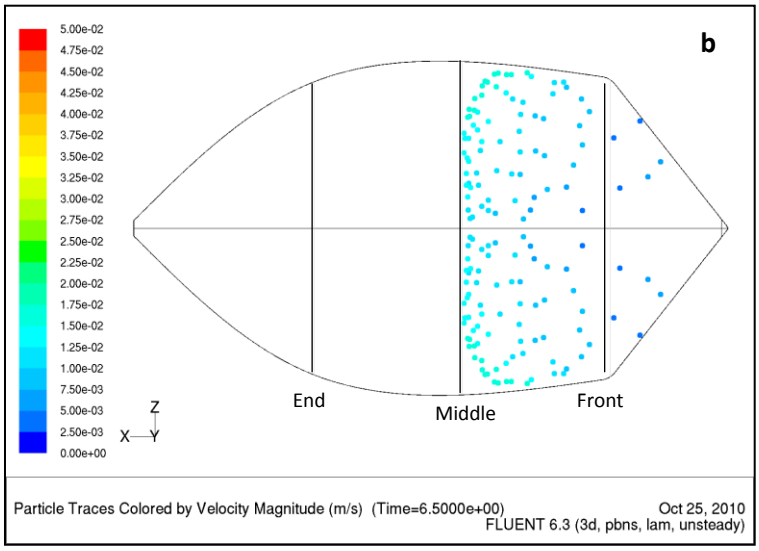

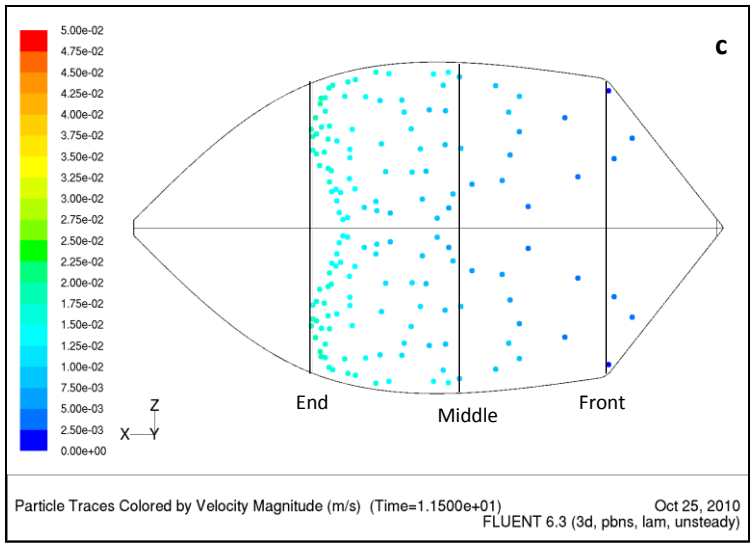

Figure 2-16: Moving front position at substrate front edge (top), middle (center), and end plane (bottom).

This is confirmed by observing the moving flow front, shown by the tracer particle plot in Figure 2-16, as it traverses the reaction (deposition) zone. In comparison to the parallel plate model, the flow front tends to maintain a more linear profile as it crosses each plane. A quantitative analysis of this dispersion shows the standard deviation has reduced by 35%, 73.%, and 61.1% for the beginning, middle and ending planes, respectively. (see Figure 2-17)

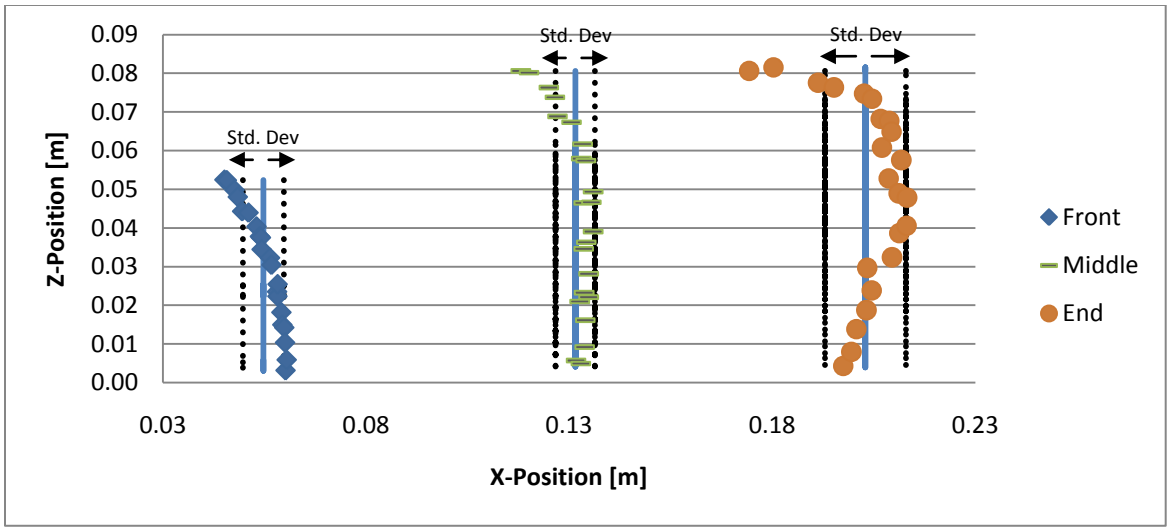

Figure 2-17: Increasing spread of moving front along axial position.

3. EXPERIMENTAL APPROACH

3.1. Overview

The final design for the flow cell underwent several iterations to ultimately meet the design requirements. The overall functionality of this design was determined by its ability to uniformly distribute reagents over the reactive area as a linear moving front. Under these conditions constant residence time is approached but variation in velocity distribution can exist depending on device geometry. This can alter the thickness of the boundary layer, length to fully developed flow (entrance region), mass flux, and shear forces in particular regions that can affect mass transfer to the reactive surface.

The model validation experiment consisted of depositing CdS in a flow cell using the dimensions of the best CFD simulated model. Measured uniformity results were

compared to a film deposited using a flow cell arranged as two perfectly parallel plates. Pulse injected dye was used to visually characterize the flow profile before deposition runs and film thicknesses were measured to assess film uniformity using UV-Vis spectroscopy.

3.2. Experimental Conditions

The flow cell was physically pressed against a Wenesco hot plate with using two Irwin Quick-Grip clamps. The surface of the hot plate measured 9”x 9” and was centered under the middle of the glass substrate area. A copper pre-heater was insulated with Kaowool and attached to the inlet of the flow cell to quickly ramp up the reagent temperature. The pre-heater was custom built and composed of two heating elements (ceramic and pad resistance heaters) and several interchangeable stacked plates capable of adjusting the internal residence time necessary to allow as sufficient concentration of secondary precursors to form. Targeted inlet temperature to the flow cell was 80 °C with a 6 sec residence time in the pre-heater. Reagents were mixed into two supply vials marked A and B with A containing 0.004 M $CdCl_2$, 0.41 M NH_4OH, and 0.04 M NH_4Cl and B containing 0.04 M of Thiourea. Equal flow rates of 15.5 mL/min. were supplied to a single T-mixer before entering the pre-heater for a total of 31 mL/min. Six thermocouples protruded into the flow stream through the silicone gasket to monitor the temperature distribution. The entire apparatus was mounted in a vertical position to allow the buoyancy of any trapped gases to exit quickly through the cell.

The flow cell was initially primed with a steady flow of de-ionized water to displace any air that may have been trapped in the system. Both pre-heater heating elements and hotplate were initiated until the pre-heater outlet temperature and thermocouple readings reached 80°C. The fluid flow supply was then switched to reagents and allowed 1 min to transverse the piping system and pre-heater to reach the flow cell. The overall deposition time was run for 5 min before all heaters were turned off and the fluid supply was switched back to de-ionized water. The system was flushed until the pre-heater outlet temperature reduced to <40°C at which time the pumps were turned off and the flow cell flow chamber was drained through the inlet connector. The top cover of the flow cell was then removed and the substrate rinsed again with de-ionized water to wash away any non-coherent particulates.

3.3. Test Setup

In order to physically implement the deflected surfaces suggested by the deflected-plate models, a test setup was needed. Requirements included the ability to manage a change in deflection from 100 to 500 µm over a 6” span in a particular profile. High precision surface milling and wire EDM were considered for construction of each surface but was ruled out due to economic considerations. A more practical solution involved controlling the deflection of the top plate of the flow cell. This was done through a combination of point displacements across the width and length of the flow cell. Screws in the outer ½” thick PC plate were used to put point forces on the inner

1/8” PC plate deflecting it into the flow channel (see Figure 3-1). To reduce set up time and minimize the number of control variables, efforts were made to use the fewest number of deflection screws. Initially, five screws were inserted into the top ½” PC plate arranged in a straight line along the flow axis. Eventually, four additional screws were added over the surface of the substrate to provide additional control over the deflection profile of the top plate within the flow cell. To evaluate the necessary position of these screws to produce the desired deflected surface, a FEA analysis was performed using COSMOS. A comprehensive list of material properties used and screw forces modeled are listed in Appendix D.

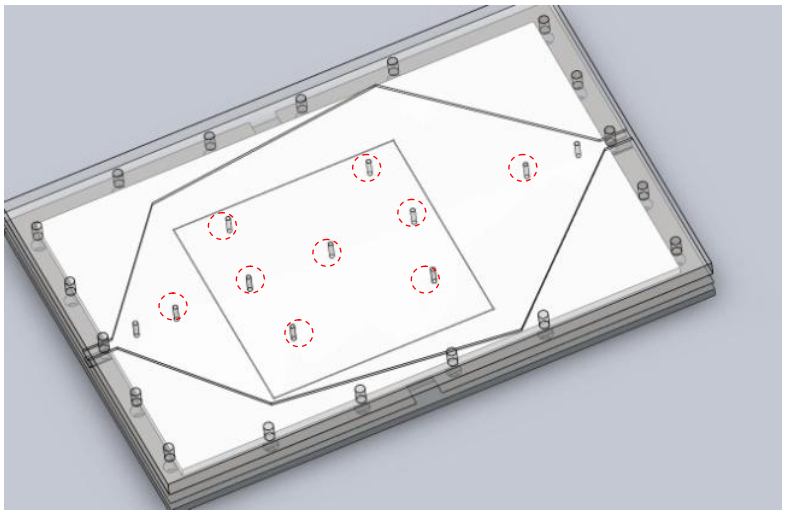

Figure 3-1: Picture of deflection screw placements.

3.4. Characterization Methods

3.4.1. Optical Laser Scanning Microscopy

Deflection profiles were calculated at seven lengths along the axial flow path: 25, 50, 100, 150, 200, 250, 275 mm. Precision in deflecting the top PC plate to this desired geometry was measured by focusing on the upper and lower flow chamber surfaces using a Zeiss LSM 510 optical microscope (5x objective). The transparency of both glass and PC made it difficult to determine features to focus on with the LSM thus small scratches where grooved along these profile lines on both surfaces. The focus dial was labeled with 180 tick marks and calibrated to move 2mm per revolution. The LSM was first focused on the lower glass substrate along a profile line and the focal point was then moved up to the desired height for that point. Next the closest adjustment screw was turned to push the upper PC plate until it came into focus. Figure 3-2 shows the final target deflection profile that was generated from FEA analysis. The channel height measured in this chart also includes displacement and distortion generated in the bottom plate. As a result, the profiles generated are not completely symmetrical.

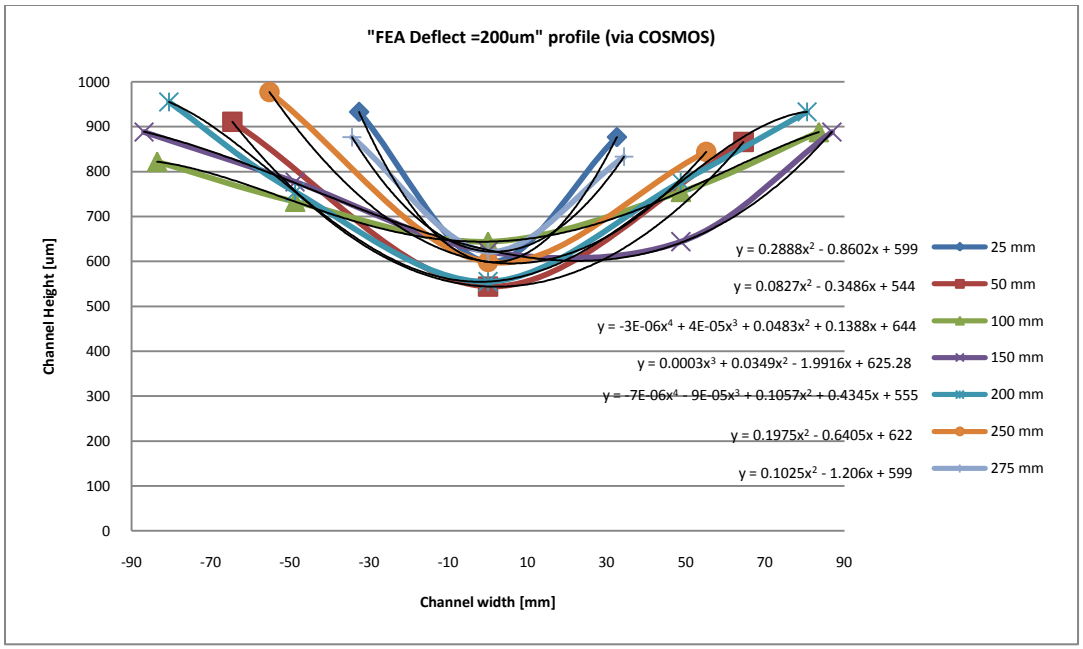

Figure 3-2: Resultant deflection profile reported from COSMOS simulation.

In order to achieve these dimensions the profiles were set starting at 25 mm and systematically adjusted until the 275 mm profile was reached. The simplicity of the design in having only 9 adjustment screw positions was expected to affect the ability to achieve high precision across along all profile lines simultaneously. In addition, the height recorded while setting a particular position is expected to change as the following points are adjusted. Appendix D lists greater detail of desired profiles, achieved profile and comparative differences.

3.4.2. Evaluation of Flow Field by Dye Injection

Prior to exposing the flow cell to the deposition chemistry, the flow distribution was optically inspected with injected pulses of concentrated food dye. This was done as an alternative to other standard high precision velocity measuring techniques such as particle image velocimetry (PIV), laser induced fluorescence (LIF), and other tagging schemes which were not available. As a result, quantitative values for velocity streams were not determined. The relative lateral positional progression obtained through the dye tests maintained sufficient resolution for our purposes. Measurement of the moving front position was done by placing rulers along the bottom and right side of the cell and measuring points from time-stamped video frames.

The flow chamber was first circulated with water at room temperature until steady state was achieved. The water supply was then switched to black concentrated food dye to visualize the moving front through the flow cell. The flow rate was set at 31 ml/min and operated at room temperature with no heat sources applied. The two experimental conditions compared were the un-deflected flow cell with parallel plates and the “FEA Deflect 200 µm” deflected model as described in section 3.4.1. The results are discussed in detail in section 4.1.

3.4.3. UV-Vis Transmission Testing

One of the primary process requirements is to deposit a 50nm CdS film with 10% tolerance in uniformity across a span of 152 mm. The focus of this study has

primarily been to control film uniformity through uniform flow distribution. Unfortunately, accurate measurement of such thin layers has proven to be a non-trivial problem. Profilometer and SEM measurements have shown that the average centerline roughness of the FTO surface is 400 +/- 60 nm which is 8x larger than the desired thickness of deposited CdS film. This roughness was much larger than originally expected and makes it impossible to use profilometry and atomic force microscopy to detect film thickness. In addition, the overall waviness of the glass substrate adds to the difficulty of defining a constant baseline for comparative measurements.

For these reasons the film thickness and uniformity was measured by exploiting the optical properties of CdS to absorb UV wavelengths (specifically 500 nm). A general relation of how film thickness relates to % transmission is accordign to the Beer–Lambert law:

$$T = e^{-\propto t} \qquad (15)$$

where T is % transmission, t = film thickness, and α is a fitting constant dependent on wavelength. A value of α = 88530 cm^{-1} was extrapolated from empirical data from Ninomiya et. al (1995) for CdS at a 500um wavelength. However, this model does not consider the effects of reflected electromagnetic radiation off of any interface it encounters. Equation (15) can be further modified to:

$$T = (R - 1)e^{-\propto t} \qquad (15)$$

where R = % reflection from the initial CdS surface. For our system there are actually four surfaces (interfaces) capable of causing primary and secondary reflection: air-CdS, CdS-FTO, FTO-glass and glass-air. A much more complete form of the transmission-thickness model with these additional reflections is possible but not considered as the general models were found to fall within a range of acceptable error (Ramprasad et. al, 2010).

As an indirect method of measurement, UV-Vis transmission is expected to be less accurate than other direct measuring methods, but is attractive due the simplicity and short time required to conduct measurements. For validation, the thicknesses of standardized film samples were measured by Yu-Wei (Wayne) Su using direct observation via transmission electron microscopy (TEM) of sample cross-sections produced using focus ion beam (FIB) machining. These values were compared with indirect measurement techniques including UV-Vis transmission and transmission/reflection as well as spectroscopic ellopsimetry (SE). TEM cross-sections were used as a standard to gauge the accuracy of UV-Vis and SE measurements (Su, Y et al., 2010).

Comparison of these measuring techniques showed that we can expect a closer correlation to FIB-TEM standard with spectroscopic ellipsometry followed by the basic UV-Vis without reflection considered and finally the UV-Vis with reflection considered.

The general UV-Vis transmission (non-reflection) model was found to overestimate actual thickness values by approximately 24.2% in the range of 20 to 70 nm.

4. RESULTS AND DISCUSSION

4.1. Velocity Distribution & Residence Time

Dye injection evaluations of flow fields within both the parallel plate and deflected plate flow cells are shown in Figures 4-1 and 4-2 below.

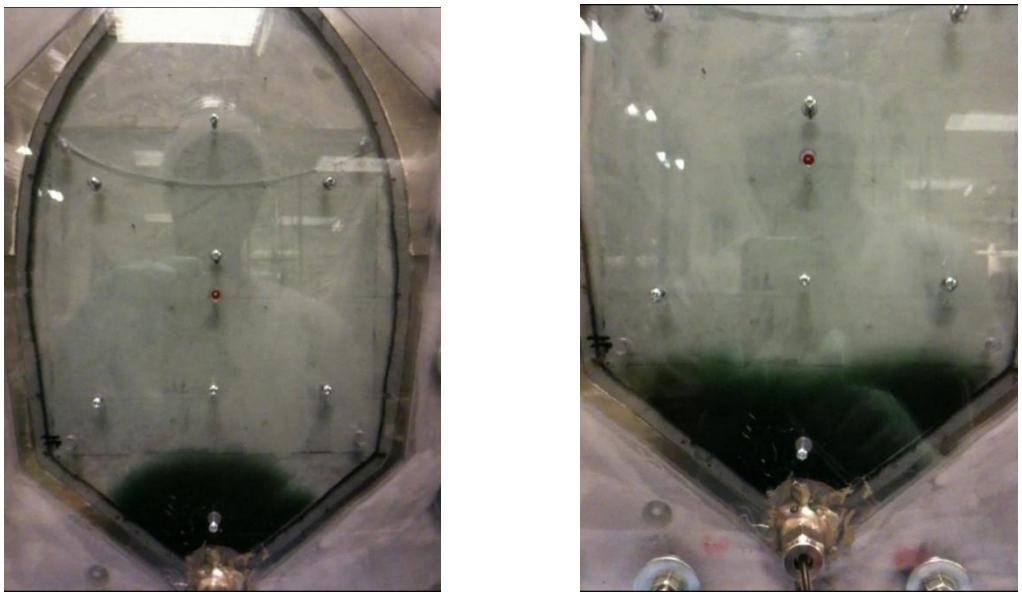

Figure 4-1: Flow distribution at the beginning of substrate (left) Parallel channels (right) Deflected top surface

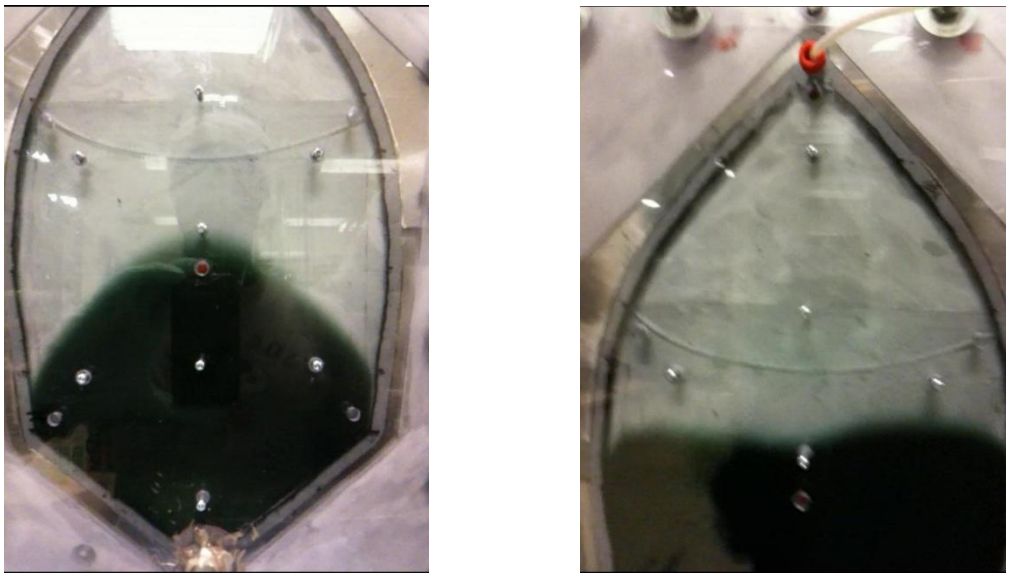

Figure 4-2: Flow distribution at the middle of substrate. (left) Parallel channels (right) Deflected top surface.

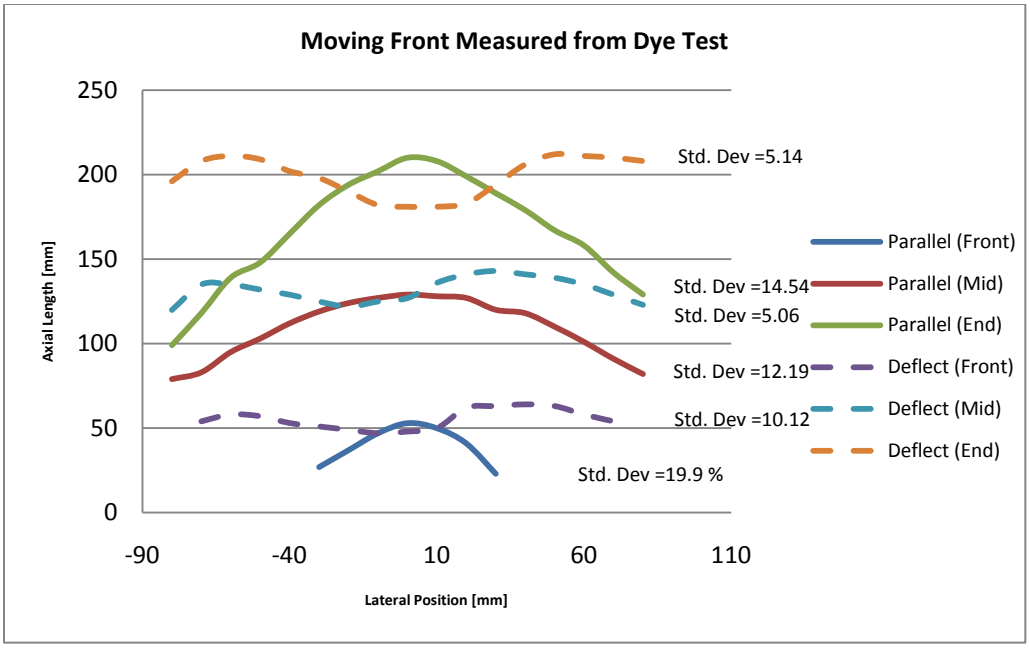

Figure 4-3: Flow distribution at the middle of substrate.

Results from the dye test were qualitatively similar to the CFD particle injection models seen earlier. The distinctive parabolic flow field is apparent in the setup with parallel plates but was dramatically reduced in the trial with the deflected top plate. Table 4-1 below shows a comparison of the flow cell performance between CFD simulations and measured dye test based on the standard deviation of the flow front position normalized by the axial path length of flow (i.e. standard deviation divided by path length). Primary sources of error between the predicted model and the dye results are: 1) Discrepancies in the physically achieved flow channel profile and desired profile. 2) Error in accurately measuring the position of the dye front which was not definitive due to diffusion. 3) Assumptions in the CFD and FEA simulation settings such as estimated material properties, symmetry plane assumptions and truncating error inherent to iterative scheme for coupled equations of state.

Table 4-1 CFD and Dye test comparison of moving front unifomity

Standardized by substrate length (150 mm)

Axial distance ------->	Front (57.5 mm)	Middle (143.1 mm)	End (228.6 mm)
No Deflection (CFD)	5.16%	12.33%	16.97%
No Deflection (Dye)	7.63%	11.63%	22.16%
Change	-2.47%	0.70%	-5.19%
% Error	32.37%	-6.02%	23.43%
200 mm Deflect (CFD)	3.36%	3.25%	6.65%
200mm Deflect (Dye)	3.88%	4.83%	7.83%
Change	-0.52%	-1.58%	-1.18%
% Error	13.44%	32.74%	15.11%

Experimental results confirm that the velocity profile can indeed be modified by manipulating the cross-sectional profile of the flow chamber. Despite the simplified methods used to deflect and measure the flow chamber profile, results demonstrate a velocity profile that reduced the % deviation in progression of the moving front from 22.16% to 7.83% by the end of the substrate.

In the converging/diverging regions of the flow cell, an inherent change in velocity occurs as the cross sectional area decreases/increases with the sloping sidewalls. This occurs because the fluid mass balance forces the average velocity to adjust as the cross-sectional area changes. Constant residence times through these zones are achieved if all fluid entering the zone reaches the end of the zone at the same time despite which streamline path it follows. In order for this to occur, the fluid traveling near the edge of the flow cell needs to travel faster than fluid traveling on axis. Once fluid reaches the reaction (deposition) zone, the flow cell plates are nearly parallel needing little or no deflection. When equivalent residence time is achieved in the inlet region, the velocity profile must be equivalent laterally across the cell to maintain uniform residence time across the substrate region. As a result, the overall deflection needed to regulate the flow ends up being much more pronounced in the inlet and outlet regions as seen earlier in Figure 3-2.

4.2. Film Thickness and Uniformity

The final films were characterized by first dividing the substrate into nine regions and further subdividing those nine regions into five subregions each. A total of 45 positions were measured for percent transmission using an Ocean Optics UV-Vis spectroscopy system.

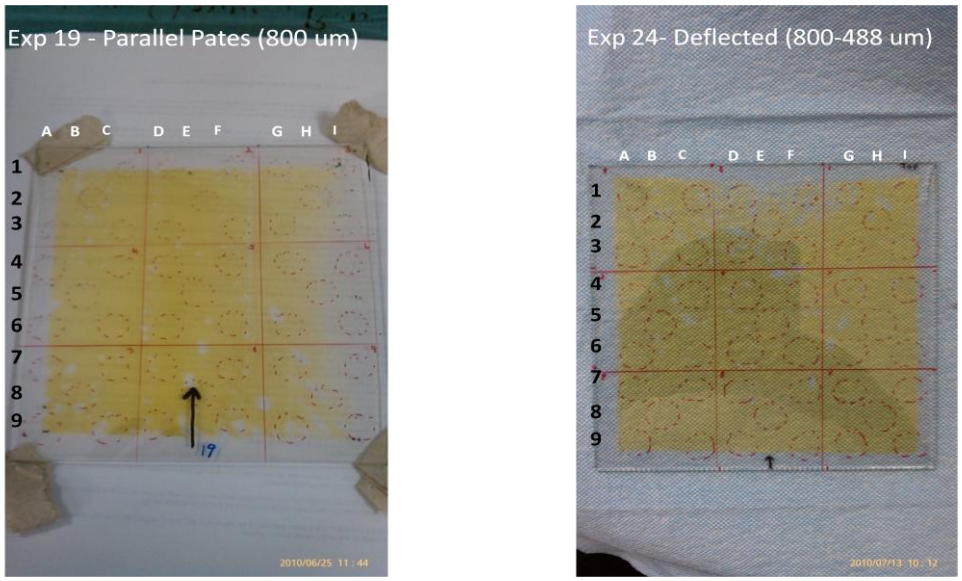

Figure 4-4: Labeling system for measuring points (left) Parallel plates (right) Deflected plates.

Complete details of transmission measurements for the parallel plate and deflected plate experimental runs are shown in Appendix F. The overall average thickness and standard deviation measured were 40.75 nm ±7.31 nm and 38.71 nm ± 22.26 nm for deflected and parallel plate conditions, respectively. This is over a 3X reduction in the variability of the film thickness. Analysis of film thickness plots across

each numbered row shows consistently lower standard deviation in measured thickness for the deflected plate flow cell (see Figure 4-5 thru Figure 4-6). CdS deposition near the end of the flow cell (Row 1 & 2) was noticeably less uniform for both films perhaps suggesting depletion of the process chemistry. More likely, based on Figures 2-16, 2-17 and 4-3 and Table 4-1, the deflection at the end of the flow cell was too severe suggesting further refinement of the flow cell is possible. Omitting these two rows reduces the standard deviation by nearly half to ±3.83nm which is less than 10% across the film for the deflected plate flow cell. For the parallel plate flow cell, it is visually apparent that film growth is thicker in the center columns (D – F) and extremely thin along columns H & I.

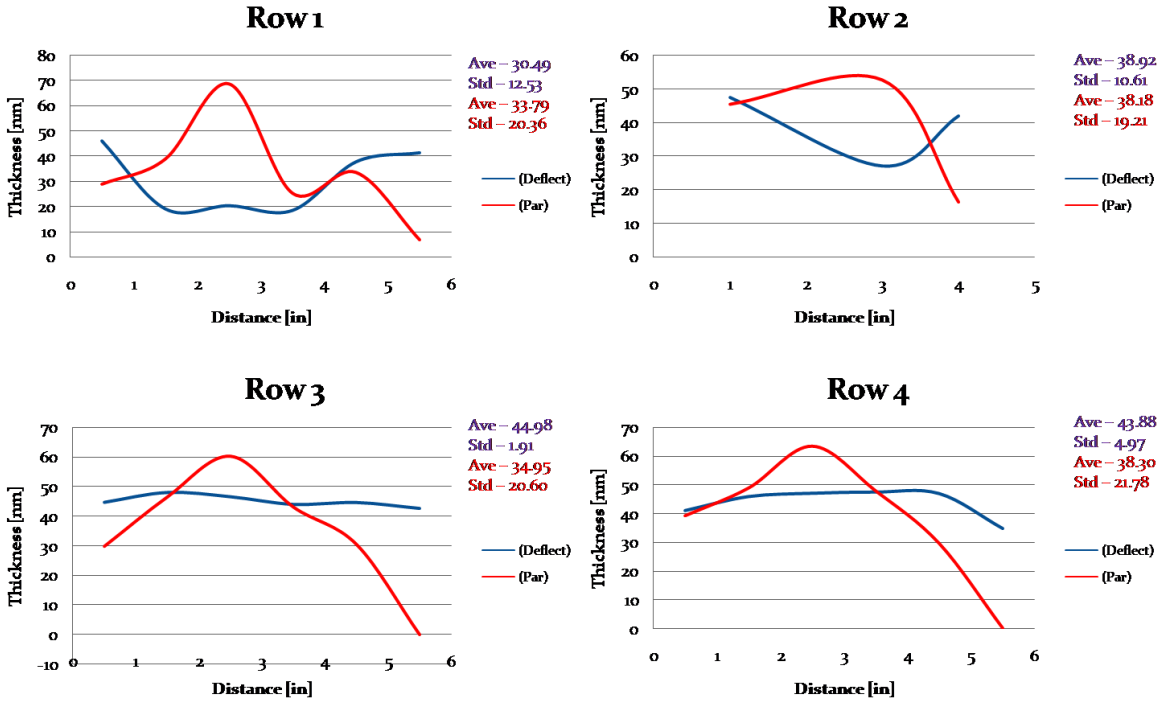

Figure 4-5: Thickness plot comparison across rows 1-4 (red) Parallel plate (blue) deflected plate.

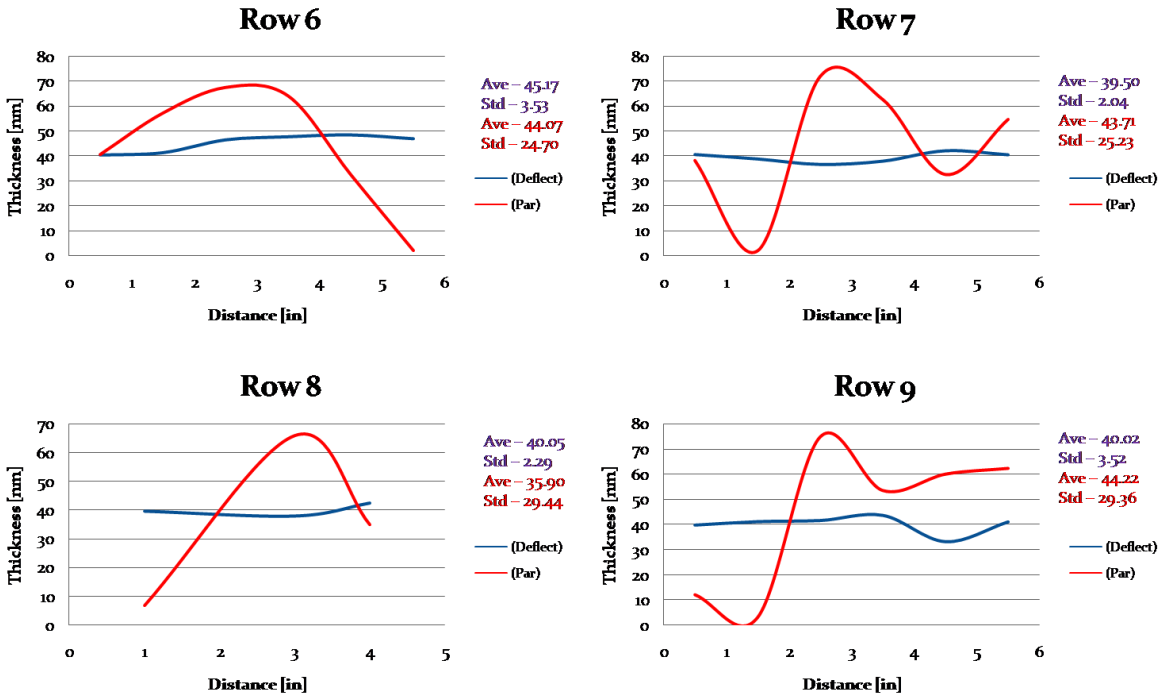

Figure 4-6: Thickness plot comparison across rows 6-9 (red) Parallel plate (blue) deflected plate.

As expected, the results from the final experiment suggest the velocity distribution has direct impact on the uniformity of the final CdS film. Under parallel plate flow conditions, the final film was expected to grow more rapidly down the faster moving center region due to a higher concentration of reactants and a thinner boundary layer. This is supported by the thickness measurements seen across each row in Figure 4-5 & Figure 4-6. The CdS was noticeably thinner along the right side of the substrate (columns H & I) compared to the left side. Possible causes for this could be: 1) a discrepancy in temperature across the substrate; 2) a contaminated surface preventing

film cohesion; or 3) an obstruction (e.g. excess deflection) near the inlet diverting flow away from the right side.

A noticeable problem that plagued both experimental runs was the formation of a gaseous phase within the flow stream. At the beginning of the deposition cycle when DI water was circulated through the cell and heaters were ramping up to reaction temperature, small pockets of bubbles were observed emerging out of solution at around 65 – 70 °C. Periodically some of these would coalesce allowing buoyancy and fluid drag to purge them from the system. However, most bubbles remained static. The effects are apparent in the final film with the presence of holes throughout the substrate.

The bubbles were believed to be a product of dissolved air in the DI water that is less soluble at higher temperatures. Several tests were done to de-gas the water prior to insertion into the flow cell by placing the water supply under vacuum for several minutes before pumping into the flow cell. However, these efforts led to no noticeable reduction in bubble formation. This may be due to the fact that the setup used required the breaking of the vacuum seal in order to insert intake leads during actual deposition runs. Another possible origin for these entrained gas bubbles could have been a gaseous by-product from reactions within the cell. The documented reaction does not suggest a gaseous by-product and the containment materials of the flow cell (polycarbonate, silicone foam) were expected to be inert based on general chemical compatibility charts.

An accumulation of these air pockets may have led to a pattern that obstructed flow in the center departing region of the deflected plate experiment and the right side of the parallel plate experiment. This arrangement was not observed during experiments.

5. CONCLUSIONS

In this thesis, a deflected-plate flow cell was developed for implementing microreactor-assisted solution deposition. The flow cell design was verified using optical dye tracers with video imaging and film thickness measurements. The flow cell was used to produce a 40.75 ± 7.32 nm CdS film over a 150 x 150 mm glass substrate. The thickness of the film deposited was found to be 3X more uniform than a film produced using a parallel-plate flow cell. This was generally accomplished by controlling the residence time uniformity in the flow cell by modifying the cross-sectional area of the flow chamber. This was most notable in the inlet/outlet regions of the flow cell where the cross-sectional area must change rapidly transverse to the flow axis. Throughout the flow cell, fluid near the central axes has a shorter distance to travel compared with fluid closer to the edge of the flow cell. Consequently, velocities must increase closer to the edges in order to maintain equivalent residence time through the region.

For the purpose of depositing films, several other factors are important to translate the fluid profile into a uniform film growth rate. The rate of deposition

depends on reaction kinetics, boundary layer thickness, diffusion rate, temperature, and concentration. Not only does the fluid velocity control the amount of time reagents have access to the substrate region, it also controls the thickness of the boundary layer. A sufficiently high velocity will reduce the residence time but will also increase the diffusion rate by reducing the boundary layer thickness. These factors were ignored in this study suggesting that the molecular residence time is a big factor in controlling film uniformity.

The film was found to have pin holes in it making it not functional. The cause of these pin holes was the evolution of small bubbles on the substrate of the device at around 65 °C in water.

5.1. Recommendation for Future Work

The investigations made in this thesis have shown that a deflected-plate flow cell reactor is feasible for depositing films tens of nanometers thick over 150 mm substrates. However, the final results and proposed model could benefit from improved design implementation and metric methods. Greater precision in producing the deflection profile could be helpful in improving the film uniformity. The current method of using "set" screws to deflect the upper surface of the flow chamber is simple but relatively inaccurate for the 400-500 μm deflections needed over a 150 mm span. An improvement on this approach could be to incorporate more set screws and use a lower modulus top plate that would keep displacements made by each screw local to their

position. It may also be possible to using high precision machining techniques to create a permanent surface profile on the PC plate or possibly even an insert that could be attached to the PC plate.

Future analysis of this design would also benefit from fluid velocity metric methods such as Particle Image Velocimetry (PIV). In comparison, a rather rudimentary method was utilized in these experiments using coloring dye as a tracer for time stamped video images. The accuracy of PIV would provide quantitative velocity magnitudes of localized positions along with the direction vector allowing a much more complete characterization of the flow field.

Finally, additional investigation is needed to eliminate the entrained gas phase during deposition. As an initial approach we believe a vacuum tight system using degassed fluids will minimize this effect. It may also be of interest to research surfactant additives that may reduce the coherence of these gas pockets to the flow chamber walls allowing them to purge through the system.

6. REFERENCES

1. Amador C., Gavriilidis A., Angeli P., Flow distribution in different microreactor scale-out geometries and the effect of manufacturing tolerances and channel blockage *Chemical Engineering Journal*; Vol. 101, 2004 p. 379-390

2. Balaji S., Lakshminarayanan S., Improved design of microchannel plate geometry for uniform flow distribution *Canadian Journal of Chemical Engineering*; Vol. 84, Dec 2006 p. 715-721

3. Bakker D. P., Plaats A., Verkerke G. J., Busscher H. J., van der Mei H. C. Comparison of velocity profiles for different flow chamber designs used in studies of microbial adheasion to surfaces *Applied and Environmental Microbiology*; 2003 p 6280-6287

4. Chang Y.J., Su Y.W., Lee D.H., Ryu S.O., Chang C.H. Investigate the Reacting Flux of Chemical Bath Deposition by a Continuous Flow Microreactor *Electrochemical and Solid-State Letters* 12; 2009 p. 244-247

5. Chopra K. L., Paulson P. D., Dutta V. Thin-film solar cells: An overview Progress in Photovoltaics: *Research and Applications* 12; 2004 p. 69-92

6. Commenge J. M., Falk L., Corriou J. P., Matlosz M., Optimal design for flow uniformity in microchannel reactors *AIChE Journal*; Vol. 48, No.2, Feb 2002 p. 345-357

7. Chung B. J., Robertson A. M., Peters D.G. The numerical design of a parallel plate flow chamber for investigation of endothelial cell response to shear stress. *Computer and Structures* 81; 2003 p. 535-546

8. Dona J. M., Herrero J., Chemical bath deposition of CdS thin films: An approach to the chemical mechanism through study of the film microstructure *J. Electrochem. Soc.*; Vol. 144, No. 11, Nov 1997 p. 4081-4091

9. Durose K., Edwards P.R., Halliday D.P., Material aspects of CdTe/CdS solar cells *Journal of Crystal Growth* 197; 1999 p. 733-742

10. Dutta D., Ramachandran A., Leighton T. D. Jr. Effect of channel geometry on solute dispersion in pressure-driven microfluidic systems *Microfluid Nanofluid* 2; 2006 p. 275-290

11. Engelbrecht C. Electricity from the Sun *Quest 2 (3)*; 2006 p. 8-10

12. Froment, M., Lincot D. Phase formation processes in solution at the atomic level: Metal chalcogenide semiconductors *Electrochimica Acta;* Vol. 40, No. 10 1995 p. 1293-1303

13. Fu R., Li D., Flow velocity measurement in microchannels using temperature-dependent fluorescent dye *Microfluid Nanofluid* 3; 2007 p. 27-32

14. Griffini G., Gavriilidis A., Effect of microchannel plate design on fluid flow uniformity at low flow rates *Chem. Eng. Technol.* 30; No. 3, 2007 p. 395-406

15. Gervais T., Klavs F. J. Mass transport and surface reactions in microfluidic systems. *Chemical Engineering Science* 61; 2006 p.1102-1121

16. Guillen C., Martinez M. A., Herrero J., Accurate control of thin film CdS growth process by adjusting the chemical bath deposition parameters *Thin Solid Films* 335; 1998 p. 37-42

17. Hoffmann W., PV solar electricity industry: Market growth and perspective *Solar Energy Materials & Solar Cells* 90; 2006 p. 3285-3311

18. Hung P. J., Lee P.J., Sabounchi P., Aghdam N., Lin R., Lee P. L. A novel high aspect ratio microfluidic design to provide a stable and uniform microenvironment for cell growth in a high throughput mammalian cell culture array. *Lab Chip*; 2005, 5, p. 44-48

19. Ito K., Shiraishi K., Preparation conditions of CdS thin films by flowed liquid film method *Solar Energy Materials and Solar Cells* 35; 1994 p. 179-184

20. Ito K., Tamaru K., CdS thin film preparation by the flowed liquid film method *Journal of Material Science Letters* 13; 1994 p. 893-894

21. Jones J. B., Lee P., Garimella V. S. Infrared micro-particle image velocimetry measurements and predictions of flow distribution in a microchannel heat sink. *International Journal of Heat and Mass Transfer* 51; 2008 p. 1877-1887

22. Kostoglou M., Andritsos N., Karabelas A. J., Modeling thin film CdS development in chemical bath deposition process *Ind. Eng. Chem. Res.* 39; 2000 p. 3272-3283

23. Kostoglou M., Andritsos N., Karabelas A.J., Incipient CdS thin film formation *Journal of Colloid and Interface Science* 263; 2003 p. 177-189

24. Nair P., Garcia V., Gomez-Daza O., Nair M., High thin-film yield achieved at small substrate separation in chemical bath deposition of semiconductor thin films *Semicond. Sci. Technol.* 16; 2001 p. 855-863

25. Ninomiya S., Adachi S. Optical properties of wurtzite CdS *Journal of Applied Physics* 78; 1995 p. 1183-1190

26. Oliva A. I., Castro-Rodriquez R., Ceh O., Bartolo-Perez P., Caballero-Briones F., Sosa V. First stages of growth of CdS films on different substrates *Applied Surface Science* 148; 1999 p. 42-49

27. Oliva A. I., Castro-Rodriguez R., Solis-Canto O., Sosa V., Quintana P., Pena J. L., Comparison of properties of CdS thin films grown by two techniques*Applied Surface Science* 205; 2003 p. 56-64

28. Orgassa K., Rau U., Nguyen Q., Schock H. W., Werner J., Role of CdS buffer layer as an active optical element in Cu(In,Ga)Se_2 thin-film solar cell *Progress in Photovoltaics: Research and* Applications 10; 2002 p. 457-463

29. Oron A., Davis H. S., Bankoff S. G. Long-scale evolution of thin liquid films *Reviews of Modern Physics;* Vol. 69, No. 3, July 1997

30. Ortega-Borges R., Lincot D., Mechanism of chemical bath deposition of cadmium sulfide thin films in the ammonia-thiourea system. *J. Electrochem. Soc.*; Vol. 140, No. 12, Dec 1993 p. 3464-3473

31. Pan M., Tang Y., Pan L., Lu L. Optimal design of complex manifold geometries for uniform flow distribution between microchannels *Chemical Engineering Journal* 137; 2008 p. 339-346

32. Ramprasad S., Su Y., Chang C., Paul K. B., Palo R. D., Cadmium Sulfide Thin Film Deposition on FTO-Coated Glass: A Parametric Study using Microchannel Microreactor-Assisted Chemical Solution Deposition *Solar Energy Materials and Solar Cells*; 2010

33. Readigo A., Garcia V., Gomezdaza O., Campos J., Nair M., Nair P., Substrate spacing and thin-film yield in chemical bath deposition of semiconductor thin films *Semicond. Sci. Technol.* 15; 2000 p. 1022-1029

34. Santiago J. G., Wereley S. T., Meinhart C. D., Beebe D. J., Adrian R. J. A particle image velocimetry system for microfluidics *Experiments in Fluids* 25; 1998 p. 316-319

35. Sinton D., Microscale flow visualization *Microfluid Nanofluid* 1; 2004 p. 2-21

36. Squires T., Messinger R., Manalis S., Making it stick: convection, reaction and diffusion in surface-based biosensors *Nature Biotechnology*; Vol. 26, No. 4, April 2008 p. 417-425

37. Su Y., Chang C., Microreactor-Assisted Nanomaterial Processing for Photovoltaic Manufacturing *US Department of Energy Industrial Technologies Program*, 2010

38. Tonomura O., Tanaka S., Noda M., Kano M., Hasebe S., Hashimoto I., CFD-based optimal design of manifold in plate-fin microdevices *Chemical Engineering Journal*; Vol. 101, 2004 p. 397-402

39. Wels C., Smith L., Beckie R. The influence of surface sorption on dispersion in parallel plate fractures *Journal of Contaminant Hydrology* 28; 1997 p. 95-114

40. Yang J., Bos R., Poortinga A., Wit J. P., Belder F. G., Busscher J. H. Comparison of Particle Deposition in Parallel Plate and Stagnation Point Flow Chamber. *Langmuir* 15; 1999 p. 4671-4677

41. Zheng X., Silber-Li Z. Measurement of velocity profiles in a rectangular microchannel with aspect ratio α=0.35 *Exp Fluids* 44; 2008 p. 951-959

7. APPENDICES

APPENDIX A: Design Concepts

I. Version 1

The first version intended to confine fluid flow between two flat plates outlined and separated by a sealing material. The inlet consists of a 1/8” tubing connection which diverged at a 7° angle to a 6.5” substrate chamber. At the 7° angle the loss coefficient for sudden expansion of fluid in a pipe is at a minimum. The substrate chamber contained a .5mm inset to accommodate a 6” circular substrate leading to an open end outlet weir that would overflow to a waste container.

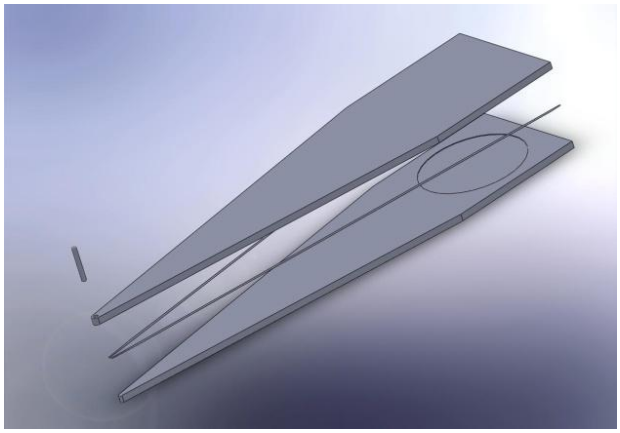

Figure 7-1: Version 1 concept

This concept was rejected due to the overall size of the cell expanding from 1/8” to 6.5” at 7°. At a total length of 828 mm (2.7ft) complications arise in the cost of building materials and available heating elements capable of maintaining uniform temperatures throughout the length of the cell.

II. Version 2

Version 2 modifications include a change of the substrate dimensions from 6” circle to 6” square and an overall reduction in cell size. The bulk of the diverging inlet in version 1 was replaced by a thin accumulation manifold feeding a micro channel flow distribution scheme at the substrate edge. This design proposed the top surface of the micro channel features to be fabricated into the top plate of the cell and complementing features etched in to the bottom plate. Separation of the two plates would determine the gap between both the microchannel region and the substrate region. A soft (spongy) sealing material would be expected to seal the sides and the gap distance would be controlled by hard stops of known thickness place at each corner of the cell.

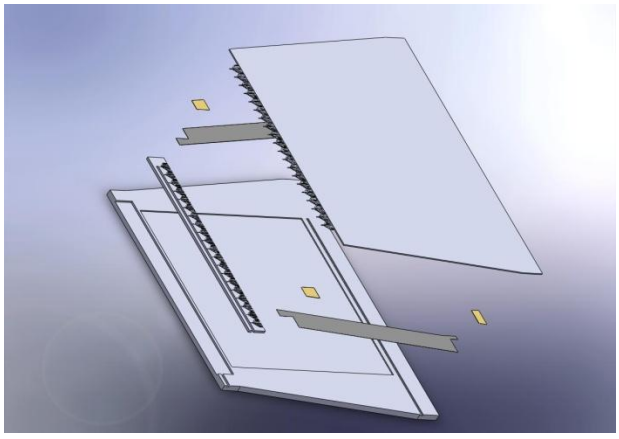

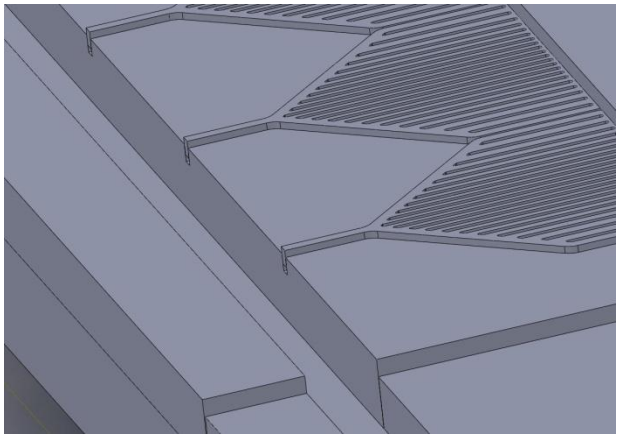

Figure 7-2 Version 2 concept (top) Exploded view (bottom) Microchannel distributor design close-up.

This concept was not implemented due to the complexity of fabricating the micro channel distributor design into the top and bottom plates. Dead-zones were also expected to be problematic with the accumulation manifold which would lead to bulk fluid particle formation and clogged micro channels. A final concern was clearance and the resulting sealing scheme that would be needed between the top and bottom plate in the micro channel region.

III. Version 3

Version 3 was a design focused on simplicity and intended to provide a working platform for initial deposition trials. The diverging angle on the inlet manifold area was increased to 52° to keep the overall length reasonable. A sheet of highly compressible foam gasket was used to seal the flow perimeter. Four clamp posts are arranged on two

sides of the cell to compress the gasket between the top and bottom plate. Two strips of hard stop shims are located along the clamp post region to control the gap distance between upper and lower plate. Additional features to reduce or correct the velocity profile were not considered in this design.

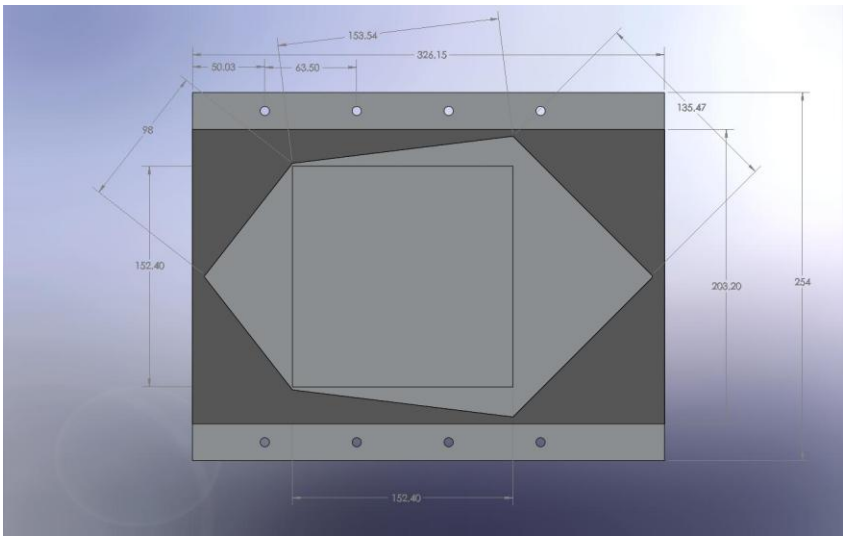

Figure 7-3: Version 3 design

Concern for stress distribution of clamp post and resulting shape of top and bottom plate where of concern and thus addressed before implementation.

IV. Version 4

Version 4 marks the first physical construction of the flow cell to be run tests. It consist of minor modification of version 3 adding clamp posts to all four edges of the cell

for increased uniformity in compression force distribution. The size of the gasket area was also decreased in order to decrease the amount of force need to compress the gasket to desired dimensions.

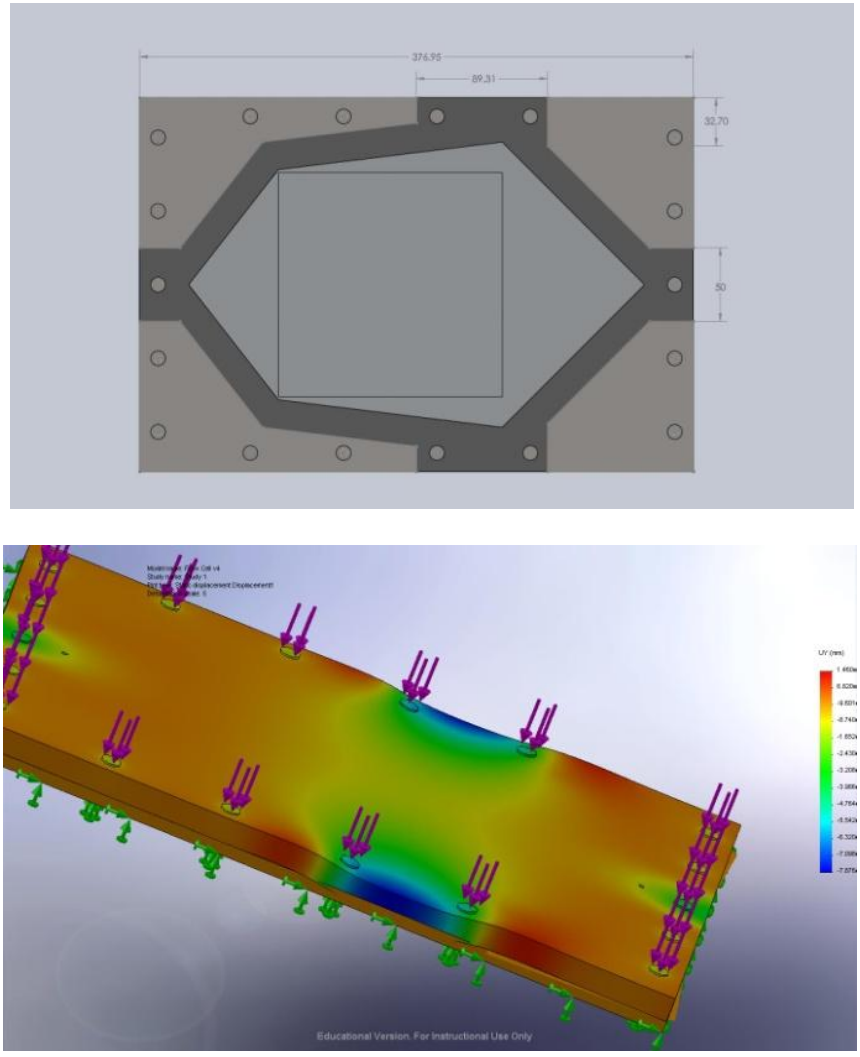

Figure 7-4: Version 4 design. (top) FEA analysis of von mises stresses distribution. (bottom)

For registration purposes the sheet gasket was extended around six different clamp post but FEA analysis showed this configuration caused an increased amount of deflection in the upper plate. Having gasket material directly below the clamping spots provided much less support than the shim stops next to it leading to a distortion in the parallelism of the two plates.

V. Version 5

Modification in Version 5 included complete removal of gasket material from underneath four clamp post positions. For registration the gasket was kept around two posts along the axial position but the area was reduced. Previous version had maintained the 7° divergent angle after the 52° inlet manifold to help effects of sudden expansion on the resultant flow profile. Further consideration of this effect along with simulations and empirical observation showed that while a diverging channel could reduce overall reduction in average velocity the velocity distribution would not be more uniform and was thus omitted in this version. As an alternative the simulations run on this model modified cross-sectional geometry of the flow cell to compensate for non-uniformity lateral velocity distribution.

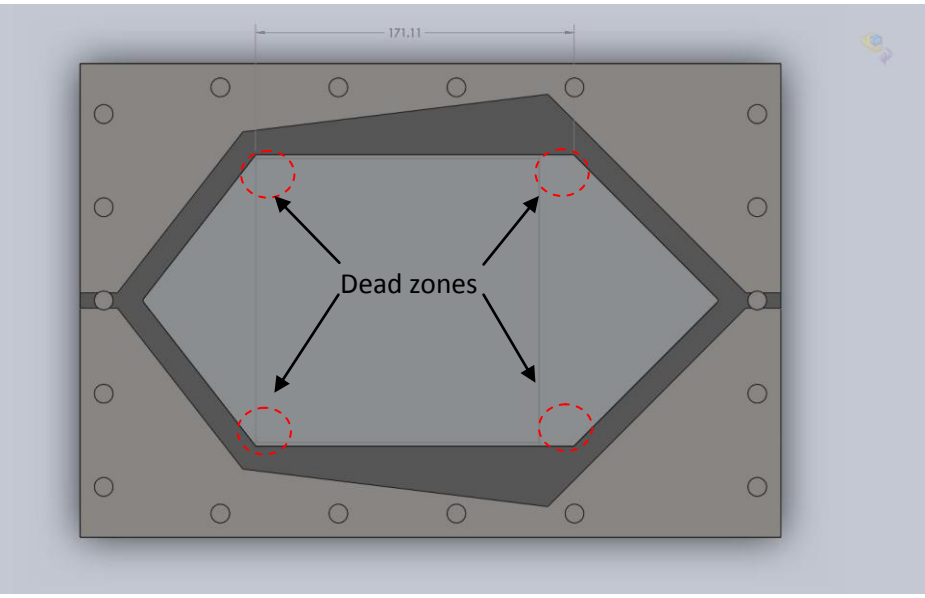

Figure 7-5: Version 5 Flow.

Simulations run using this version showed significant dead zones in the sharp corners of the cell that needed to be addressed in future versions.

VI. Version 6

The sharp corners of the flow chamber where smooth as much as possible in the final version to reduce the stagnant flow regions seen in version 5. Test run on previous versions showed that after placing the substrate in the recess cut into the bottom plate a significant gap existed that disturbed fluid flow. To eliminate this and simplify construction the design was modified to use a substrate that covered the entire flow region. This provided a continuous surface for smooth fluid flow but required the 6” square area of interest to be cut from the substrate plate after deposition.

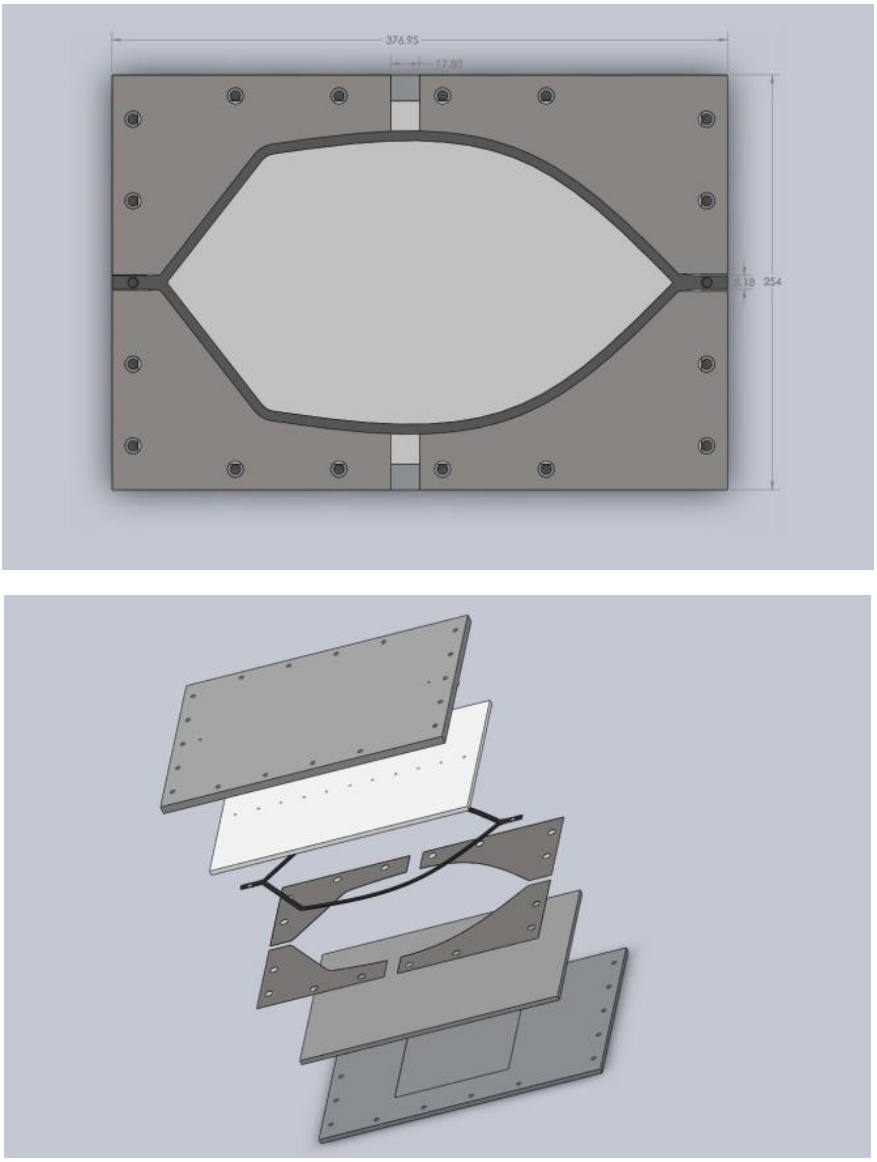

Figure 7-6: Version 6 Design (top) Top view. (bottom) Exploded view.

Papers in the literature review modified regions such as front/back end manifolds, perimeter dimensions, and inlet/outlet placement to control non-uniformity in lateral fluid velocity distribution. This version modifies the cross-sectional geometry of the flow chamber by adding another full length plate between the original top plate

and the gasket material. This served as a plane that could be easily deflected to suppress fluid flow at key regions. To reduce the amount of compressive forces needed to reach desired gap distances the gasket area was reduced even further from version 5.

APPENDIX B: CFD of Preliminary Deflection Models

The initial CFD analysis of the flow cell originated using the version 5 geometry. Two parallel plates set at a distance of 800 µm apart is the standard by which each analytical deflection model is compared. The velocity contour map for the standard is a result of a 31ml/min flow rate and is shown in Figure 7-7. The velocity across the front, middle, and ending plane of the substrate was plotted and evaluated to determine the fluid velocity distribution. The standard deviation of velocity at each of plane is displayed in Table 7-1. Notable regions of stagnant low velocity areas are seen in the corners of the flow cell. Some stagnant regions were found near the corners which reduced the lower range and overall average.

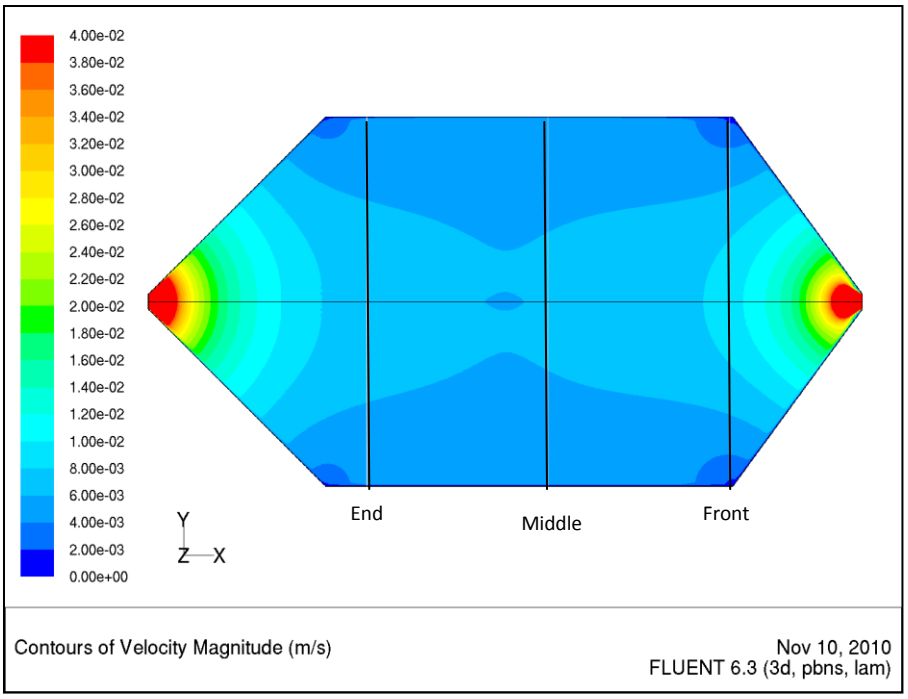

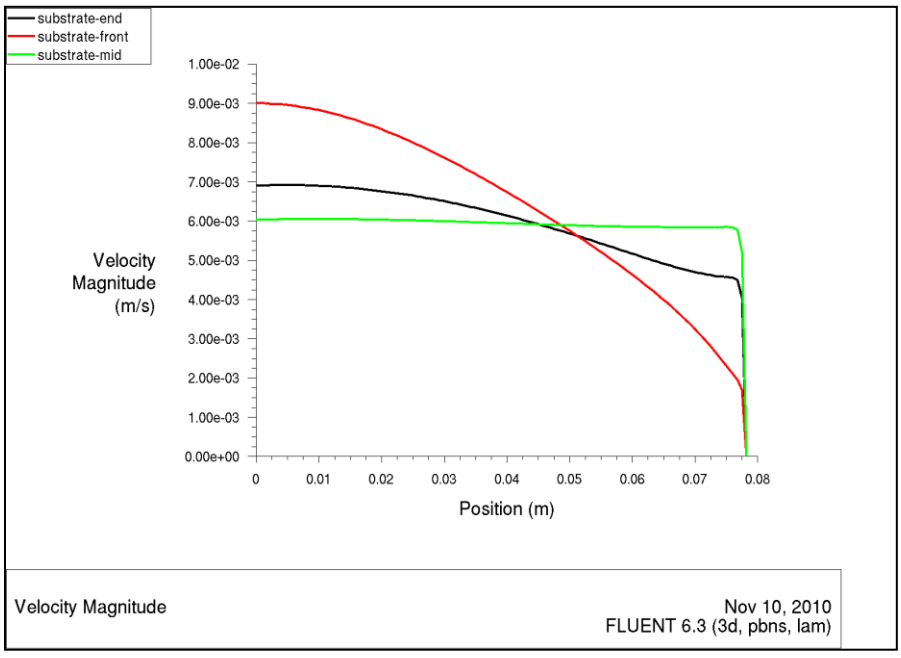

Figure 7-7: (top) Contour of parabolic profile under parallel plate conditions. (bottom) Velocity distribution from edge to middle of the channel (800um separation)

Table 7-1: Variation in velocity magnitudes (Parallel plates)

	Average Velocity	Max. Deviation	Coefficient of Variance
Front	0.006496	0.004542	69.9 %
Middle	0.005939	0.000731	12.3%
End	0.005986	0.001949	32.6 %

I. Spline Line (on 4 channels)

The initial top plate deflection model (using design version 5) estimated the path of four streamlines as straight line segments in three zones, inlet manifold, substrate region, and outlet manifold. Equal spacing of 39mm was maintained between each line in the substrate region and converged to the inlet/outlet in the appropriate manifolds.

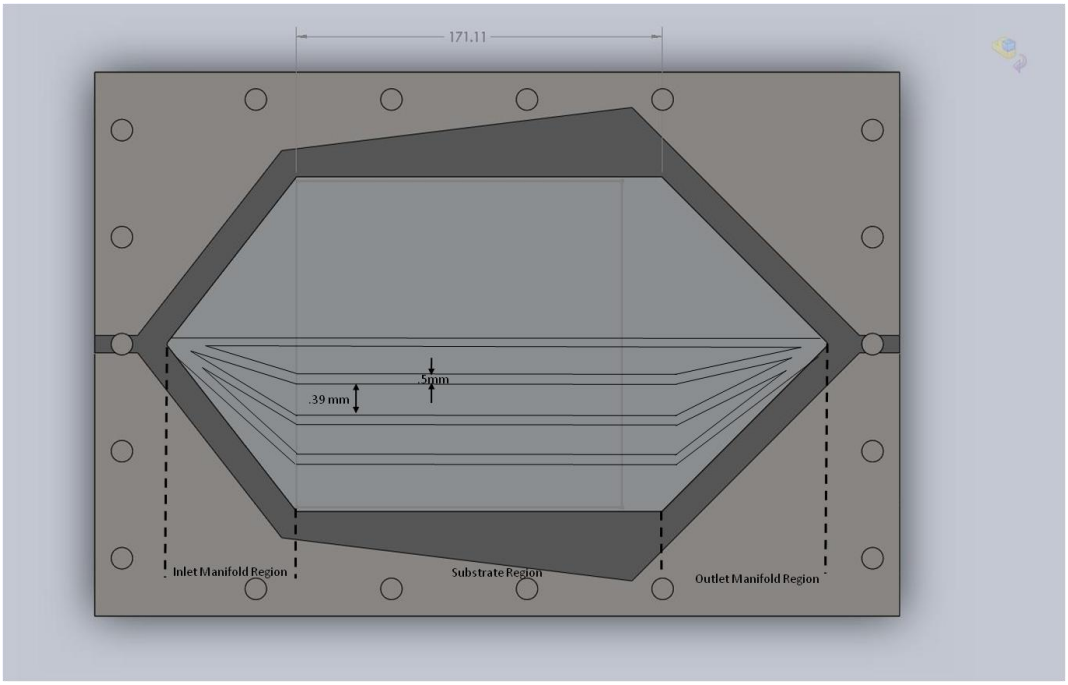

Figure 7-8: Initial model assuming four straight streamline paths

A width of 0.5mm was used to outline four channel paths and the total length of center streamline of each channel was measured. The Hagen-Poiseuille equation was used to evaluate the required height for each channel from the edge to the middle of the plate. The outer most border of the deflected plate was set to a reference height of 800 µm. The spline feature in Solidworks was used to connect these reference points and the loft feature used to form the surface profile between the three sections.

Spline Line results (11-20-09)

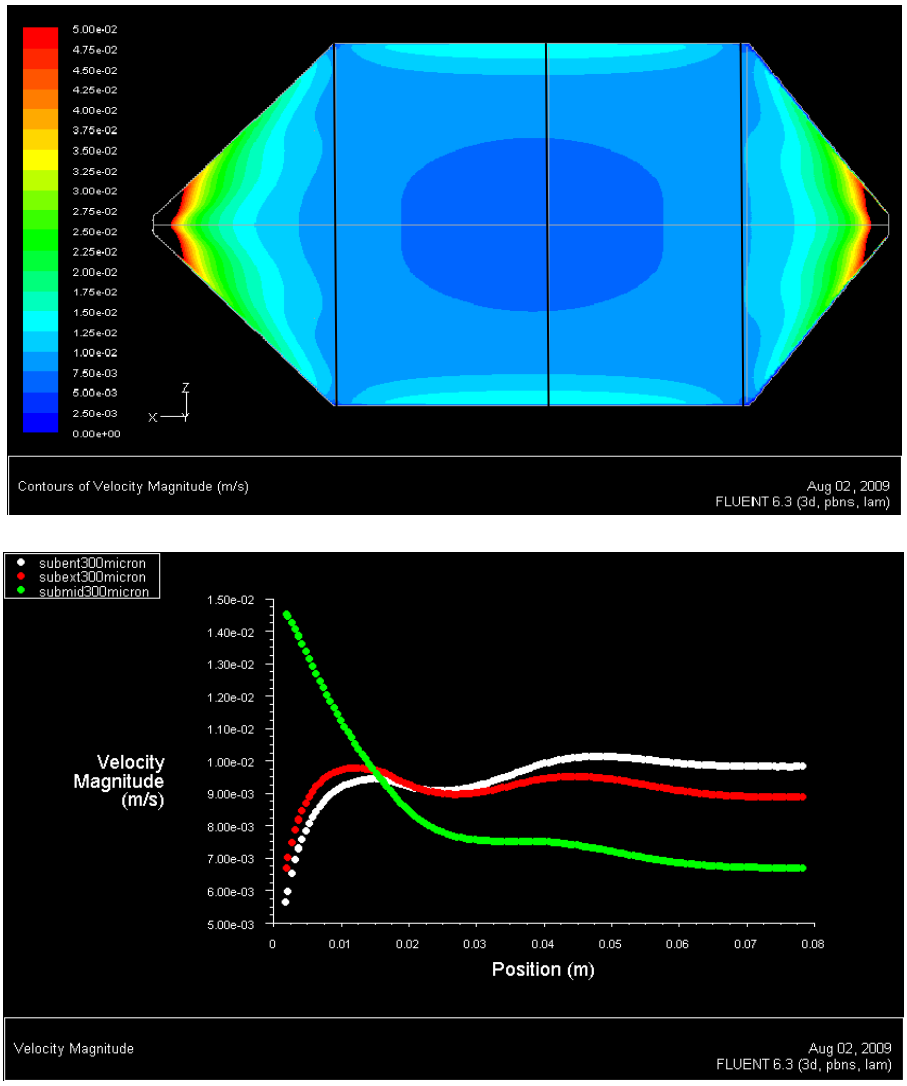

Figure 7-9: (top) Velocity contour map of spline model. (bottom) Velocity profile at substrate beginning, middle, and ending plane.

Simulation results showed a slight inversion of the parabolic profile present in the manifold regions shown in the undeflected model. In the substrate region a large decrease in velocity appeared in the center along with an increase along the walls indicating the deflection is too aggressive in the center. The instantaneous velocity

profile across the substrate front plane yielded in a 6.9% standard deviation. This increased to 16.2% by the middle plane and decreased to 3.9% by the end plane. This indicates that the upper plate has been over-deflected in the central region causing fluid flow to be diverted to the edges in excess. This is consistent with the appearance of the very low velocity region in the in middle of the flow cell and increased velocity region on the edges along the middle plane.

Table 7-2: Variation in velocity magnitudes (Spline line model)

	Average Velocity	Max. Deviation	Coefficient of Variance
Front	0.009665	0.000673	6.9%
Middle	0.007223	0.001174	16.2%
Back	0.009118	0.000362	3.9%

II. Increased channel divisions (n - Straight channels)

The number of channels used to describe the deflection profile was increased to improve accuracy. The entire area of the substrate region was divided into equal channels of width, w. As an alternative to applying a spline line in the Solidworks model, the height of each channel was plotted and a regression method was used to determine

an equation for the deflection profile. A 3rd order equation fit each series of points for each model with an R^2 value of 99.4%.

At w = 0.5mm, the cell was divided into 156 channels and deflected from 800 µm at the edge to 617 µm at the center. The resulting equation of $y=-7*10^{-9}x^3+3*10^{-5}*x^2$ was used along with the loft feature to complete the model geometry.

.617 mm to 800 mm w=.5 mm

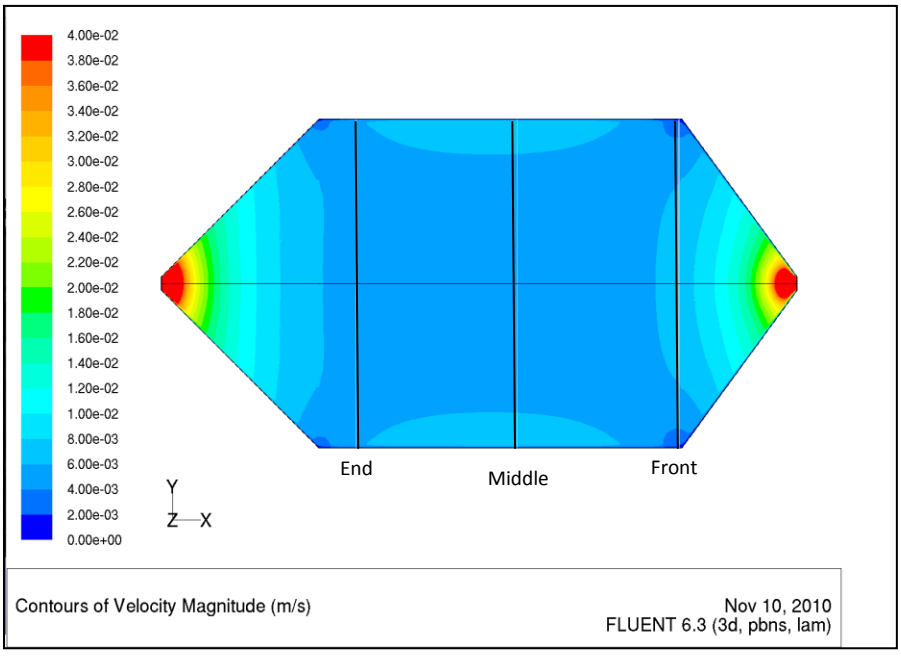

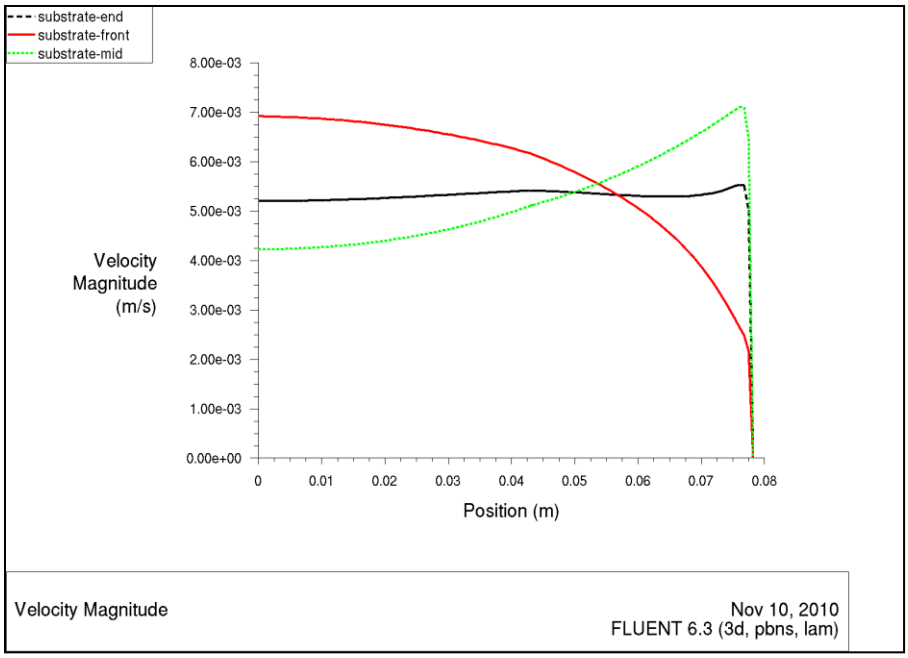

Figure 7-10: (top)Contour velocity map (bottom) Velocity profile at substrate beginning, middle, and ending

The simulation results show a reduction in the parbolic profile seen in the parallel plate results but the deflection is not inverted as in the 4-point spline model. The reduced center and increased edge velocities were also present but not as large as the spline model. The maxium deviation from the velocity average increased from 18.3% at the front plane to 21.7% at the middle plane before falling to 3.2% at the back end plane.

Table 7-3 : Variation in velocity magnitudes (w=.5 mm model)

	Average Velocity	Max. Deviation	% Deviation
Front	0.005522	0.00101	18.3%
Middle	0.00416	0.000903	21.7%
End	0.004537	0.000146	3.2%

At w = 0.25mm the cell was divided into 312 channels and deflected from 800 µm at the edge to 540 µm at the center. The resulting equation used to complete the model geometry was $y=-3*10^{-8}x^3+4.2*10^{-5}*x^2$.

.540 mm to 800 mm w=.25 mm

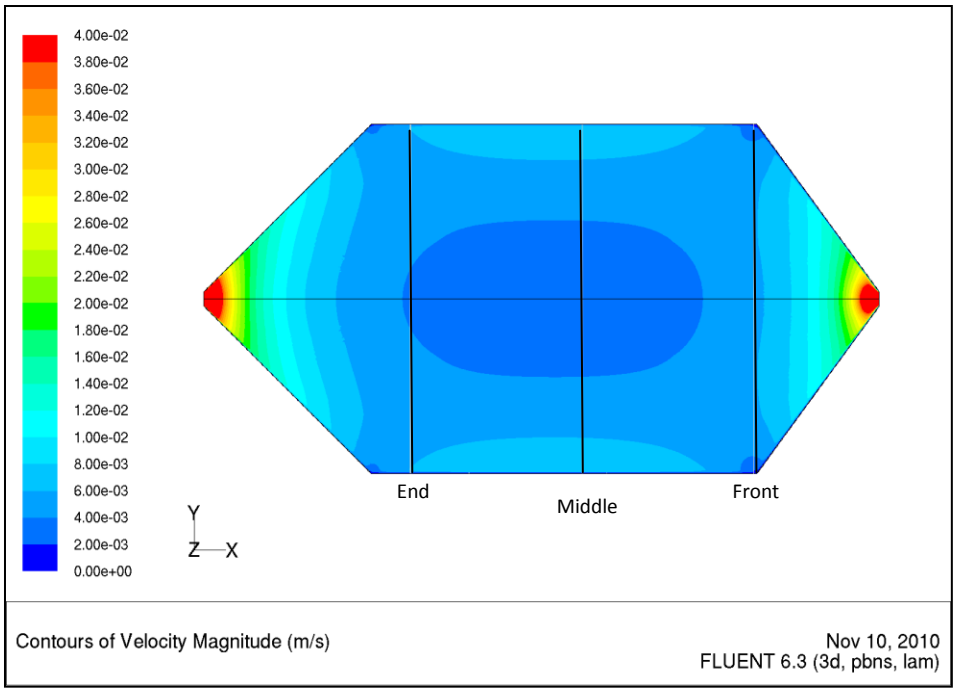

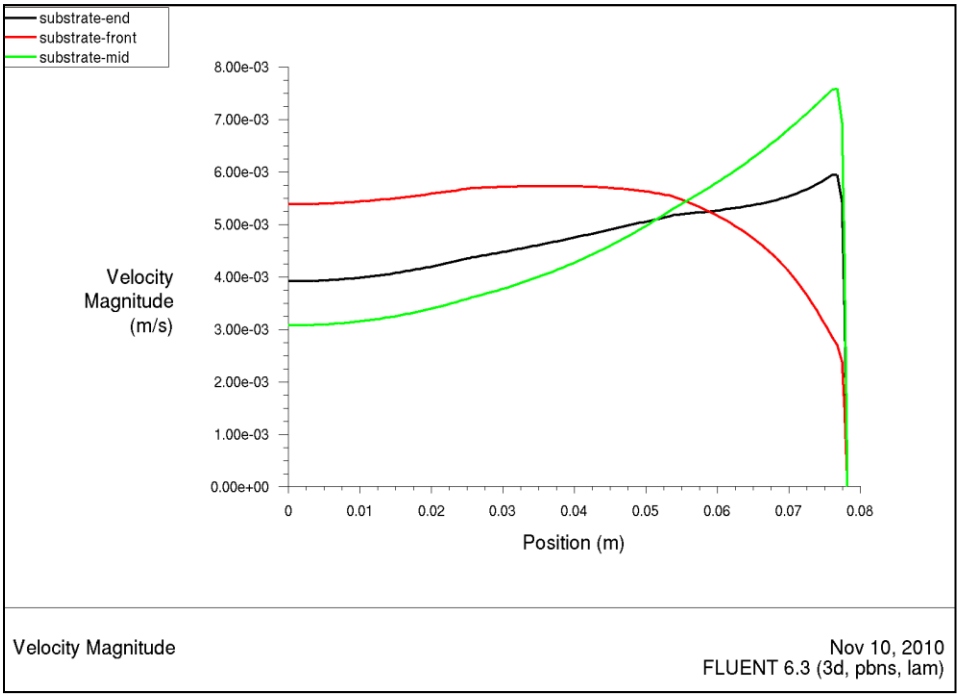

Figure 7-11: (top)Contour velocity map (bottom) Velocity profile at substrate beginning, middle, and ending

The simulation results continue to flatten out the parabolic profile from the w=.5 model while the low velocity zone in the middle of cell and high velocity zones at the edge becomes more pronounced. This model showed the lowest average velocity deviation across the front plane of all models at 4.8% but this increased to having the maximum deviation across the middle plane and ending plane at 42.4% and 20.2%.

Table 7-4: Variation in velocity magnitudes (w=.25 mm model)

	Average Velocity	Max. Deviation	% Deviation
Front	0.004803	0.000232	4.8%
Middle	0.003461	0.001469	42.4%
End	0.00383	0.000773	20.2%

At w=.1mm the cell was divided into 782 channels and deflected from 800 µm at the edge to 392 µm at the center. The resulting equation used to complete the model geometry was $y=9.8*10^{-7}x^3+1*10^{-5}*x^2$.

.392 mm to 800 mm w=.1 mm

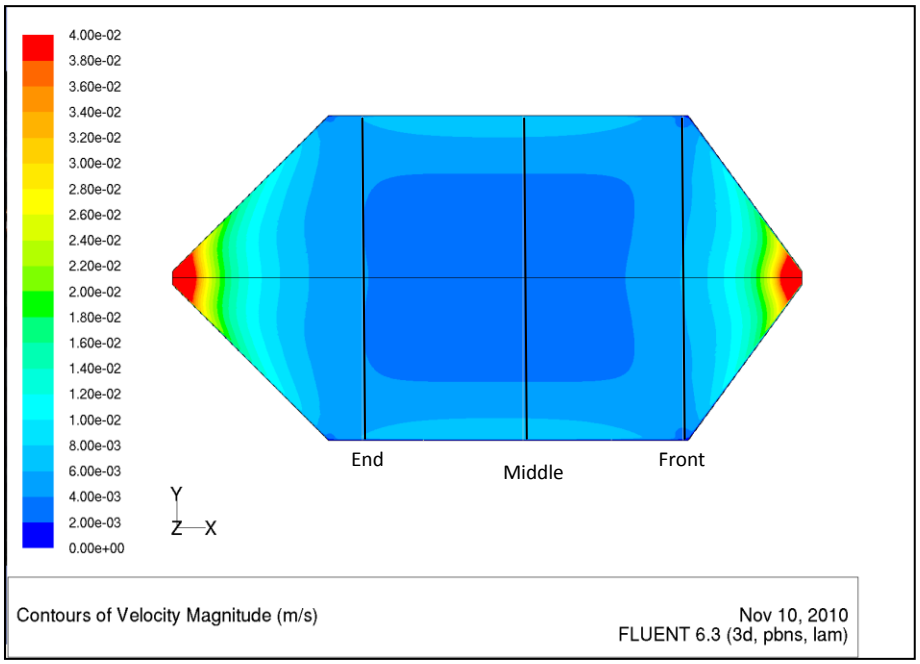

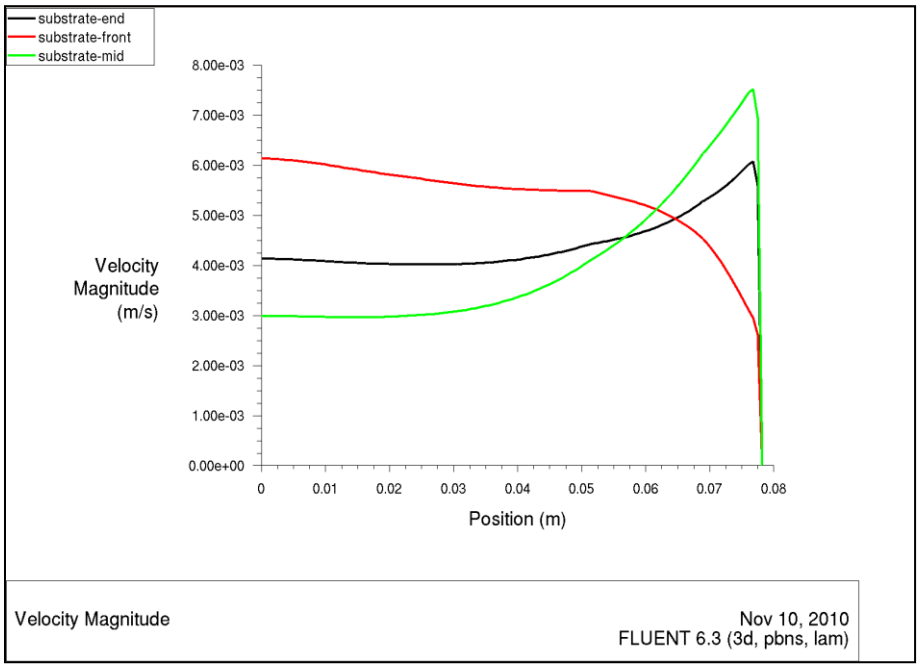

Figure 7-12: (top)Contour velocity map (bottom) Velocity profile at substrate beginning, middle, and ending

The simulation produced similar results to the w=.25 model at the front and ending planes. Neither model inverted in its profile but resembled a more sinesodal shape as it alternated back and forth along the plane. The central region of low velocity began to take on more linar edges verus the oval shape seen in the previous models. Overall deviations from average velocity were only a few percent different from the w=.25 model with 7.7% at the front plane and 40.8% and 14.5% deviations across the middle plane and ending planes.

Table 7-5: Variation in velocity magnitudes (w=.1 mm model)

	Average Velocity	Max. Deviation	% Deviation
Front	0.004893	0.000379	7.7%
Middle	0.002927	0.001195	40.8%
End	0.003494	0.000507	14.5%

APPENDIX C: Final CFD Models

I. Constant velocity model

For constant velocity only the .25 and .1mm width models where evaluated. These two deflected down to 570 and 421um along the centerline. A snapshot visualization of the associated moving fronts are displayed in Figure 3-25.

w=.25mm, Middle channel = 570um

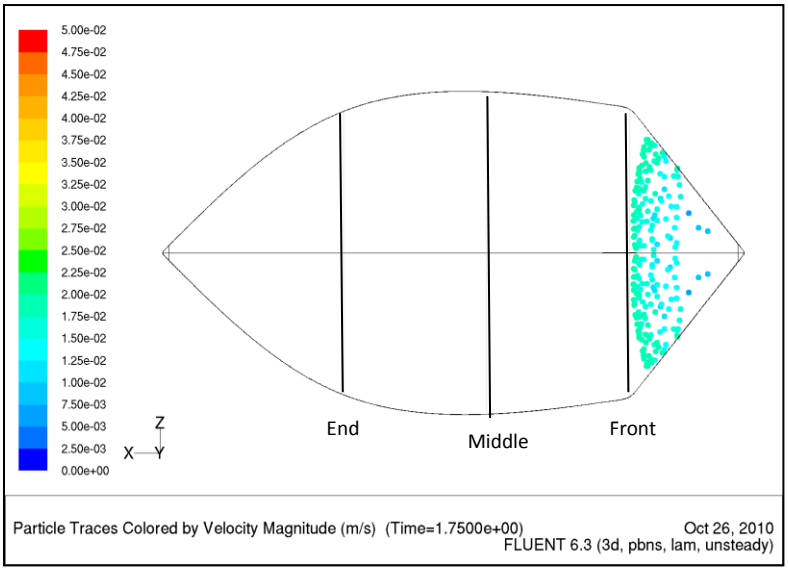

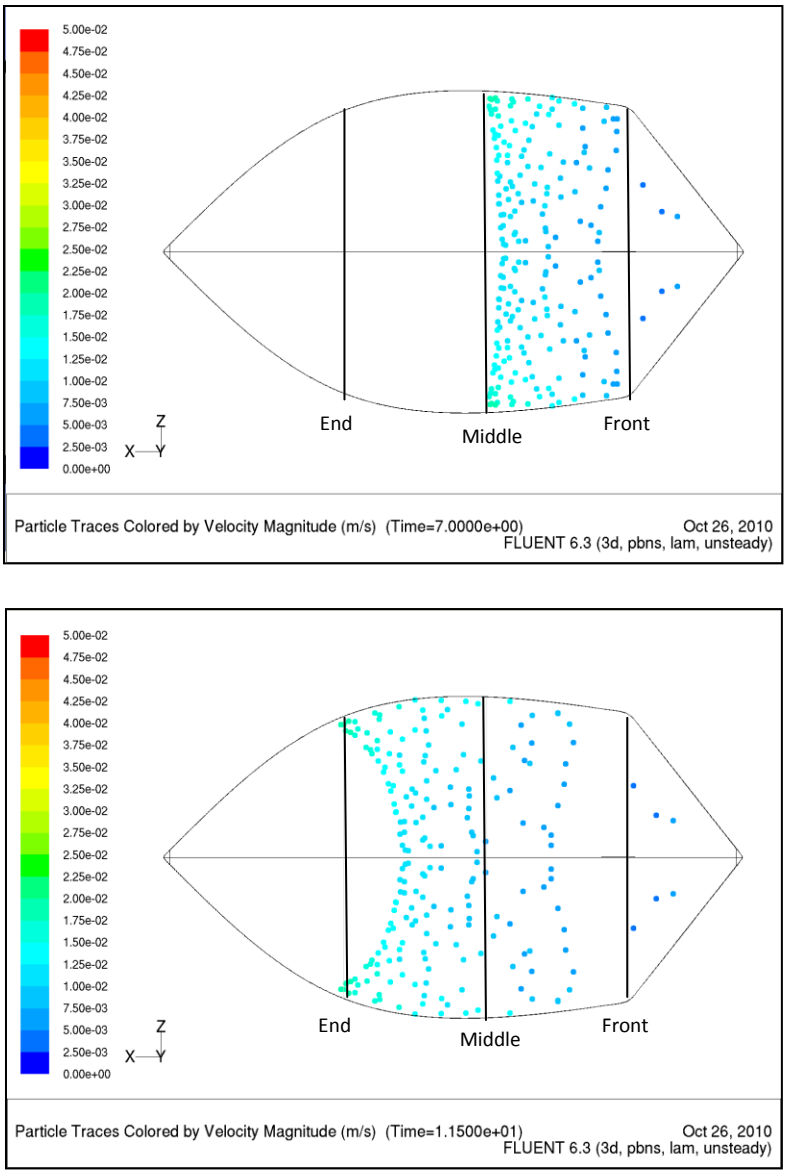

Figure 7-13: Moving front position at substrate front edge(top), middle(center), and end(bottom).

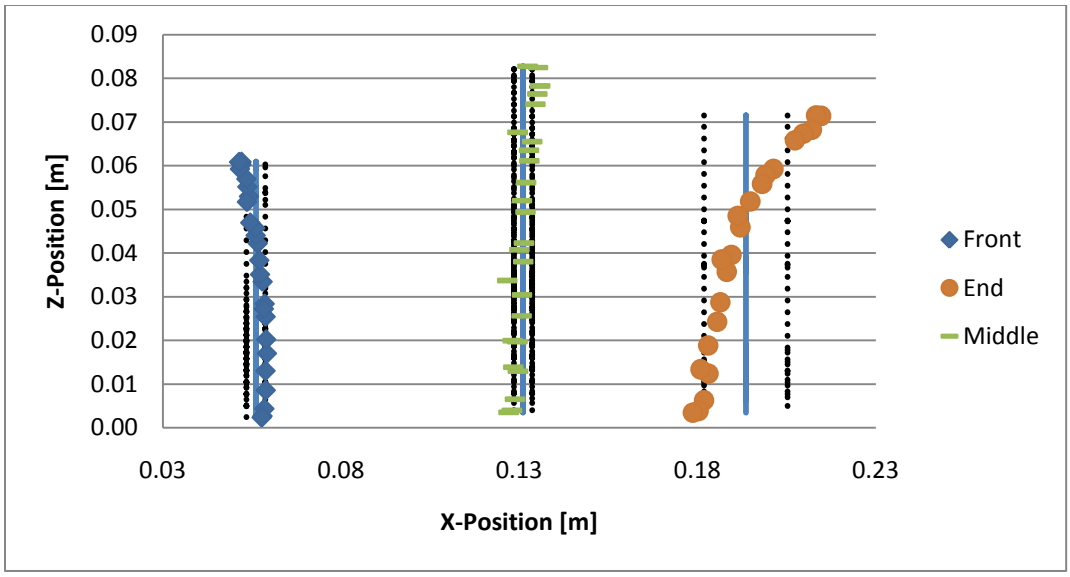

Figure 7-14: Increasing spread of moving front along axial position.

w=.1mm, Middle channel = 421um

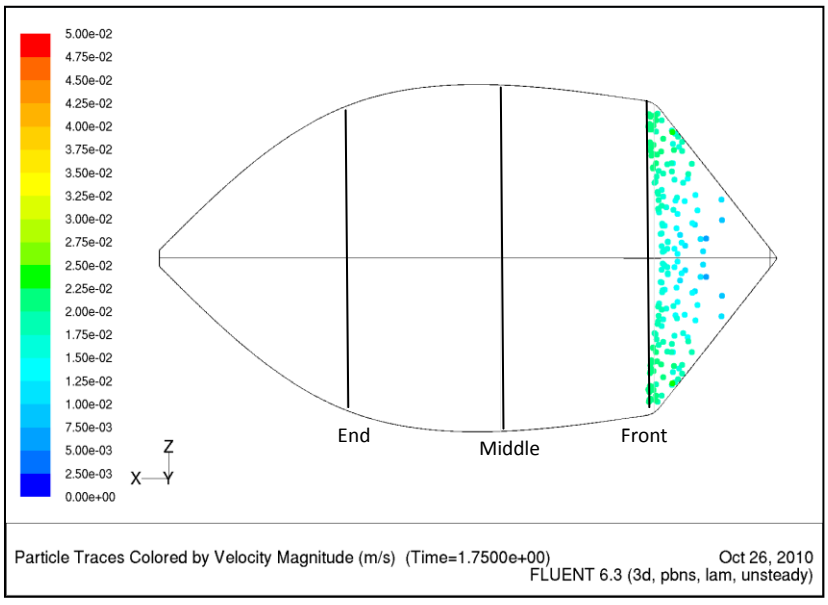

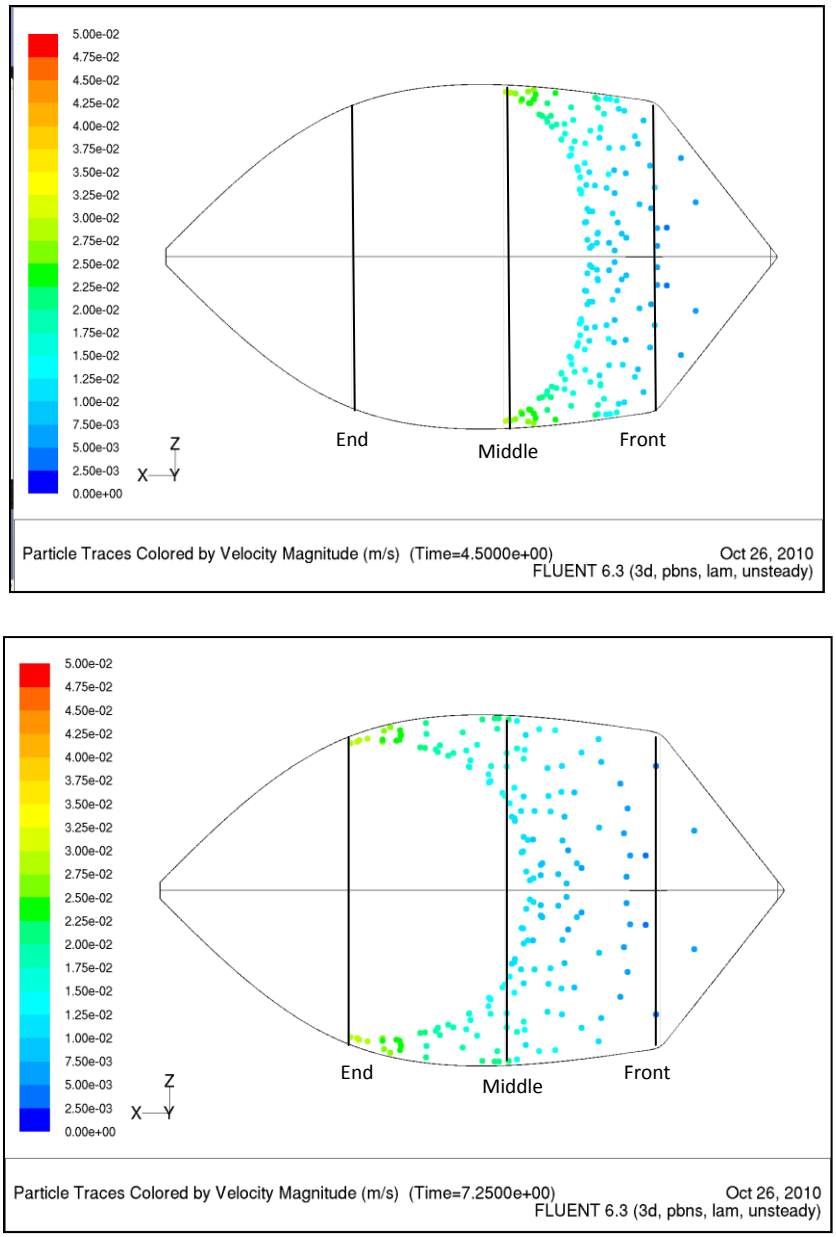

Figure 7-15: Moving front position at substrate front edge(top), middle(center), and end(bottom).

II. Constant residence time model

In a similar fashion the fluid residence time can be mediated by manipulating these same equations. Variation in residence time affects the amount of time reagents have access to the reactive zone. In order to maintain equivalent residence time for each channel the equations in the model above change to:

$$\Delta P = \frac{32\mu L\lambda_{nc}}{D_H^2} V \quad [12]$$

$$V_{1_{ave}} = \frac{L_1}{t_{1_{ave}}} \;\; , \; V_{2_{ave}} = \frac{L_2}{t_{2_{ave}}}, \; V_{3_{ave}} = \frac{L_3}{t_{3_{ave}}}, \ldots \quad [13]$$

$$\frac{32\mu L_1\lambda_{nc}}{D_{H_1}^2} V_{1_{ave}} = \frac{32\mu L_2\lambda_{nc}}{D_{H_2}^2} V_{2_{ave}} = \frac{32\mu L_3\lambda_{nc}}{D_{H_3}^2} V_{3_{ave}} \ldots \quad [14]$$

$$t_{1_{ave}} = t_{2_{ave}} = t_{3_{ave}} = \cdots (\, const\ residence\ time) \quad [15]$$

$$\frac{D_{H_1}^2}{L_1^2} = \frac{D_{H_2}^2}{L_2^2} = \frac{D_{H_3}^2}{L_3^2} = \cdots \quad [16]$$

where V_{ave} and t_{ave} are the average velocity and residence time within the channels.

Targeting constant residence time the model was simulated and evaluated at three different channel widths: .5, .25, and .1 mm. Maximum deflection for each model occurred at the center symmetry line and ranged 521um, 429um, and 280um respectively.

w=.5mm, Middle channel = 521um

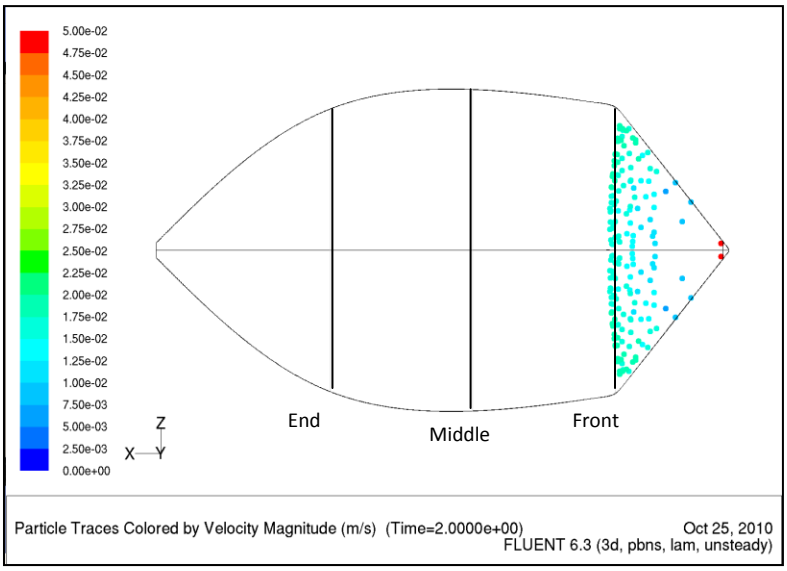

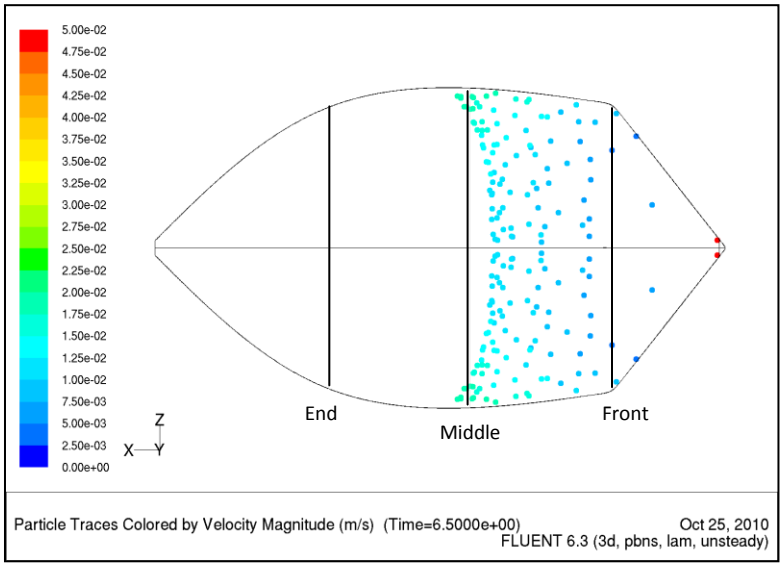

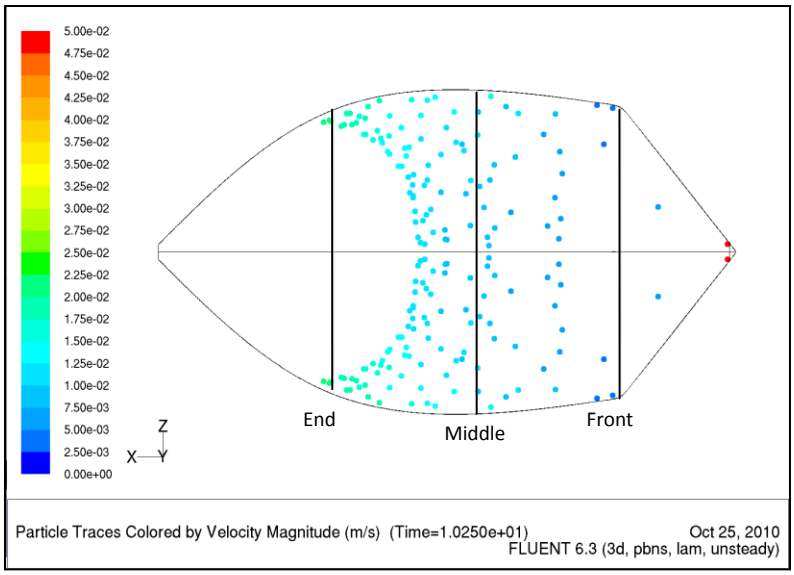

Figure 7-16: Moving front position at substrate front edge(top), middle(center), and end(bottom).

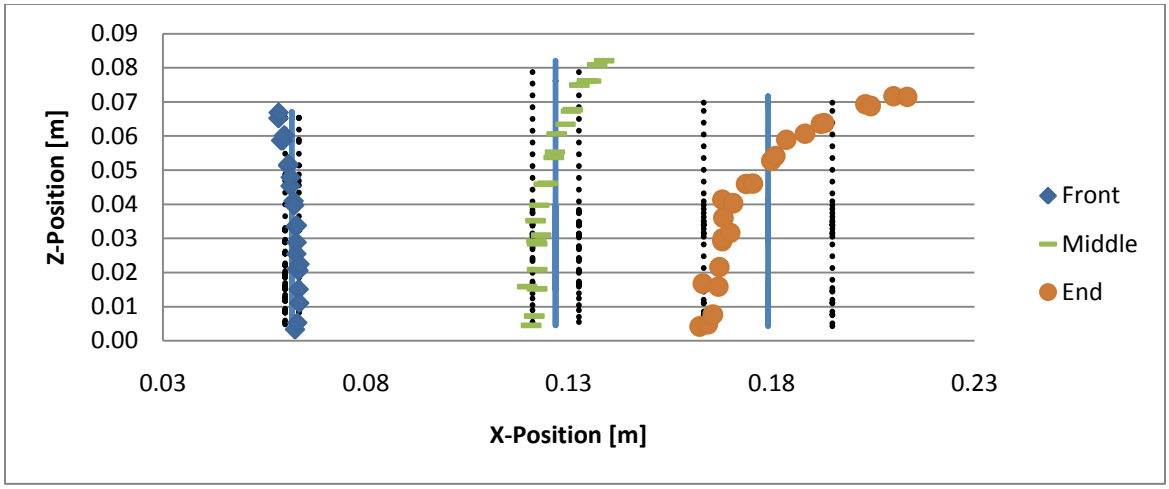

Figure 7-17: Increasing spread of moving front along axial position.

w=.25mm, Middle channel = 429um

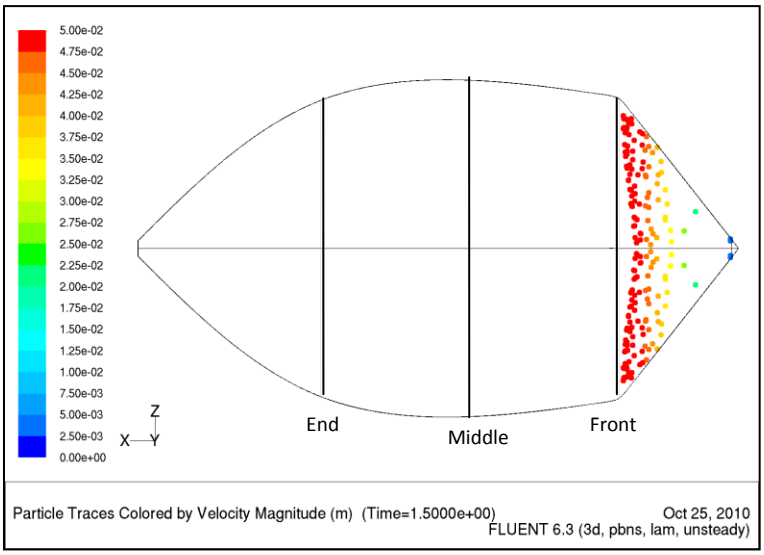

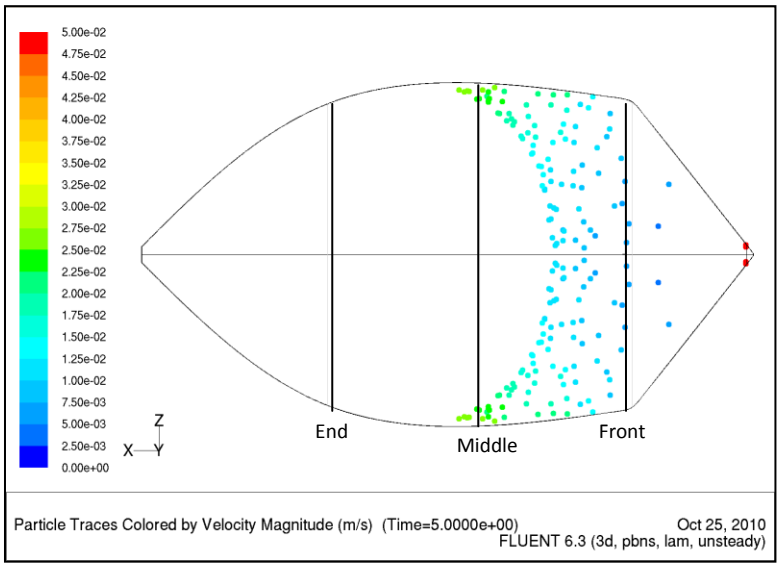

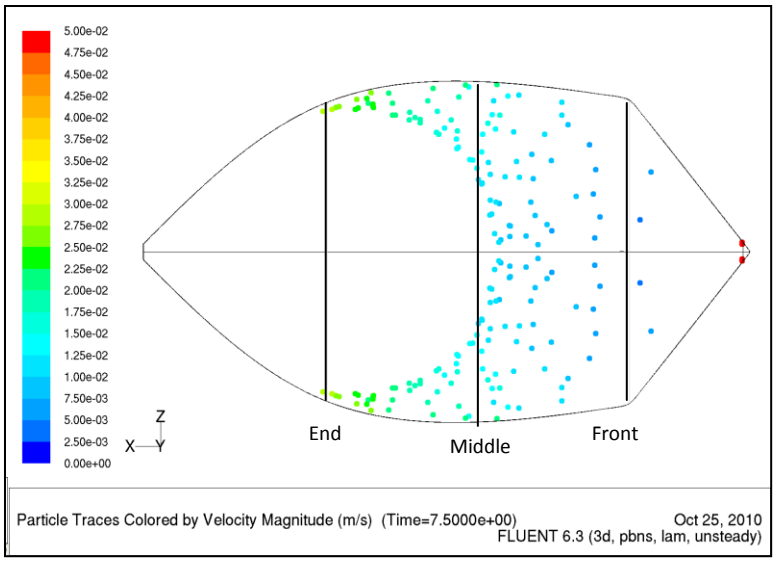

Figure 7-18: Moving front position at substrate front edge(top), middle(center), and end(bottom).

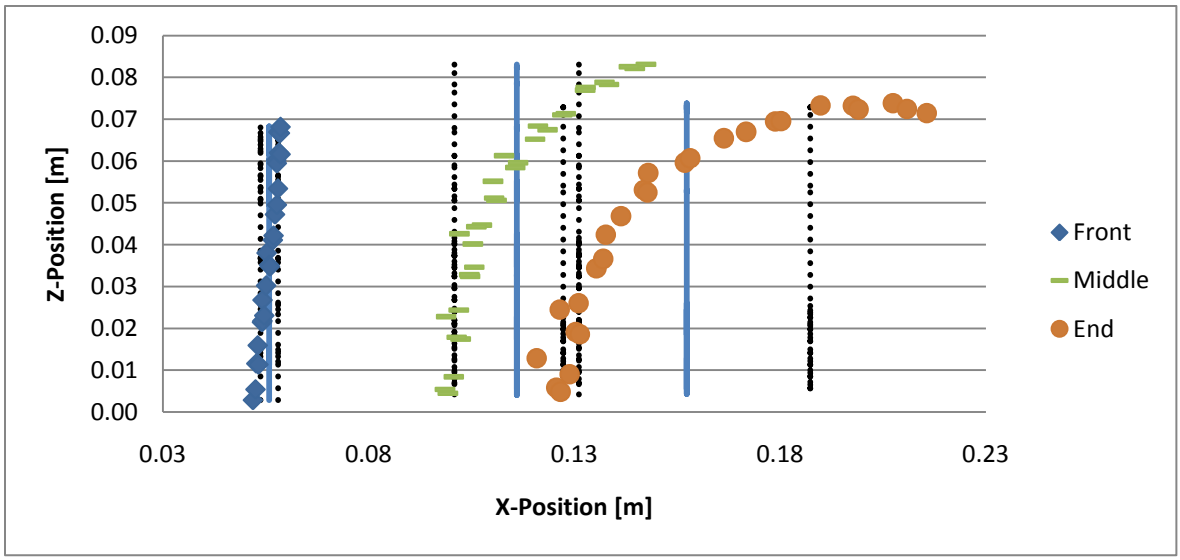

Figure 7-19: Increasing spread of moving front along axial position.

w=.1mm, Middle channel = 280um

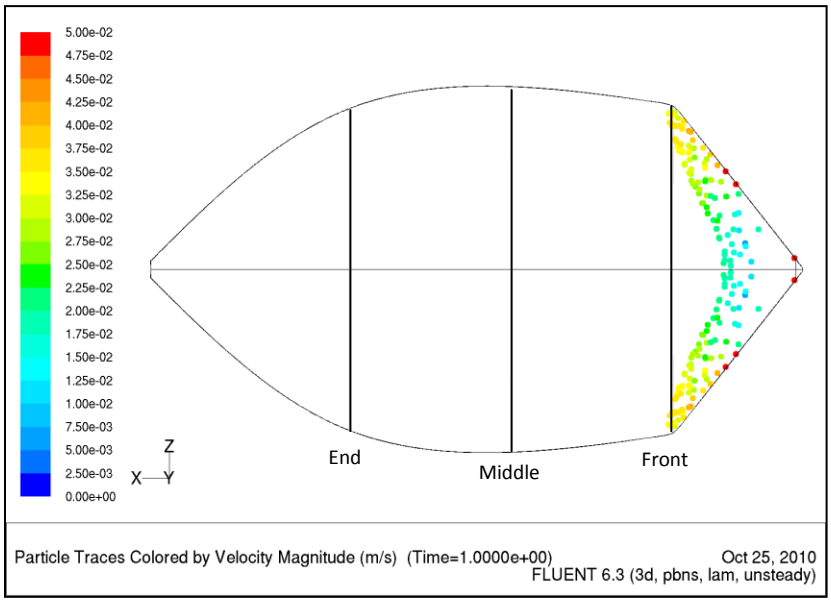

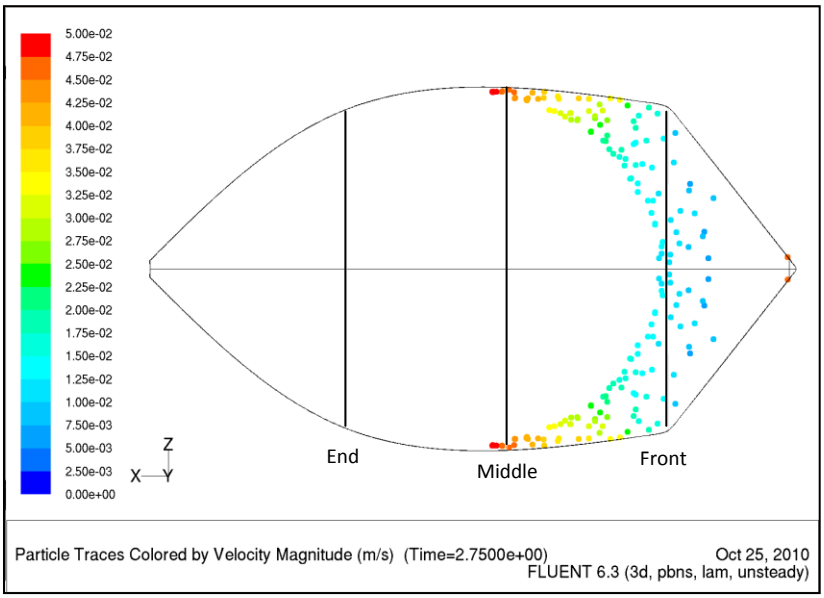

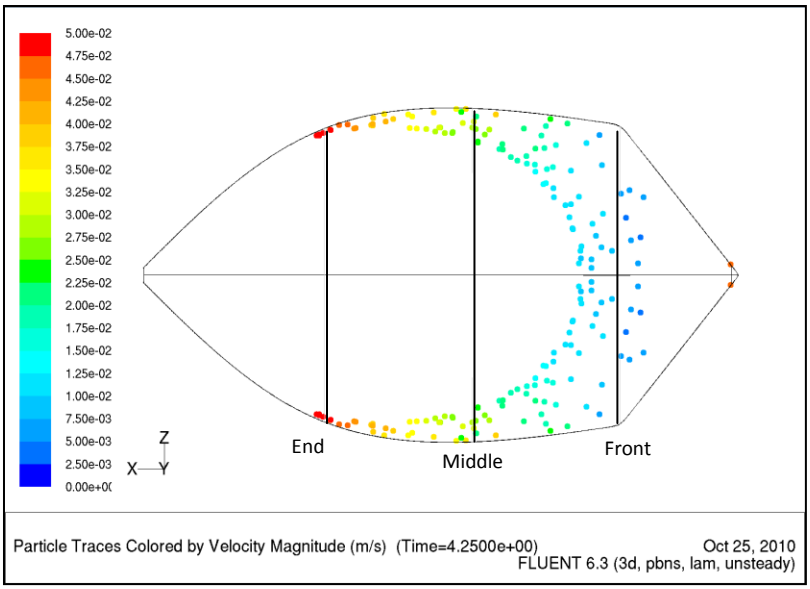

Figure 7-20: Moving front position at substrate front edge(top), middle(center), and end(bottom).

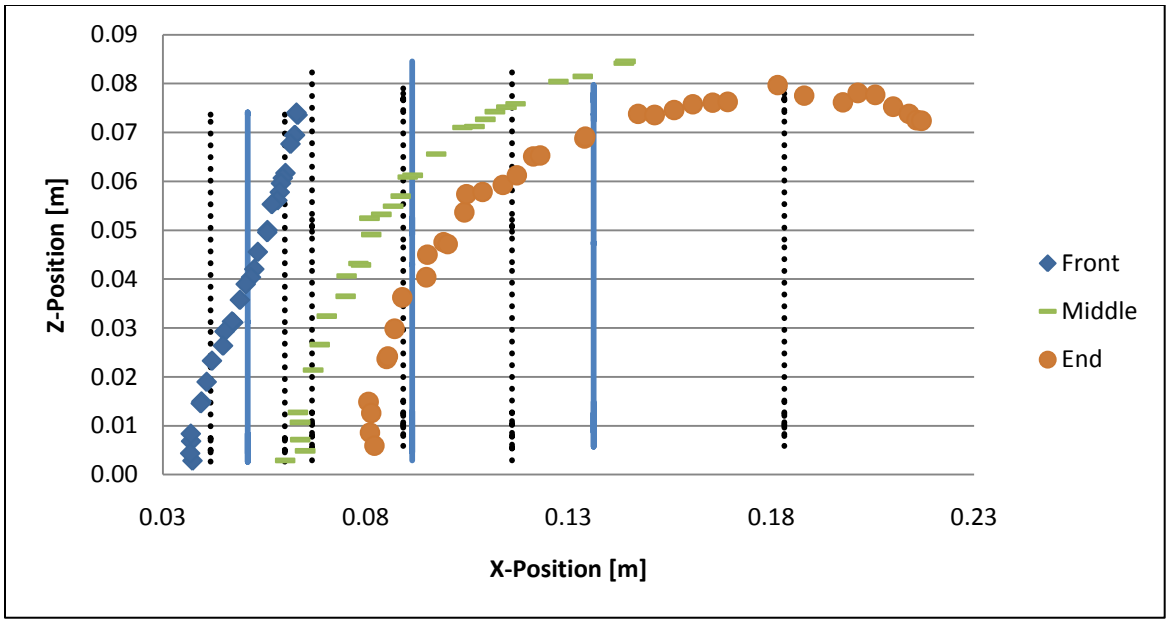

Figure 7-21: Increasing spread of moving front along axial position.

III. FEA Deflection Models

FEA Parameters		
Jacobian point	4	pt
Element Size	8.827	mm
Tolerance	0.441	mm
Total Nodes	93,926	
Total Elements	62,779	

Global contact: No penetration on solid bodies.

Standard fixed geometry on bottom face of silicon gasket

Symmetry assumed along axial plane.

600 N across washer area of 314.16 mm² (Clamp force)

300 um depression along flow axis

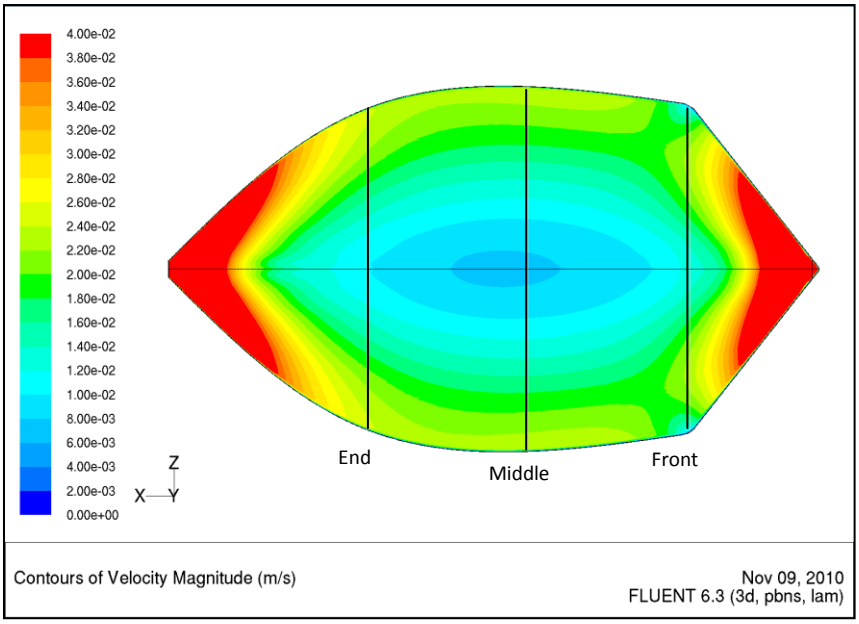

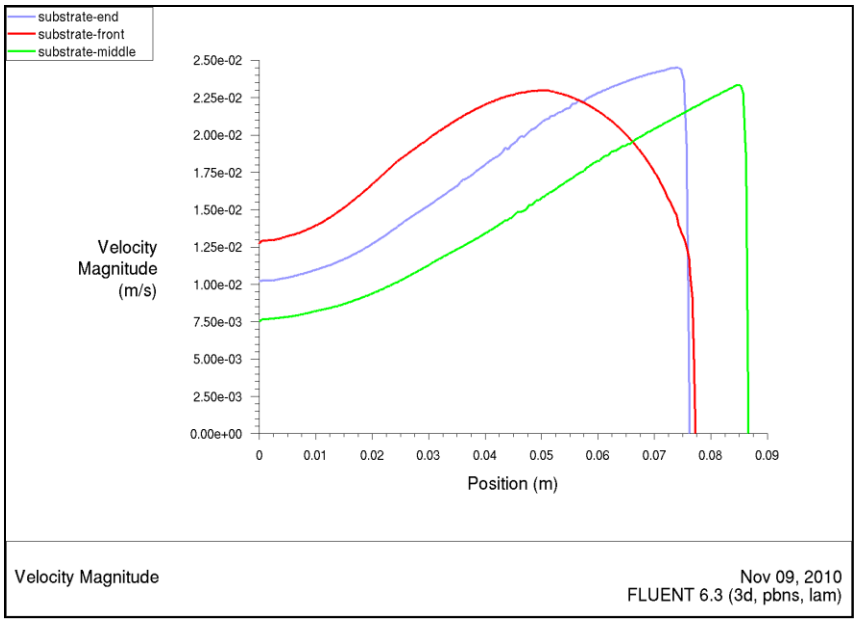

Figure 7-22: (top) Parabolic velocity contour map (bottom) Velocity profile at front, middle, and ending plane of substrate placement.

300 um depression along flow axis

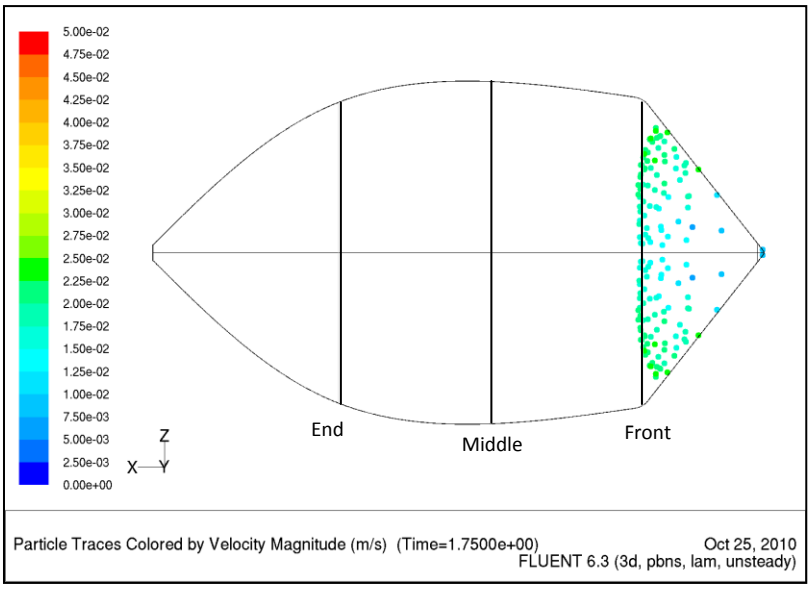

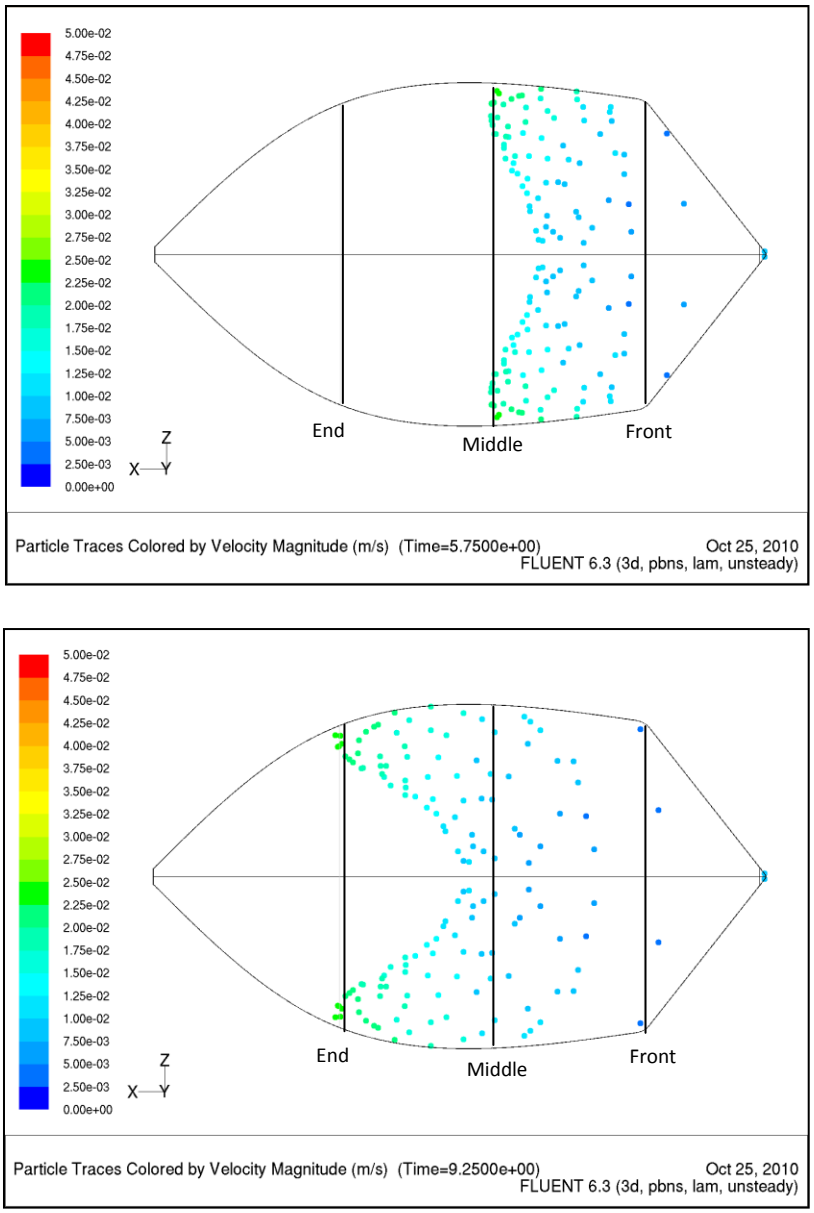

Figure 7-23: Moving front position at substrate front edge(top), middle(center), and end(bottom).

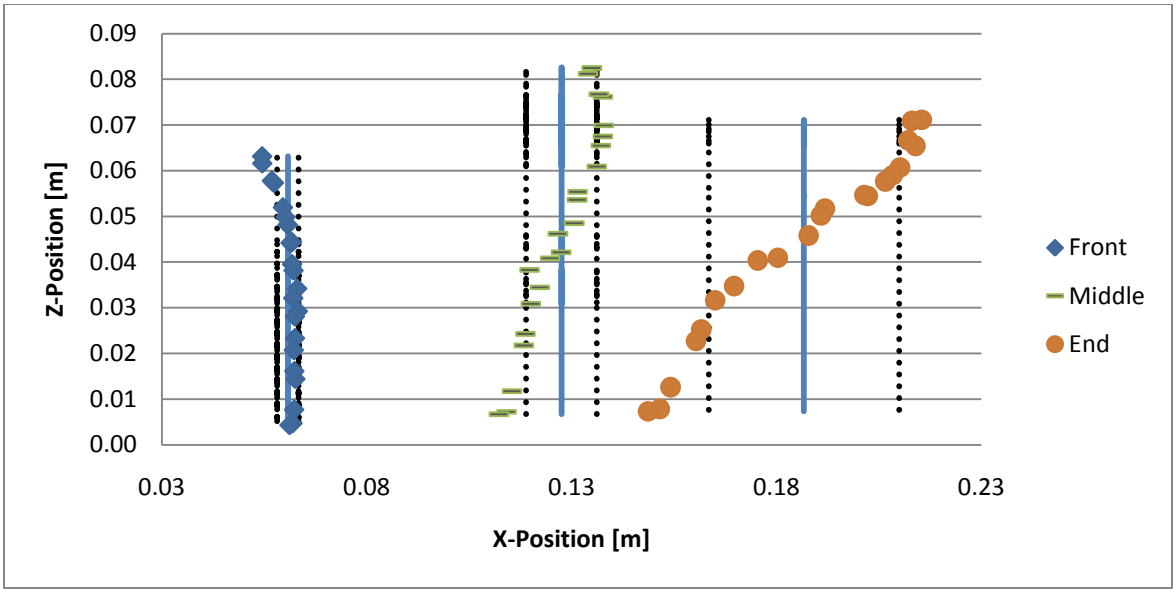

Figure 7-24: Increasing spread of moving front along axial position.

APPENDIX D: Material Properties in SolidWorks

Table 7-6: SolidWorks Material Properties

Material	Elastic Modulus [N/mm²]	Specific Heat [J/Kg K]	Poissons Ratio	Shear Modulus [N/mm²]	Coefficient of Thermal Expan	Density [g/mm³]	Thermal Conductivity [W/m k]	Tensile Strength [N/mm²]	Yield Str [N/mm²]
Silicon Gasket	6.1		0.49	2.9	0.00067	0.001	0.14	13.7871	9.237
Aluminum	6.90E+04	1300	0.33	26000	0.00024	0.0027	170	124.08	55.149
FTO Glass	68935	834.6	0.23	28022	0.000009	0.0024	0.749		
Polycarbonate	2320	1535	0.39	829.1		0.0012	0.0189	62.7	
	[dyne/cm²]					[g/cm³]		[dyne/cm²]	[dyne/cm²]
Stainless Steel	1.93E+12	500	0.27		1.60E-05	8	16.3	500	1.72E+09

APPENDIX E: Progression of forces to achieve 200um deflections

The precision analytical model for version 6 has a constant deflection height of 225 µm along the center axis. Figure 7-25 below shows the progression of forces estimated to construct a constant deflection of 200 µm along the center line. The amount of force applied for each progressive test was done by trial and error. The deflection measure was solely the plane of the upper polycarbonate surface and did not consider the distortion of the bottom surface.

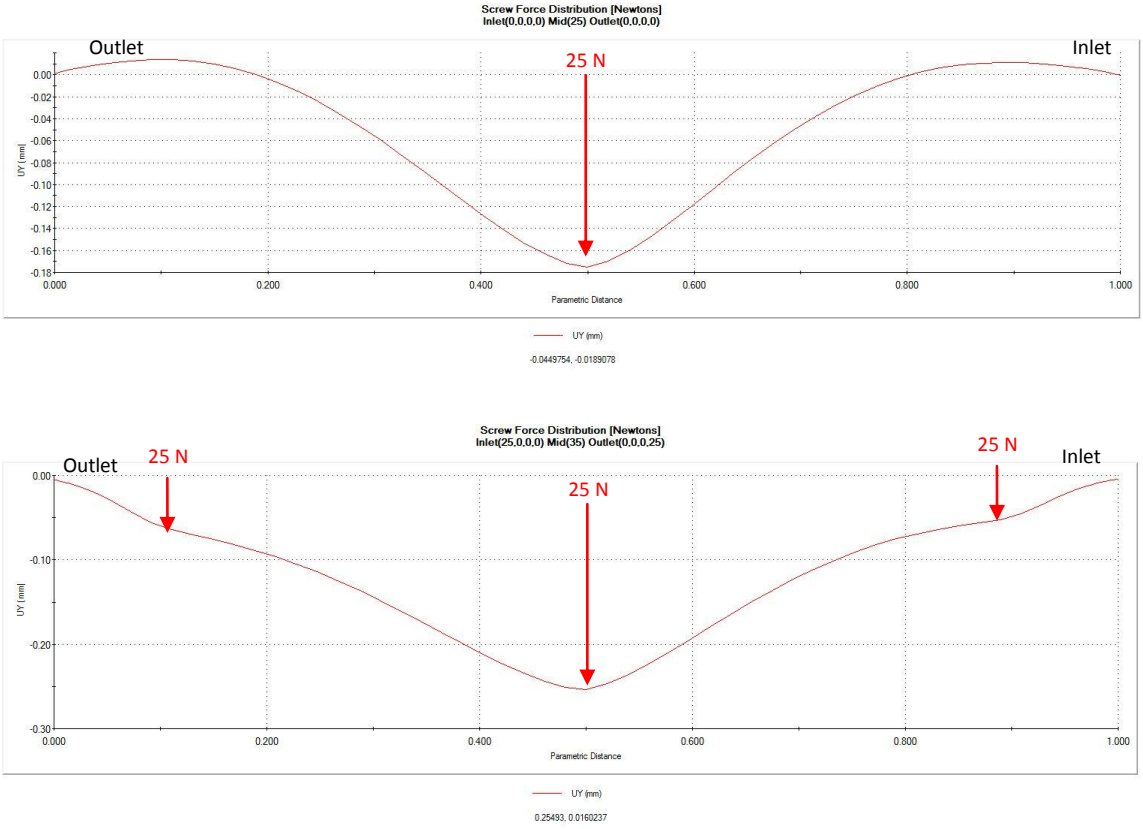

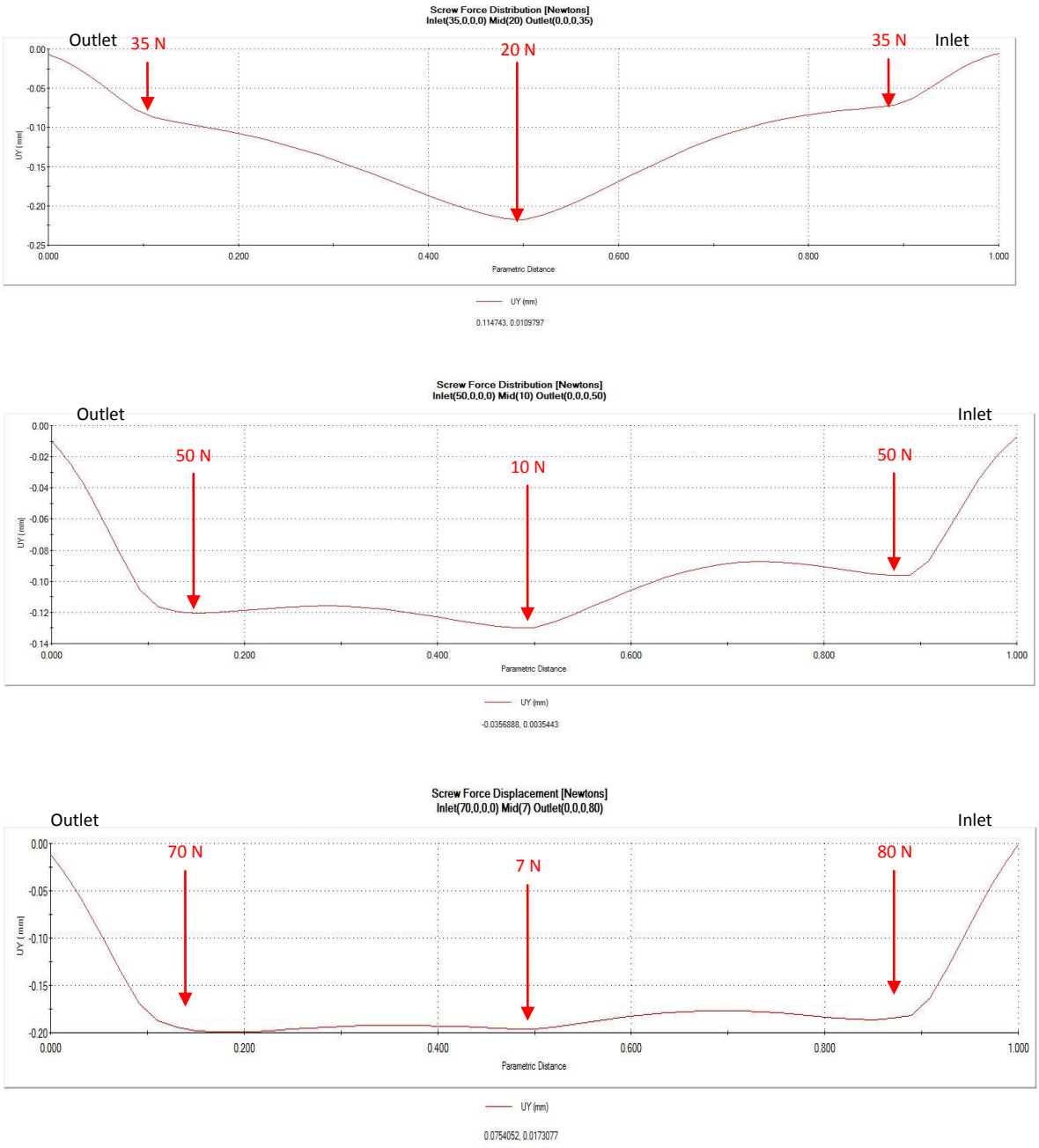

Figure 7-25: Progression of point forces introduced in COSMOS model to achieve 200 µm deflection.

APPENDIX F: LSM Optical measurements for final experiment

The measured deflection in Figure 7-26 is an accumulation of the displacement shown in Appendix E and the distortion predicted in the bottom glass surface.

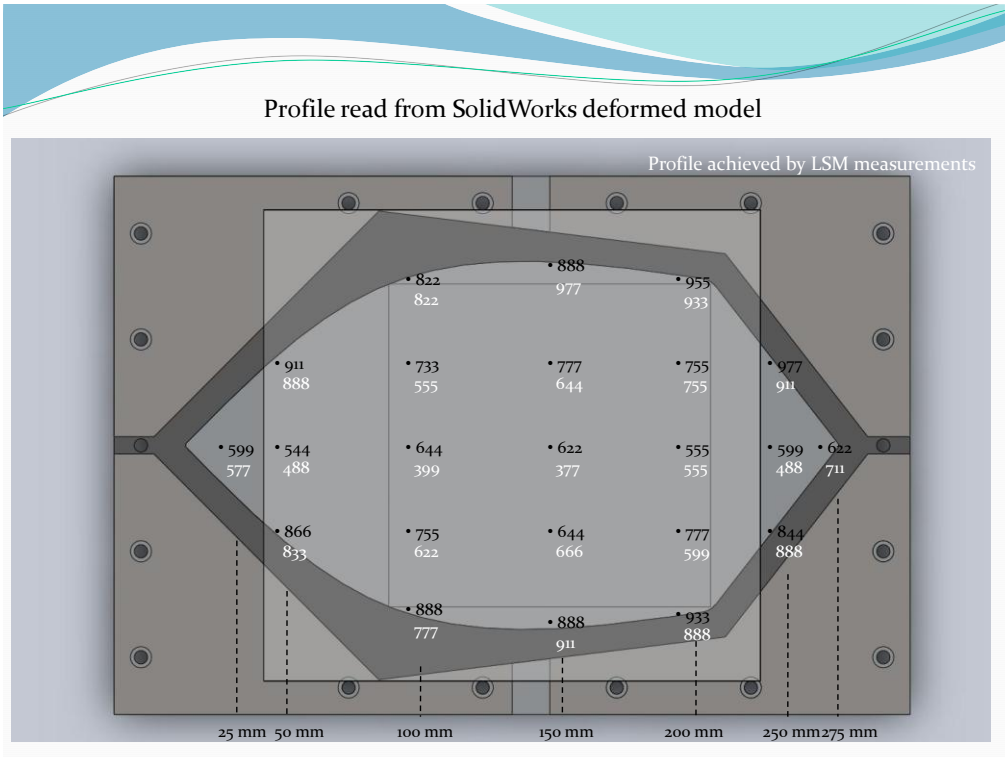

Figure 7-26: Channel gap measurements. (black) Profile predicted from COSMOS model. (white) Profile achieved from LSM measurements.

APPENDIX G: UV-Vis Transmission Data

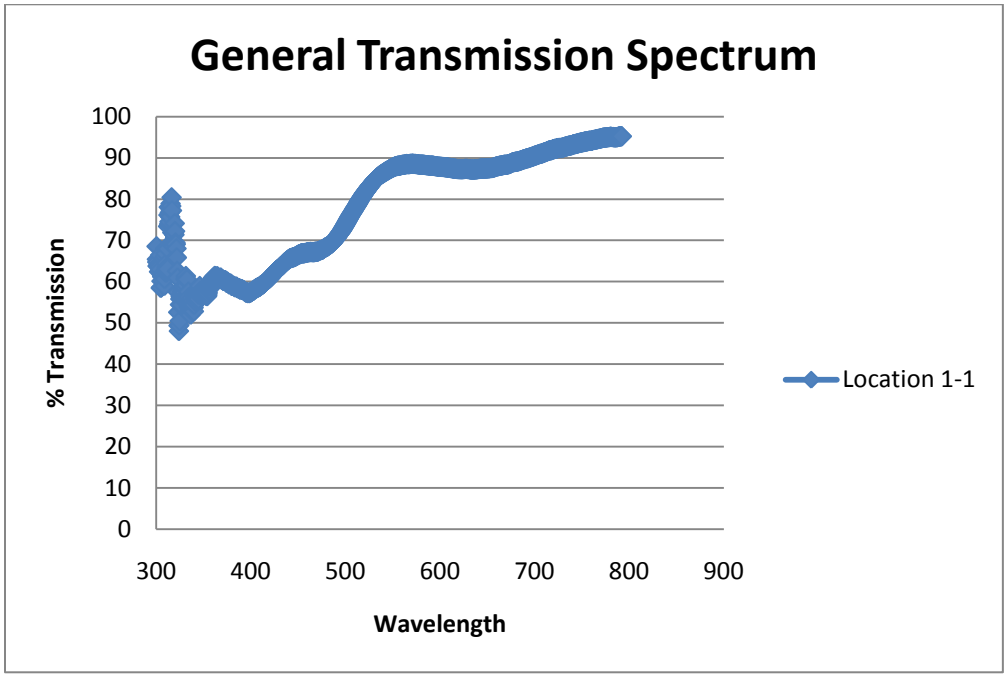

Figure 7-27: Transmission spectrum (Deflected plate at position 1-A)

Table 7-7: Measured UV-Vis transmission at 500 nm (Parallel plate) (red)

Indicates missing data point.

Transmission (T) at 500 nm Wavelength

		Checker Board Block #								
		1	2	3	4	5	6	7	8	9
Inner cell Location	A	77.36%	54.37%	74.23%	70.59%	56.97%	76.87%	71.27%	52.86%	74.93%
	B	70.80%	79.86%	94.10%	64.81%	65.39%	99.82%	98.32%	57.40%	61.58%
	C	66.86%	62.73%	86.49%	70.63%	0.00%	93.50%	94.03%	55.85%	73.39%
	D	76.85%	58.65%	76.42%	69.77%	54.95%	74.95%	89.86%	51.63%	58.84%
	E	66.26%	68.33%	100.16%	60.21%	56.63%	98.23%	97.34%	62.32%	57.66%
	Average	0.716278	0.647874	0.862816	0.671998	0.467874	0.886742	0.901634	0.560098	0.652774
	Std. Dev	0.053012329	0.098772	0.111392	0.045963	0.264679	0.119003	0.11069	0.04209	0.082475

Table 7-8: Transmission data converted to film thickness (Parallel plate) (red)

Indicates missing data point.

Thickness (t) in [nm]

		Checker Board Block #									
		1	2	3	4	5	6	7	8	9	
	A	28.99147813	68.83064	33.65807	39.34533	63.55024	29.71654	38.2592	72.01425	32.60392	
Inner cell	B	39.004991	25.39902	6.866699	48.99892	47.99074	0.208031	1.91723	62.70483	54.76666	
Location	C	45.47602154	52.67664	16.39721	39.27014	?	7.590427	6.950755	65.80305	34.95432	
	D	29.73711374	60.27332	30.37384	40.66521	67.63821	32.56624	12.08198	74.67812	59.90797	
	E	46.48406446	43.02268	-0.1851	57.3137	64.22636	2.013778	3.041835	53.42279	62.20218	
											Total
	Average	37.93873377	50.04046	17.42214	45.11866	60.85139	14.419	12.4502	65.72461	48.88701	38.71386
	Std. Dev	8.341016766	16.74202	14.61022	7.92378	8.758454	15.53872	14.96617	8.369363	14.07644	22.26224

Table 7-9: Measured UV-Vis transmission at 500 nm (Deflected plate) (red)

Indicates missing data point.

500 um Wavelength

		Checker Board Block #								
		1	2	3	4	5	6	7	8	9
	1	73.909	67.957	67.137	65.929	69.493	70.251	66.151	74.469	74.482
Inner cell	2	61.688	68.244	65.968	46.272	60.389	67.131	73.251	72.361	63.615
Location	3	67.323	69.119	69.106	66.814		69.654	69.882	75.514	68.511
	4	65.201	66.877	66.168	68.163	71.85	71.01	69.892	82.41	75.227
	5	69.812	67.262	70.913	69.845	70.21	67.931	70.512	79.933	75.825
Averge		67.5866	67.8918	67.8584	63.4046	67.9855	69.1954	69.9376	76.9374	71.532
Std. Dev		4.622748	0.874755	2.111787	9.690765	5.159526	1.618474	2.532393	4.122665	5.305438

Table 7-10: Transmission data converted to film thickness (Deflected plate)

(red) Indicates missing data point.

Thickness (t) in [nm]

		Checker Board Block #									
		1	2	3	4	5	6	7	8	9	
	A	34.15063586	43.63437	45.00563	47.05657	41.1097	39.88429	46.67685	33.29801	33.27829	
Inner cell	B	54.56689975	43.15833	46.98977	87.04769	56.97088	45.01573	35.16077	36.54159	51.09239	
Location	C	44.69312712	41.71925	41.7405	45.55038	?	40.84831	40.47917	31.72395	42.71726	
	D	48.31078502	45.44393	46.64783	43.29248	37.3421	38.67045	40.46301	21.85286	32.15407	
	E	40.59237222	44.79552	38.82485	40.53899	39.95024	43.67759	39.46541	25.30006	31.2597	
											Total
	Average	44.46276399	43.75028	43.84172	52.69722	43.84323	41.61927	40.44904	29.74329	38.10034	42.01574
	Std. Dev	7.718060175	1.453435	3.490102	19.35924	8.892461	2.649184	4.114611	6.016167	8.595258	9.712299